Title
The Non-linear Time-dependent Mechanical Behaviors of Degradable Polymers and Hydrogels

Permalink
https://escholarship.org/uc/item/3bb51103

Author
Qari, Nada

Publication Date
2023

UNIVERSITY OF CALIFORNIA SAN DIEGO

The Non-linear Time-dependent Mechanical Behaviors of Degradable Polymers and Hydrogels

A dissertation submitted in partial satisfaction of the requirements for the degree Doctor of Philosophy

in

Materials Science and Engineering

by

Nada Faisal Qari

Committee in charge:

Professor Shengqiang Cai, Chair
Professor Jinhye Bae
Professor Renkun Chen
Professor Robert Sah

2023

The dissertation of Nada Faisal Qari is approved, and it is acceptable in quality and form for publication of microfilm and electronically.

University of California San Diego

2023

DEDICATION

I humbly dedicate this dissertation to my parents, Faisal Abdullah Qari and Maha Omar Baryan. Thank you for raising me to believe that there is no such thing as impossible! Thank you for believing in me more than I could ever believe in myself. Thank you for teaching me how to chase my dreams with no fear and having faith in my ability to change the world. Although I still have a lot of work to do, I promise to do my best and to be the difference I want to see in the world today and every day!

All of my past, present and future accomplishments will always and forever be dedicated to you, my beautiful parents.

TABLE OF CONTENT

LIST OF FIGURES

LIST OF TABLES

ACKNOWLEDGMENTS

Firstly, I would like to acknowledge the boundless support and guidance offered by Professor Shengqiang Cai as chair of my committee. The depth of his scientific knowledge is truly unmatched and his ability to explain the most complicated concepts in the simplest ways is a special form of art that I had never been exposed to until I met Dr.Cai. A lifetime of learning from him would still not be enough, but I promise to make the most of the short time we spent together with the aspiration of becoming at best 10% of the scientist that he is.

I would like to express my deepest gratitude to my committee members, Professor Robert Sah, Professor Jinhye Bae and Professor Renkun Chen for offering their valuable time and support whenever I needed it. They have each significantly contributed to my PhD with their vast knowledge and expertise within their research field and for that I am eternally grateful.

For the past 4 years, my lab mates and I have shared our daily lives together and all the hardships that a PhD has to offer. We shared innovative ideas, we laughed, we cried, we celebrated our achievements and learned from our failures. Throughout this arduous journey, I am truly grateful to have been surrounded by their wisdom, sense of humor and unwavering support. I am thankful to have shared 1461 days of my life on this planet with them and will carry our friendship with me wherever I go next in life.

Over the years, I had the privilege of working with several research volunteers who have added great value to my work with their invaluable contributions. Their efforts have helped advance my work in ways that would otherwise be impossible. Although no words of gratitude could ever be enough, “Thank you” will always be the best expression! So, thank you to Eugenia Kritsuk, Dr. Hamed Hosseini-toudeshki, Dr. Zhaoqiang Song, Dr. Jennifer Cai and Dr. Zhijin Wang for sharing their valuable time, experience and knowledge voluntarily and out of the goodness of their hearts for the advancement of science.

The program of Materials Science and Engineering at UC San Diego has been my home away from home and what a privilege it is to be part of this world class research community. I am thankful to the program's director, faculty, advising team and staff for all the support they have offered me over the years. I will always be indebted to the program and its people, for the lessons I learned here will carry me very far in life and allow me to reach new peaks that I never thought were possible. This is a debt I can never repay, but I will always find a way to pay it forward and try to be the best Triton that I can be today and every day!

This August marks my 7th year anniversary with Saudi Aramco, a company that has valued me by the giving me the opportunity of a lifetime. Through the Advance Degree Fellowship Program, I was fully sponsored by the company to purse my Master, Micro MBA, and PhD here at UC San Diego. None of my accomplishments would be possible without the infinite support of the Research & Development Center, Training & Academic Programs Department back in the Kingdom and our advising team here in our US-based Houston office. I am and will forever be eternally grateful for everything and truly look forward to generously giving back to the company in every way that I can for the rest of my career.

When one chapter ends, we must always look back and thank the institutions and the people who guided us along the way. Because of that, I proudly acknowledge the University of Houston where I obtained my Bachelor of Science and learned how to dream big. During my time at UH, I was exposed to hands-on scientific research under the mentorship of Dr. Vassiliy Lubchenko. The research program along with Dr. Lubchenko's mentorship had an unforgettable influence on my life and as a result, I decided that I was going to pursue a PhD one day. After almost 10 years, that day is finally here, and I owe it all to the extraordinary Chemistry Department at UH and its faculty, especially Dr. Lubchenko who is and will forever be my first research advisor.

Finally, and most importantly, I would not be the person that I am today without the unconditional love and support of my parents, siblings, family members, friends, mentors, and teachers. Writing all of your names down would require a separate dissertation as you have all impacted my life in your own special way and I was always better for it. All the beautiful parts of me are just a reflection of how you all touched my heart. Your love will continue to infinitely expand my horizons and with your support, I know that there is nothing that I can’t achieve. All of my past, present and future achievements will always and forever be dedicated to you all.

Chapter 2, in full, is coauthored and has been submitted for publication of the material as it may appear in Mechanics of Time-dependent Materials, 2023. Qari, Nada; Song, Zhaoqiang; Hosseini-toudeshki, Hamed; Li, Chenghai; Cai, Shengqiang. The dissertation author was the primary investigator of this paper.

Chapter 3, in full, is coauthored and has been submitted for publication of the material as it may appear in Macromolecular Chemistry & Physics, 2023. Qari, Nada and Cai, Shengqiang. The dissertation author was the primary investigator of this paper.

VITA

2015	Bachelor of Science, Chemistry, University of Houston, Texas
2016-2018	Junior Lab Scientist, Research & Development Center, Saudi Aramco
2018-2019	Saudi Aramco Advance Degree Fellowship – Master Program
2019	Master of Science, Materials Science and Engineering, University of California San Diego
2019-2023	Saudi Aramco Advance Degree Fellowship – Doctoral Program
2022	Micro Master of Business Administration – Rady School of Management, University of California San Diego
2023	Doctor of Philosophy, Materials Science and Engineering, University of California San Diego

PUBLICATIONS

“Tailorable Non-linear Viscoelasticity of Hydrogels”, Mechanics of Time-Dependent Materials, Submitted Revision, August 15, 2023.

"Stress-assisted Erosion of Poly (Glycerol-co-Sebacate) Acrylate Elastomer", Macromolecular Chemistry & Physics, Submitted, August 26, 2023.

FIELDS OF STUDY

Major Field: Polymer Science

Studies in Polymer Mechanics
Professor Shengqiang Cai

Studies in Polymer Synthesis
Professor Shengqiang Cai and Jinhye Bae

Studies in Biomedical Materials and Applications
Professor Shengqiang Cai and Robert Sah

Studies in Theoretical Models
Professor Shengqiang Cai and Renkun Chen

ABSTRACT OF THE DISSERTATION

The Non-linear Time-dependent Mechanical Behaviors of Degradable Polymers and Hydrogels

By

Nada Qari

Doctor of Philosophy in Materials Science and Engineering

University of California San Diego, 2023

Professor Shengqiang Cai, Chair

Degradable polymers and hydrogels are promising classes of soft materials that have sparked the interest of the research community for many years due to their unique properties.

Firstly, we investigate the viscoelastic properties of hydrogels through stress relaxation experiments to gain a better understanding of the force-dependent dynamics of these materials with the aspiration of expanding their application envelope within the biomedical field and beyond.

We experimentally studied the viscoelastic behavior of 4 different types of hydrogels: covalently crosslinked polyacrylamide (PAAm), covalently crosslinked PAAm network immersed in a viscous alginate solution, ionically crosslinked alginate along with crosslinked PAAm-alginate double network.

Through our investigations, we demonstrate that we can tailor the viscoelasticity of a covalently bonded PAAm network by tuning the viscosity of the solution in the gel. Moreover, based on the stress relaxation test of ionically crosslinked alginate gel and the double network gel, we have revealed the quantitative correlation between the ionic bond dissociation and force-dependent viscoelastic behavior of gels containing ionic crosslinks.

Secondly, we conducted a systematic investigation on stress-assisted erosion of the photocurable and degradable elastomer poly (glycerol sebacate) acrylate (PGSA). Without external stress, we confirmed that the elastomer undergoes surface erosion in an aqueous environment.

Upon the application of mechanical stress, our results revealed that the surface erosion rate was dramatically accelerated. By studying the stress corrosion cracking (SCC) phenomena, we demonstrated that the crack growth speed depends on the applied load and is significantly faster than the surface erosion rate of the elastomer.

We have further shown that with decreasing the crosslink density of the elastomer, the crack growth speed during SCC can be slowed down due to the increased viscoelasticity of the material.

With these reported discoveries, we hope to provide the scientific community with multiple methodologies to develop advanced polymers with tunable mechanical properties while highlighting the importance of time-dependent behavior and how it is correlated to microscopic mechanisms that take place within the polymer network including ionic debonding in hydrogels and the ester bond dissociation in PGSA.

Introduction

Degradable polymers and hydrogels are promising classes of soft materials that have sparked the interest of the research community for many years due to their unique properties.

Hydrogels are composed of a three-dimensional hydrophilic polymer network in which a large amount of water is interposed. This molecular structure makes hydrogels suitable for many applications in the biomedical field, active devices, soft robots, and environmental engineering. While degradable polymers have the ability to break down in response to certain triggers that include temperature, humidity, and light while sustaining their mechanical properties. Because of that, they offer a solution to the ever-growing global problem of plastic pollution.

Both materials have the potential to accelerate the development of sustainable polymers, drug delivery devices and soft actuators. However, and when used for application development, these materials are exposed to external factors including dynamic loading, stress, strain, and chemically modified environments, all of which can impact the mechanical behavior of these materials along with their performance within certain applications. Yet, a deeper understanding of how such factors can impact their mechanical behavior as a function of time has been limited.

Therefore, and with the results presented in this dissertation, we unravel the importance of the time-dependent mechanical properties of degradable polymers and hydrogels by conducting two in-depth studies. In the first part, we investigate the force-dependent viscoelastic behavior of hydrogels and how it can be tuned to closely mimic the changing behavior of soft tissue in living organisms. After that, we take a deep dive into the degradation mechanism of degradable polymers and the factors that influence them by investigating the stress-assisted erosion of Poly (Glycerol-co-Sebacate) Acrylate elastomer simply known as (PGSA).

From the collective findings of our detailed investigations, we hope to provide the scientific community with a methodology to develop hydrogels with tunable viscoelastic properties while highlighting the importance of force-dependent stress relaxation and how it is correlated with chain debonding mechanisms within the hydrogel network. Additionally, and by coupling the effects of mechanical loading and hydrolytic degradation, we demonstrate the important influence of external factors on the performance of degradable polymers.

Chapter 1

The Mechanical Properties of Soft Matter, A Review

Introduction & Background

Polyoxybenzylmethylenglycolanhydride commonly known as Bakelite was one of the first synthetic polymers composed of phenol and formaldehyde developed by Leo Baekeland in 1907 [1]. The synthetic procedure used was considered the first viable and cheap method to produce plastics, paving the way for the establishment of an industry that would revolutionize the materials world for decades to come. Today, global consumption of plastics is greater than 200 million tons with an expected annual growth of 5% [2].

Yet, commonly used oil-based plastics such polyethylene terephthalate (PET) and high-density polyethylene (HDPE) do not undergo natural degradation which has significantly harmful effects on the environment. In fact, out of the 35.4 million tons of plastic that are generated each year in the United States, 26.8 million tons end up in landfills [3]. While the overall number of recycled plastics remains relatively small with an 8.4% current recycling rate which is equivalent to 3 million tons per year [3].

Due to these facts, and in recent decades, the scientific community gained interest in a special class of polymers known as degradable polymers. They are defined as polymers that can undergo degradation through the action of chemical deterioration [4]. Therefore, degradability depends not only on the origin of the polymer but also on its chemical structure and the environmental degrading conditions [4]. Consequently, a wide range of natural and synthetic polymers capable of undergoing degradation through hydrolysis are currently being investigated and developed for specific applications, especially in the biomedical field [5].

With more investigations and the development of advanced processing methods along with the versatility of polymeric materials, degradable polymers are expected to rapidly replace other material classes, such as metals, alloys, and ceramics for use as biomaterials. In recent years, the sales of degradable polymers exceeded $7 billion, accounting for almost 88% of the total biomaterial market [5]. Future outlooks predict that the biocompatible materials market will reach $11.9 billion suggesting a huge market for degradable polymers in the coming decades.

Nonetheless, finding one polymeric material that can fulfill the requirements of one niche application remains a big issue in the field [6]. Additionally, the mechanical behavior of degradable polymers depends on many parameters that have a significant impact on their properties and practical performance. More importantly and given the fact that their properties change with time, the prediction of their mechanical behaviors within a specific application is extremely challenging.

Although currently used degradable polymers are designed to be fully degraded after a certain period of time, before that, they still need to work robustly, somehow, similar to nondegradable polymers. In contrast, for most nondegradable polymers, though degradation of mechanical behaviors happens, it is slow and causes much less concern.

Therefore, understanding the time-sensitive mechanical behaviors of these polymers makes the investigation truly challenging and exciting.

With these challenges in mind, we believe that the utilization of degradable polymers is not limited to biomedical applications, and by gaining a deep understating of how their time-sensitive mechanical properties change, we aspire to eliminate some of the current limitations while expanding the application envelope of these truly promising class of materials.

The objective of this chapter is to provide a mechanical review on the time-sensitive properties of degradable polymer firstly by exploring a range of mechanical properties including elasticity, toughness, strength, viscosity, and stress corrosion cracking through experimental efforts and computational models that have been developed to study commonly used degradable polymers. More importantly, we focus our attention on polymer erosion and degradation through a range of mathematical models and recent experimental results.

1.2. Elasticity

An elastic modulus also known as Young's modulus (E) is defined as the quantity that measures the resistance of an object to being elastically deformed under stress (figure 1). Mathematically, it is defined as the slope of the stress-strain curve in the elastic deformation region (Equation 1).

$$E = \frac{Stress}{Strain} = \frac{\sigma}{\varepsilon} \quad \textbf{(1)}$$

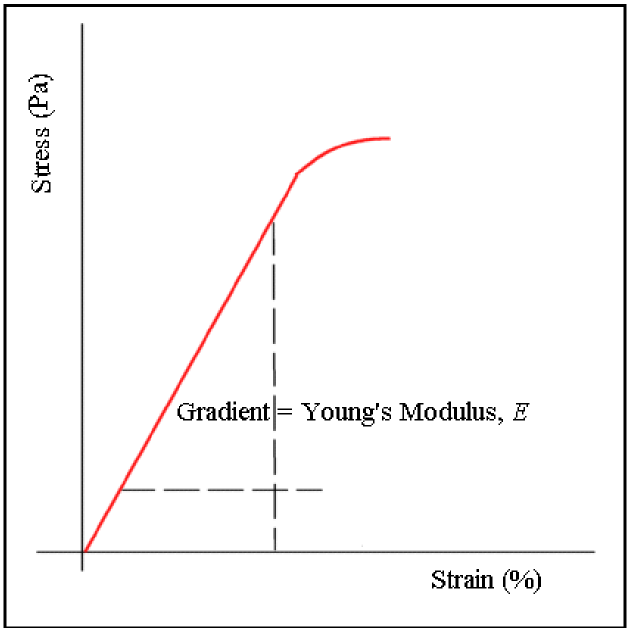

Figure 1: Elastic region as defined by a stress-strain curve [7].

Therefore, the modulus of a degradable polymer and how it changes during degradation is considered a critical design factor when it comes to selecting a material for specific applications. Accordingly, *Wang et al* developed a model that can determine the change in Young's modulus of degradable polymers due to hydrolytic cleavage of the polymer chain. The model is based on the entropy spring theory for amorphous polymers which assumes that when the polymer chains are very short, isolated polymer chain cleavage does not affect the entropy change in a linear degradable polymer during its deformation [8]. Based on that a force applied on a sample of material (f), is related to its stretched length (l), through its internal energy (U), and entropy (S), which is defined by Equation 2 [8]:

$$f = \left(\frac{\partial U}{\partial l}\right)_T - \left(\frac{\partial S}{\partial l}\right)_T \tag{2}$$

where T represents the temperature. For amorphous polymers, the entropy spring model assumes that the internal energy term can be ignored, and it is the entropy change of the polymer chains from a disordered state to a more ordered state during deformation that provides the elasticity of the material [8].

The entropy spring theory reflects the fact that very little force is carried by the polymer backbone during deformation [8]; hence the total internal energy change is small relative to the entropy change which leads to the following prediction of Young's modulus [8]:

$$\mathrm{E = 3Nk_BT} \tag{3}$$

where N represents the number of polymer chains per unit volume, k_B is the Boltzmann constant, and T is the absolute temperature [8].

It's important to note that the entropy theory was developed for fresh polymers with the fundamental assumption that the end-to-end distance of a single polymer chain is much smaller than the extended chain length [8]. This means that the end-to-end distance follows a Gaussian distribution. However, this assumption is no longer valid if random chain cleavage occurs [8].

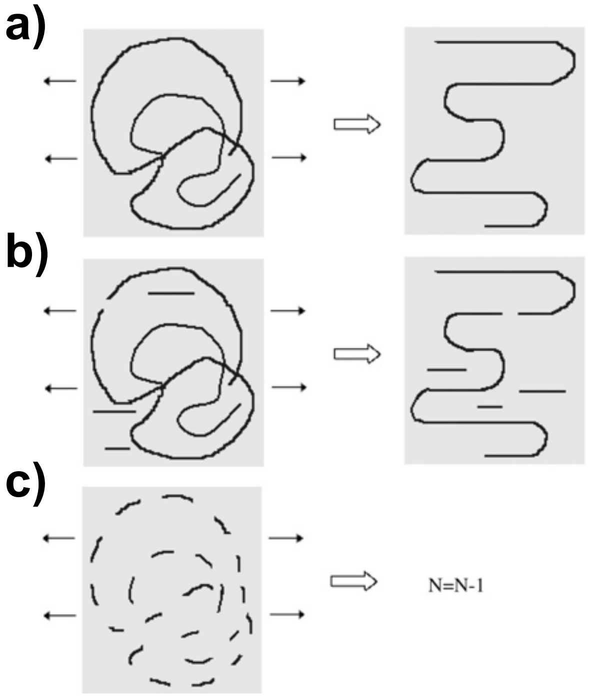

Figure 2: Schematic demonstration of the entropy spring model showing an initially intact polymer chain embedded in many other polymer chains which are represented by the shaded background. **(a)** The entropy of the polymer chains is reduced during deformation as the long molecules become more ordered, giving an elastic resistance to the deformation. **(b)** Neither an isolated cleavage nor very short chains affects the entropy resistance to deformation. **(c)** Sufficient chain cleavages break down the polymer chain which no longer contributes to the entropy resistance to deformation [8].

And since it is complicated to calculate the entropy taking the random scission into account, the theory has been modified to where an isolated chain scission of a very long chain (figure 2.b) should not affect the entropy change during the deformation of the polymer because the long polymer chain is constrained by its surrounding chains (represented by the shaded background in figure 2). It is then reasonable to assume that N does not increase after chain cleavage. This is referred to as the “no rise rule” where very short chains do not contribute to the entropy change during deformation [8].

Therefore, chains shorter than that of a critical degree of polymerization should not be counted when using Equation 3. Consequently, a polymer chain should be removed from the entropy calculation if enough cleavages have occurred so that its molecular weight (or degree of polymerization) is smaller than a threshold that is schematically shown in Figure 2.c [8].

With all these assumptions in mind, a computer code was developed to obtain a numerical relationship between Young's modulus and the average molecular weights. In combination with a degradation model to predict the spatial and temporal distribution of Young's modulus in a cylindrical rod, the following profile was developed.

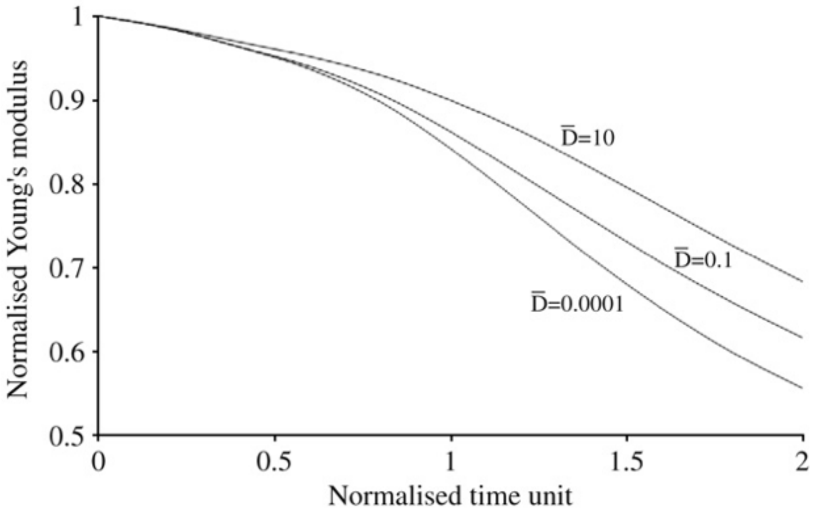

Figure 3: Effective Young's modulus for a degradable rod in its axial direction as a function of the normalized degradation time [8].

Experimental data for PLLA and PDLA were used to determine the reliability of the developed model. And as seen from figure 3, the numerically obtained data show that the reduction of Young's modulus as a function of time was dependent on the diameter of the rod (D) [8]. Similarly, *Ding et al* wanted to understand how elasticity is reduced during the degradation of a polymer system composed of crystal lamellae and an amorphous inter-lamellae phase.

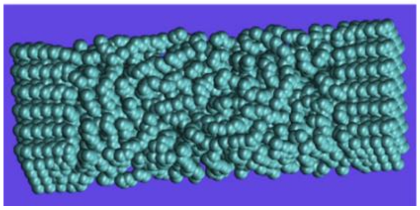

Figure 4: Model for two polymer crystals (lamellae) connected by an amorphous region between them [9].

Molecular dynamics and Monte Carlo techniques were used to develop a model system composed of an amorphous region sandwiched between two polymer crystals (figure 4) which was designed to have mechanical properties that resembles those of poly (glycolic acid) (PGA), a commonly used degradable polymer **[9]**.

To mimic the process of hydrolysis chain scissions in the amorphous region, the polymer chains were cut randomly by removing some of the chain beads which results in creating various chain scissions **[9]**. After an equilibration run, they were subjected to a unidirectional deformation via molecular dynamics simulations that can be regarded as a series of virtual tensile tests completed at different stages of degradation **[9]**.

Results show that below the glass transition temperature, the elasticity of the inter-lamellae amorphous phase was controlled by van der Waals interactions between the polymer chains. Therefore, chain cleavage led to immediate reduction in the Young's modulus **[23]**. Above the glass transition temperature, the simulations confirmed that the elasticity of the amorphous inter-lamellae phase was controlled by the entropy change during deformation and that isolated chain cleavage does not lead to immediate reduction in Young's modulus **[9]**.

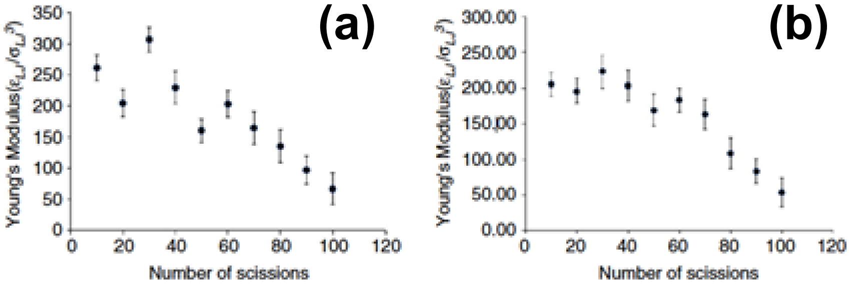

Figure 5: Young's modulus as a function of the number of chain scissions at temperatures **(a)** below and **(b)** above the glass transition temperature where the inter-lamellae region thickness was 8 nm **[9]**.

This means that at temperatures below the glass transition temperature of the model polymer (figure 5.a), the Young's modulus of the system reduces quickly with the number of chain scissions, while above the glass transition temperature (figure 5.b), the Young's modulus reduction lags behind the polymer chain scissions [9].

This observation supports the entropy spring model of amorphous polymers proposed by *Wang et al*, which suggests that Young's modulus above the glass transition temperature is dominated by the internal energy of the system, while below the glass transition temperature, it is dominated by the entropy of the amorphous phase [8,9].

1.3. Toughness

In material science, the toughness of a material is defined as the material's ability to absorb energy and plasticly deform without fracture. Mathematically, it is defined as the amount of energy per unit volume that a material can absorb before rupture and can be calculated by obtaining the area under the stress-strain curve through integration (figure 6).

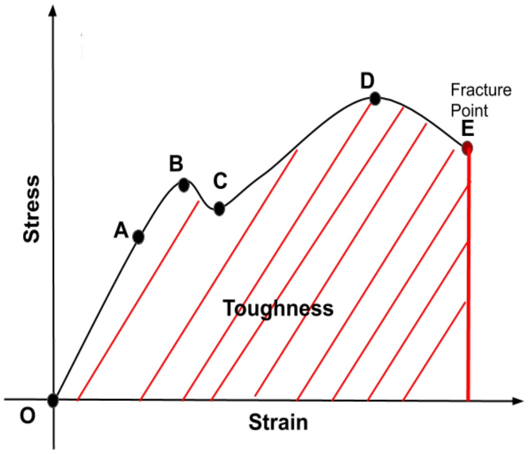

Figure 6: Toughness as defined by the stress-strain curve [10].

The toughness of a polymer and its resistance to fracture determines how it will perform as a device and is therefore considered an important design factor. Multiple studies have been conducted to understand the role of various material parameters and how they can be used to control the toughness. Several experimental methods are highlighted in the current section.

Although toughness is an important parameter, it is often not considered when developing polymer-based biomaterials that undergo extensive mechanical loading and deformation *in vivo* [11]. While matching the modulus of the implant and native tissue is important, the material must be tough in order to survive *in vivo* and not fail prematurely [11].

As an example, poly (β-amino ester) networks are constantly being explored by the scientific community for biomedical applications [11]. Yet, they lack the mechanical properties necessary for long term implantation [11]. And given the fact that methacrylate copolymer networks can exhibit a wide range of mechanical properties, *Safranski et al* wanted to evaluate the effect of adding methyl methacrylate on the poly (β-amino ester) networks' mechanical properties under simulated physiological conditions [11].

The tested networks were synthesized by firstly forming a degradable crosslinker composed of Hexanediol diacrylate (HDDA) and 3-methoxypropylamine (3MOPA) [11]. HDDA was mixed with 3MOPA at varying molar ratios and the step-growth polymerization reaction between the two produced the degradable crosslinkers [11]. The macromers/crosslinkers will be labeled as HDDA and their molar ratio, such that HDDA:3MOPA 1.15:1 will be referenced as HDDA 1.15 from now on [11]. As a final step, varying concentrations of methyl methacrylate (MMA) were added prior to photopolymerizing the network [11].

Strain to failure tensile tests were performed using a thermal chamber in a dry atmosphere at 37°C [11]. In order to determine the effect of degradation on the properties of the prepared samples, dog-bones were soaked in phosphate-buffered saline (PBS) at 37°C for up to 8 weeks, and then strained to failure in a custom environmental chamber that was also filled with PBS and held at 37°C to simulate physiological conditions [11]. Experimental data were used to calculate toughness using the trapezoidal rule from the area under the stress-strain curve and was given in MJm^{-3} [11].

Failure strain and toughness profiles as a function of time for the HDDA-co-MMA networks are shown in figure 7 [11]. As wt% MMA increased, failure strain increased by two orders of magnitude. However, as immersion time increased, the failure strain behavior was composition dependent [11].

The 0% MMA network saw an increase in failure strain (figure 7.a) at 4 weeks from 2% to 14%, but then declined to 4% by 8 weeks [11]. The 35% and 45% MMA networks show an overall average increase in failure strain during the 8 weeks from 14% to 29% and 34% to 47%, respectively [11]. The failure strain of the 55% MMA network remained nearly unchanged during the 8 weeks [11]. The failure strain of the 75% MMA network had an increase from 4 to 6 weeks, but then a decrease by an order of magnitude at 8 weeks from 240% to 5% [11].

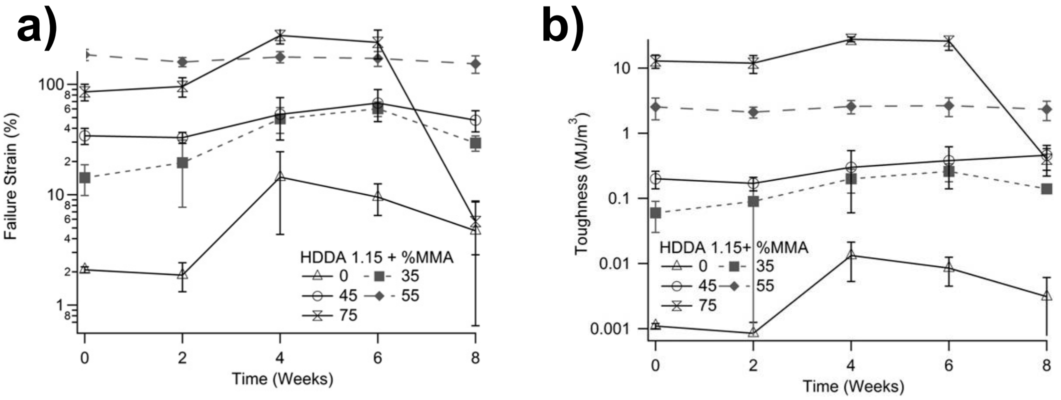

Figure 7: (a) Failure strain profile and **(b)** the Toughness profile over 8 weeks for HDDA-co-MMA networks [11].

As the wt% MMA increased, the toughness increased for all networks (figure 7.b). The effect of immersion time on toughness varied depending on the wt% MMA. For example, the average toughness of the 35% and 45% MMA networks increased over 8 weeks from 0.06 to 0.15 MJm^{-3} and 0.2 to 0.47 MJm^{-3}, respectively [11].

The 0% MMA network showed an increase in toughness at 4 weeks then a decrease by 8 weeks, similar to its failure strain profile. The 75% MMA network had the highest toughness for the first 6 weeks (12 - 27 MJm^{-3}) but decreased at 8 weeks to 0.4 MJm^{-3} leaving the 55% MMA network with sustained average toughness near 2 MJm^{-3} for 8 weeks. The toughness of the 75% MMA network approached values close to that of pure PMMA [11,12].

Safranski et al concluded that varying MMA concentrations resulted in decreasing crosslinking density, which toughened the networks by several orders of magnitude [11]. Under simulated physiological conditions, the mechanical properties change in a composition dependent manner, where select networks increase in toughness or sustain toughness while undergoing degradation [11,12].

In a similar study, *Smith et al* evaluated how immersion time in phosphate-buffered saline (PBS) affects the toughness of photopolymerizable methyl acrylate (MA)–co-methyl methacrylate (MMA)–co-poly (ethylene glycol) di-methacrylate (PEGDMA) networks containing various concentrations of MA [13]. These solutions were prepared by combining ratios of MA and MMA by weight percentage with10 wt.% PEGDMA and 1 wt.% DMPA. Four compositions with varying MA concentrations were used for further testing including 18MA, 29MA, 36MA and 72MA [13].

Stress–strain behavior was determined by performing tensile strain to failure testing after soaking in PBS for different periods that ranged from 1 day and up to 9 months [13]. The toughness of Ultra-High-Molecular-Weight-Polyethylene (UHMWPE) is included on both graphs seen in figure 8 for comparative purposes where it progressively increased with immersion time up to 6 months in PBS, but then abruptly decreased from 80 to 30 MJm^{-3} at 9 months [13].

In figure 8.a, it can be seen that 29MA exhibits significantly greater toughness than 18MA after longer time spans in PBS, but lower toughness compared with UHMWPE, although not significantly so [13]. Specifically, the toughness of 18MA increased with initial exposure to PBS but gradually decreased with time [13].

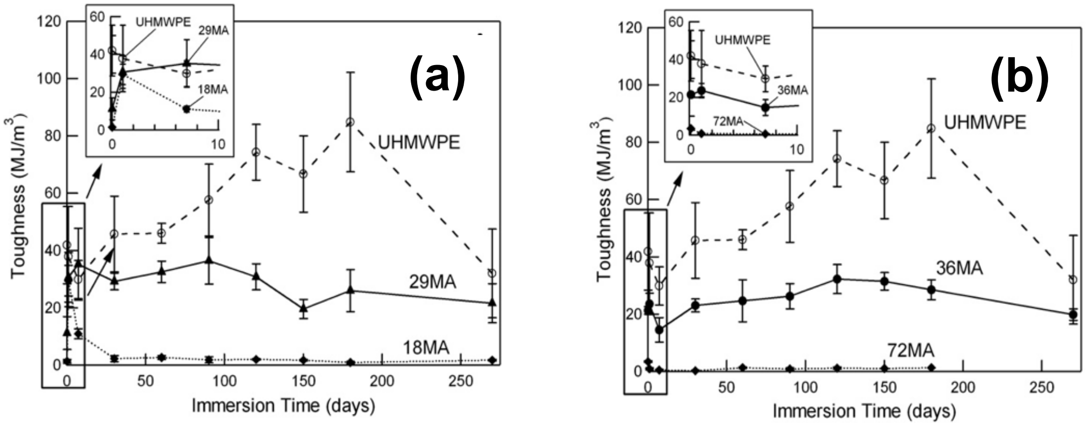

Figure 8: Effect of immersion time on the toughness of **(a)** 18MA and 29MA and **(b)** 36MA and 72MA networks tested in PBS at 37°C [13].

On the other hand, the toughness of 29MA increased within the first 24 hours in PBS and remained relatively stable at around 35 - 40 MJm^{-3} for up to 9 months in solution [13]. As figure 8.b shows, the toughness of 36MA did not change with immersion time in PBS after the first 24 hours, remaining at around 20 - 25 MJm^{-3} [13]. A similar relationship with immersion time was observed for 72MA, although the toughness values were less compared with that for 36MA [13].

Based on these results, *Smith et al* concluded that copolymer networks in a glassy state experience a stiffening effect and loss of extensibility after several months in PBS that is linked to significant decrease in toughness [13]. However, if such networks were modified through the addition of hydrophobic crosslinkers, they might be able to maintain their mechanical properties for up to 9 months in PBS [13].

These findings provide insight into strategies for improving the long-term toughness of not only photopolymerizable (meth) acrylate networks but other polymer-based material platforms that are implemented in load-bearing applications [11,13].

1.4. Strength

Strength is defined as a material's ability to withstand load without failure, the two most common forms of strength are yield and ultimate strength (figure 9). Yield strength is defined as the maximum stress that can be applied without causing any plastic deformation. While ultimate strength is often referred to as tensile strength which can be defined as the maximum stress that a material can withstand before failure occurs. It is a measure of a material's resistance to failure under tensile loading.

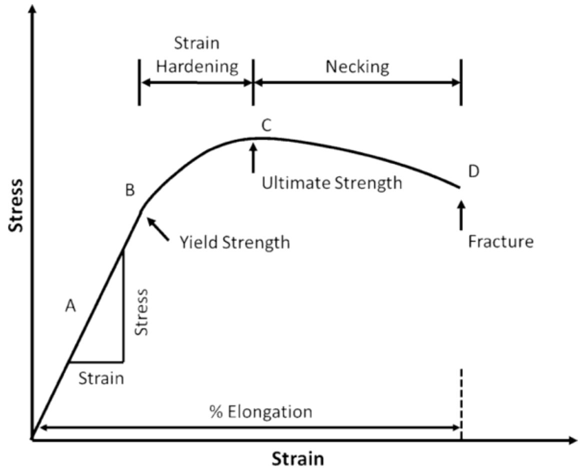

Figure 9: Yield and ultimate strength as defined by a stress-strain curve [14].

The tensile strength of a material is determined using a tensile test. It is the highest point on the stress-strain curve (figure 9) that can also be determined using the following equation [15]:

$$\sigma_f = \frac{P_f}{A_0} \tag{4}$$

where P_f is the load at fracture, A_o is the original cross-sectional area, and σ_f is the tensile strength, measured in Nm^{-2} or pascals [15].

Pervious sections have established the connection between degradation and molecular weight loss and by studying the effect of molecular weight on the tensile strength of polymers, *Flory's* studies give insight into how degradation might impact strength.

The study was completed using cellulose acetate and results confirm that the tensile strength of cellulose acetate depends on the number average molecular weight regardless of the molecular weight distribution. Additionally, *Flory* calculates the tensile strength (T_m) of blends composed of a mixture of cellulose acetate based on the following equation [16]:

$$T_m = \sum_i w_i \; T_i \tag{5}$$

where w_i is the weight fraction of a specific blend component and T_i is the tensile strength experienced by that component.

The results shown in figure 10 were used to define a general relationship between tensile strength and the molecular weight of polymers [16,17].

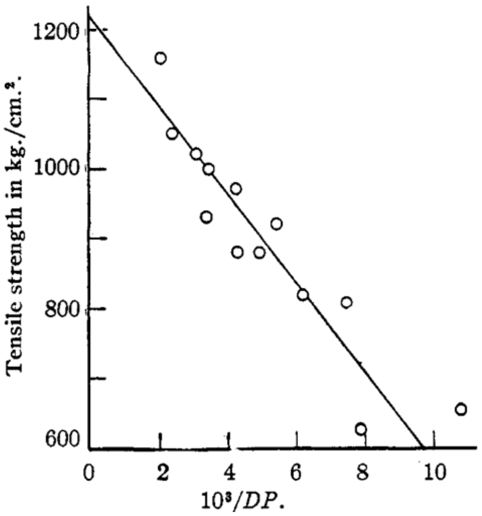

Figure 10: Tensile strength vs. reciprocal of chain length for cellulose acetate fractions [16,17].

The tensile strength (T) can be expressed as a function of molecular weight (M) based on the following equation [16]:

$$T = F\left(\frac{1}{M}\right) = a_0 + \frac{a_1}{M} + \frac{a_2}{M^2} + \cdots \qquad \textbf{(6)}$$

where a_0, a_1 and a_2 are numerical coefficients in the series expansion of $F\,(\frac{1}{M})$. The dependence of tensile strength on molecular weight is observed only when a_2 and higher coefficients are equal to zero. Most importantly, this type of analysis can be applied to other properties which likewise seem to depend on the number average molecular weight and exhibit additivity in their weight fractions **[16,17]**.

1.5. Tensile Loading

The application of an external force that results in elongating or stretching a body is known as tensile loading. It can be mathematical defined through tensile stress and strain based on Equations 7 and 8 and as illustrated by figure 11 **[18]**.

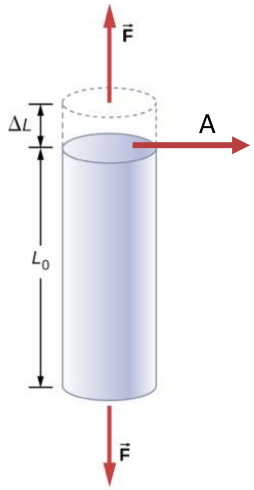

Figure 11: Tensile loading diagram used to mathematically define tensile stress and strain **[18]**.

$$Tensile\ Stress\ (\sigma) = \frac{Applied\ Force}{Cross\ Sectional\ Area} = \frac{F}{A} \qquad \textbf{(7)}$$

$$Tensile\ Strain\ (\varepsilon) = \frac{Elongation}{Orginal\ Lenght} = \frac{\Delta L}{L_0}\ ;\ where\ \Delta L\ > 0 \qquad \textbf{(8)}$$

In order to clarify the impacts of tensile load on polymer degradation, *Guo et al* carried out an *in vitro* degradation of poly(L-lactide-co-glycolide) (PLGA) membranes that were incubated in deionized water and five constant loadings (0.1, 0.2, 0.3, 0.4, 0.5 MPa) were applied to the specimens by hanging a dead weight during the experiments **[19]**.

Each specimen was cut into 50 mm long, 10 mm wide strips for mechanical testing and the tensile stress level was maintained constant during degradation. The mass loss, tensile elastic modulus (E) and tensile strengths (σ) of the membranes were measured each week until the membranes broke **[19]**.

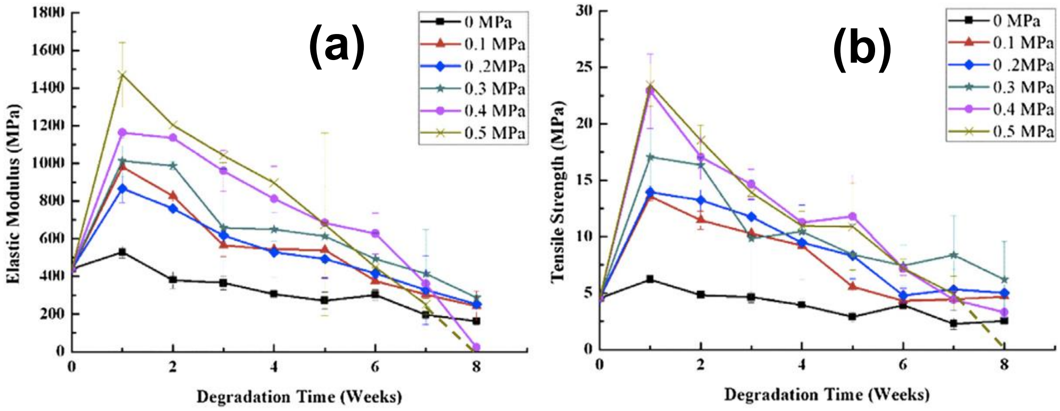

Figure 12: Changes in **(a)** elastic modulus and **(b)** tensile strength as a function of degradation time and different stress loads **[19]**.

The experimental results showed that over a range of tensile stresses, higher tensile stress might lead to quicker loss of mechanical properties **[19]**. Specifically, remarkable decrease in elastic modulus and tensile strength in 0.5 MPa group were observed and as seen from figure 12 **[19].**

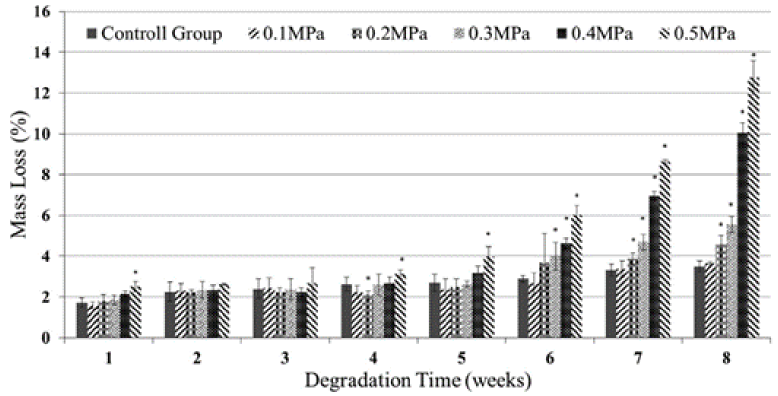

Figure 13: Mass loss rate as a function of degradation time with different stress loads where * indicates a statistically significant difference with respect to the control group **[19]**.

As the magnitude of tensile stress increased, more mass loss was observed in the loaded groups (figure 13) **[19]**. Based on these results, *Guo et al* concluded that the mass loss rate and mechanical properties of PLGA were sensitive to the tensile stress level during *in vitro* degradation **[19]**.

Similarly, *Deng et al* studied the effect of load on *in vitro* degradation behaviors of poly (glycolide-co-L-lactide) 90/10 multifilament braids by conducting strain-controlled experiments. Braided specimens were hung vertically on a rack and placed into a glass container (diameter = 200 mm, height = 180 mm) filled with a phosphate buffer solution (PBS) at 37°C and a pH of 7.4 **[20]**. The braid specimens were tested at room temperature immediately following their removal from PBS, i.e., in their wet condition to determine the breaking strength, Young's modulus and breaking strain at a crosshead speed of 127 mmmin^{-1} where the sample gauge length was equal to 80 mm **[20]**.

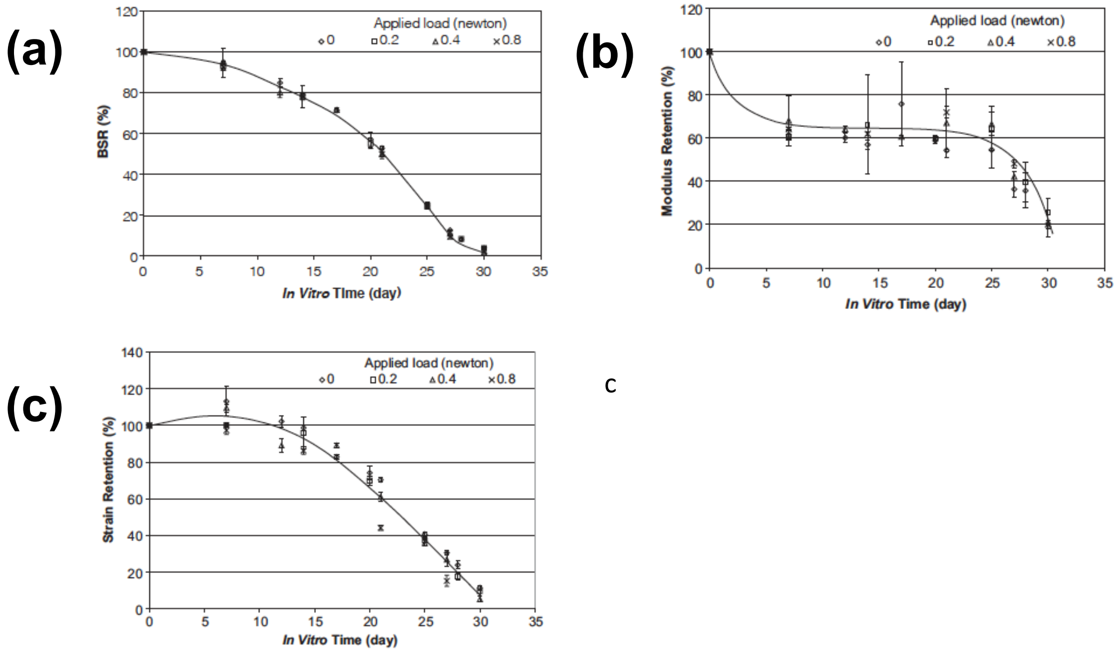

Figure 14: The effect of load as a function of degradation time on **(a)** breaking strength retention, **(b)** tensile modulus retention, **(c)** tensile breaking strain retention [20].

Based on the results shown in figure 14, *Deng et al* have demonstrated that there existed a well-defined relationship between strength, strain and molecular weight [20]. Additionally, and as a result of the degradation effect on the studied mechanical properties, surface morphology of the fibers showed significant change during degradation [20].

1.6. Compressive Loading

As opposed to tensile loading; compressive loading is defined as the application of an external force to contract an object or shorten it. Similar to the pervious section, the compressive stress and strain values can be defined based on Equations 9 and 10 and as illustrated by figure 15 [18].

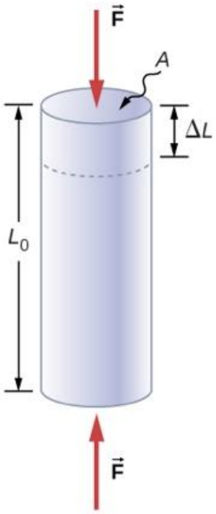

Figure 15: Compressive loading diagram used to mathematically define compressive stress and strain [18].

$$Compressive\ Stress\ (\sigma) = \frac{Applied\ Force}{Cross\ Sectional\ Area} = \frac{F}{A} \tag{9}$$

$$Compressive\ Strain\ (\varepsilon) = \frac{Elongation}{Orginal\ Lenght} = \frac{\Delta L}{L_0}\ ;\ where\ \Delta L\ < 0 \tag{10}$$

To determine the effect of compressive loading on polymer degradation, *Kang et al* studied the degradation properties of poly (L-lactic acid)/β-tri-calcium phosphate (PLLA/β-TCP) under dynamic loading [21].

Both PLLA and β-TCP are widely used in tissue engineering for the regeneration of bone tissue due to their biocompatibility and degradability [21]. However, the brittle nature of β- TCP confines clinical application to non-load-bearing repair and substitution [22,23]. Additionally, the acid degradation products of PLLA could result in aseptic inflammation, and their hydrophobicity can significantly affect cell penetration into the scaffolds [24].

To improve the bioactivity and mechanical properties so as to meet the basic requirement for bone repair, one potentially promising approach is to design a composite scaffold combining the advantages of these two biomaterials while attempting to avoid the limitations of each [21].

To prepare the composite scaffolds, *Kang et al* fabricated uniform and ultra-fine β-TCP powder through precipitation reactions while the PLLA was commercially obtained. Then, the composite porous scaffolds were fabricated using a solvent self-proliferating/model compressing/particulate leaching technique [21].

Using this preparation procedure, more than 30 scaffolds were fabricated and divided into two groups to complete the degradation experiments. The first group was immersed in a simulated body fluid (SBF) at 37°C with no dynamic loading. The second group was immersed in SBF and were placed in a customized dynamic flow chamber (figure 16) where dynamic loading was applied on the samples as they degrade [21]. Inside the chamber, the scaffolds were subjected to dynamic loading with 0.6 Hz and 0.1MPa for 6 weeks. The degradation behaviors of the scaffolds from both groups were systematically investigated through mass, porosity, and compressive strength changes [21].

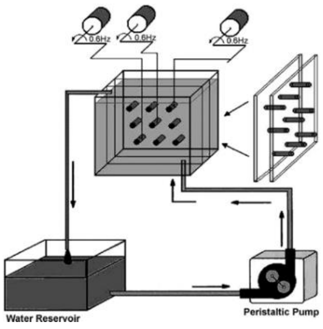

Figure 16: Schematic graph shows the apparatus for studying the degradation of degradable scaffolds in flow conditions using a peristaltic pump with dynamic loading using a minor motor [21].

Results confirm that changes in mass, porosity, and compressive strength of the scaffolds happened more under dynamic loading conditions than that under flow only SBF conditions (figure 17) [21].

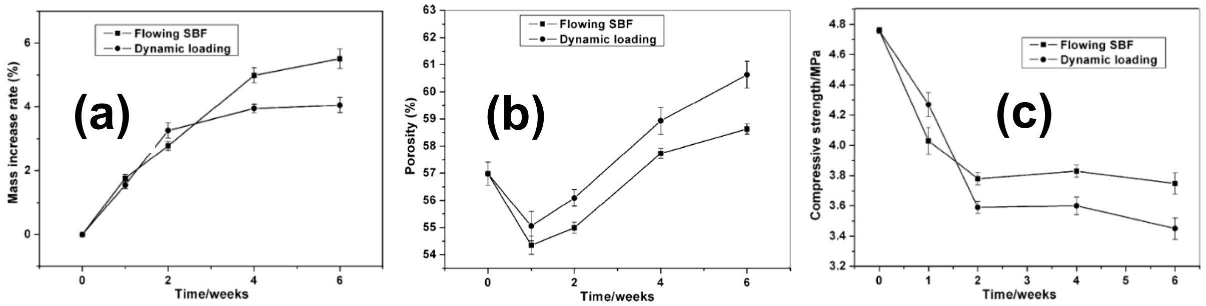

Figure 17: Changes in **(a)** mass, **(b)** porosity, **(c)** compressive strength of scaffolds as a function of degradation time under the two conditions [21].

Based on these results, *Kang et al* concluded that mechanical loading at the physiological level can promote the degradation of the scaffold, but the dynamic loading did not remarkably deteriorate the mechanical performance of the scaffolds [21]. Nonetheless, dynamic loading under flowing SBF conditions can accelerate the degradation of the PLLA/β-TCP composite scaffolds compared to the effect of SBF flow conditions without applied stress [21].

1.7. Viscoelasticity

The effect of dynamic stresses on degradation can be best studied through a material property known as viscoelasticity. This property is used to characterize materials that exhibit both viscous and elastic behavior while undergoing deformation (figure 18).

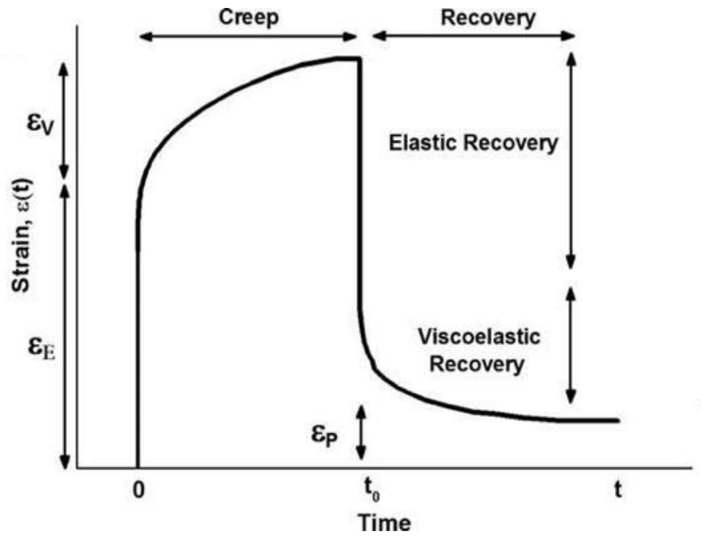

Figure 18: Schematic diagram of a viscoelastic response [25].

In other words, when stress is applied on a viscoelastic material, it causes temporary deformation when quickly removed (elastic recovery region in figure 18) but results in permanent deformation when maintained (viscoelastic recovery region in figure 18). Viscoelastic materials exhibit both elastic and dissipative response characteristics, in that they can store energy like elastic bodies and dissipate energy like viscous fluids [26]. Stress in a viscoelastic body relaxes (decreases) with time when strain is held constant. However, strain increases with time when a constant stress is prescribed as seen in the creep region of figure 18.

This behavior becomes especially interesting when studying degradable polymers because their mechanical properties exhibit a time-dependent response [26]. When it comes to understating the viscoelastic behavior of degradable polymers, efforts have been focused on how degradation effects the internal structure of polymers and their viscoelastic properties.

From a mechanical perspective, degradation means decreasing the load carrying capacity of the body. Although, the degradation due to the effect of moisture and temperature in elastic solids has been previously studied, *Muliana et al* wanted to extend applicability of this concept to include the response of viscoelastic solids **[26]**.

The mechanical response of a material depends on its molecular structure and is determined by the response at the molecular level due to an external stimulus **[26,27]**. Consequently, the rate of stress relaxation (or the rate of creep) in a linear viscoelastic body is determined by the body's internal structure **[26]**.

To study this, *Muliana et al* designed a degradable cylinder-shaped polymer to investigate the changes in its internal structure as a result of fluid diffusion (figure 19) **[26]**.

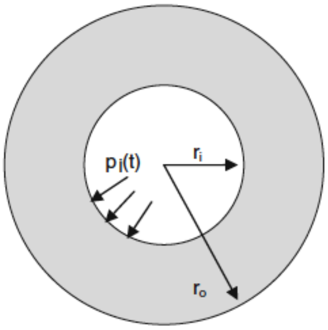

Figure 19: A viscoelastic cylinder where r_i is in the internal radius, r_o is outer radius and $p_i(t)$ is the internal pressure caused by fluid diffusion through the sample **[26]**.

where the governing equation of fluid diffusion through the cylinder was defined as follows **[26,28]**:

$$\frac{\partial c}{\partial t} = \frac{1}{r}\frac{\partial}{\partial r}\left(rD\frac{\partial c}{\partial t}\right) \tag{11}$$

C (r, t) is the concentration of fluid as function of radius and time and D is the diffusivity of the solid **[26]**. The mechanical viscoelastic response of the hollow cylinder was examined while undergoing continuous changes in its material properties due to the diffusion of a fluid through the cylinder **[26]**.

By subjecting the inner surfaces of a cylinder to uniform pressure, it was confirmed through FE simulation that the inner cylinder experiences higher stress as function of time (figure 20).

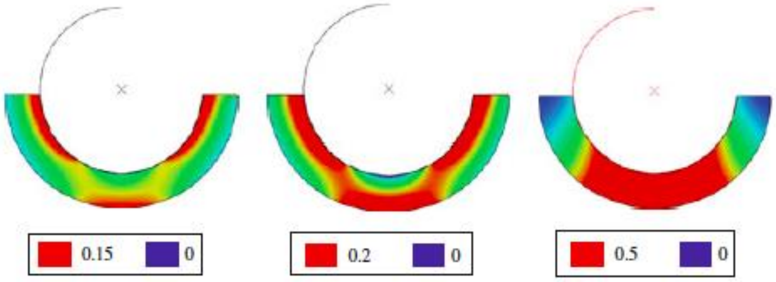

Figure 20: FE simulation of contact pressure created by fluid diffusion through the inner cylinder **[26]**.

This is most likely due to the effect of degradation on the internal structure of the polymer as the fluid flows through the material. From these results, *Muliana et al* believe that the relaxation response of viscoelastic bodies can be controlled through modification of their internal structure **[26]**.

Motivated by these results, *Breche et al* synthesized a degradable tri-block copolymer composed of Poly lactic acid (PLA) and Polyethylene glycol (PEG) to be used as scaffold for tissue engineering applications. Dog-bone tensile specimens were cut in 0.5 mm thick films with a specific punch of 14 mm in length and 2 mm wide gauge length. They were then placed in 20 mL test tubes and submitted to two times of degradation, 1 and 3 weeks, in phosphate buffer solution (PBS) at 37°C within an agitator/incubator **[29]**.

The *in vitro* experiment was designed so that the tensile (figure 21) and relaxation (figure 22) tests were performed at 6% strain during multiple time intervals throughout the degradation process. It’s important to note that the mechanical tests were conducted in solution at a controlled temperature of 37°C via a steel hermetic bath adjusted on the mechanical test machine in order to be in conditions that closely resemble *in vivo* ones **[29]**.

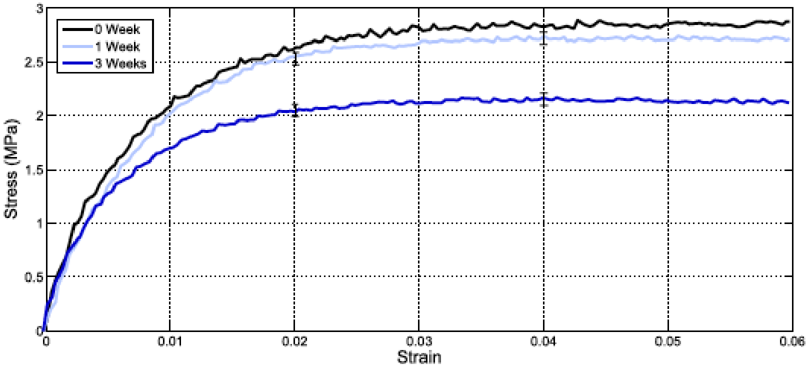

Figure 21: Experimental load curves at 6% strain at 0, 1, and 3 weeks of degradation [29].

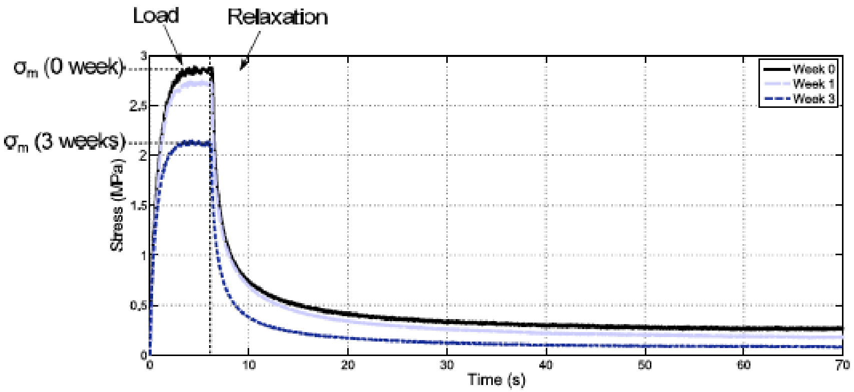

Figure 22: Experimental load and relaxation curves at 6% strain at 0, 1, and 3 weeks of degradation [29].

Based on these results, *Breche et al* were able to experimental demonstrate how the viscoelastic behavior of the PLA-b-PEG-b-PLA changed as function of degradation [29].

Capitalizing on the power of computational modeling, *El-Sayed et al* developed a constitutive framework for degradable polymers which accounts for non-linear viscous behavior under large deformation using the finite element software ABAQUS to perform real structural simulations. To capture this behavior, a degradable cylinder was designed to have an elastic outer layer and a viscoelastic inner layer [30].

By considering a deformation-induced degradation mechanism, a general contact analysis for a concentric cylindrical annulus under constant pressure was completed to observe the effect of degradation on the two layers, simultaneously [30].

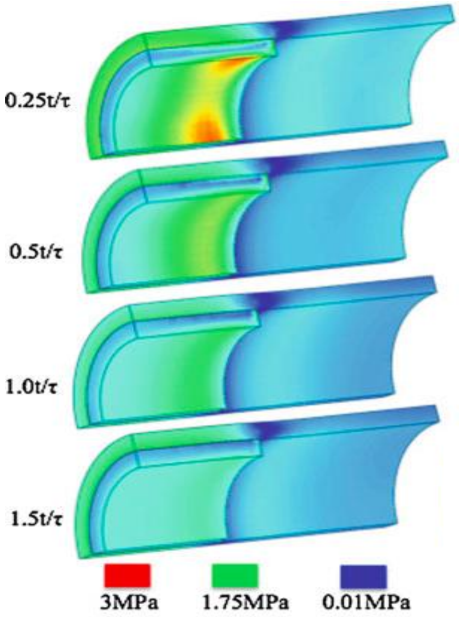

Figure 23: The effective stress contours at different nondimensional times (t/τ_D) [30].

Although the degradation rate was similar, *El-Sayed et al* concluded that during the ramping stage of loading, the outer elastic cylinder restrains the inner cylinder and caused the generation of more stress [30].

Additionally, the inner cylinder shows stress decay due to the strain softening effect, which is primarily due to the dominant viscoelastic attribute of the inner cylinder for the given loading condition and time studied (figure 23) [30].

1.8. Degradation & Erosion

1.8.1. Defining Degradation & Erosion

Degradation is the chemical process that triggers erosion. Therefore, it's important to distinguish between the two processes. By definition, degradation is the breakdown of the polymer's backbone. However, erosion designates the loss of material from the bulk of the polymer in the form of oligomers and monomers [31].

When it comes to degradation mechanics, hydrolysis is the most common path taken by degradable polymers. However, the actual hydrolytic event is just the initiation of the process in which polymers eventually disappear. After the initial attack by water, there are a series of events, including a decrease in the molecular weight (the number of bonds per chain) and a gradual loss of mechanical properties [32].

On the other hand, erosion is a physical process that is typically characterized by the mass loss of a polymer matrix [33]. In general, polymer erosion can be divided into two types; bulk and surface erosion. When a polymer experiences bulk erosion, material is lost from the entire polymer volume. In this case, the erosion rate depends on the total amount of material and decreases as the material is depleted (figure 24) [34].

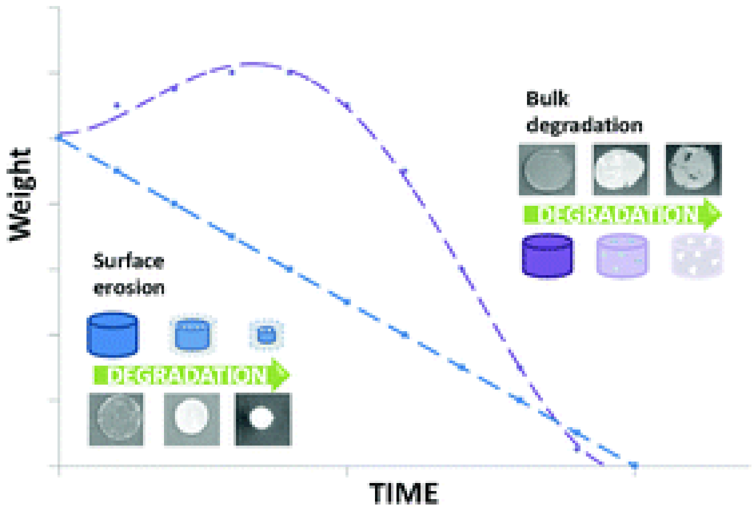

Figure 24: The difference between bulk and surface erosion based on weight loss as a function of time [35].

On the other hand, when a polymer exhibits surface erosion, the material is lost from the polymer matrix exterior surface. In this case, the erosion rate is directly proportional to the external surface area and the rate remains mostly constant until the polymer is completely eroded (figure 24) [34].

Different polymers can be designed to experience a certain kind of erosion based on their applications. For example, for degradable packaging, any erosion mechanism is satisfactory so long as the material maintains its integrity during use and disappears completely after disposal. However, for other applications, surface erosion is more desirable or possibly essential such as the case in drug delivery, where a surface-eroding polymer can provide constant and easily controllable drug release rates. Nevertheless, most polymers display bulk erosion patters, as surface erosion is difficult to achieve [34].

1.8.2. Experimental Studies

1.8.2.1. Degradation

Experimentally observing degradation is extremely difficult. Nevertheless, efforts by *Ali et al* were able to determine which mechanisms of polymer degradation are operative during *in vivo* degradation of poly(caprolactone) PCL and related polyesters [36].

By preparing PCL samples and implanting them into rat tissues, it was observed that hydrolytic degradation occurs in at least two discrete stages. The first involves bulk hydrolysis of ester linkages, auto-catalyzed by the carboxylic acid end groups of the polymer. While the second stage involves reactive oxygen free radicals that are produced by many biological systems within the rat's tissue [36].

Scanning Electron Microscopy (SEM) images were collected of implanted PCL samples and results show that the first phase lasts for at least 6 months [36]. It's important to note that hydrolytic degradation of semi-crystalline materials such as PCL generally involves a rapid chemical attack on the amorphous phase than that on the crystalline phase [36]. The difference in reaction rate leads to surface texture contrast in bulk crystallized samples that can be easily observed through SEM and as seen in figure 25.

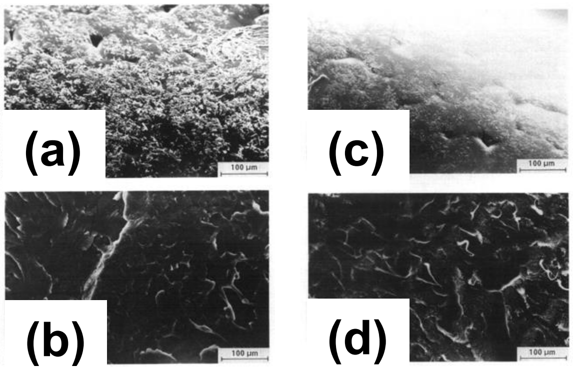

Figure 25: Scanning electron microscopy of **(a)** surface and **(b)** cross-section of virgin PCL vs. **(c)** surface and **(d)** cross-section of implanted PCL specimen after 30 weeks of degradation [36].

To investigate the effects of degradation over an extended period of time, *Mainil-Varlet et al* fabricated low molecular weight Poly(L/D-lactide) rods (figure 26) and used accelerated testing conditions to complete *in vitro* experiments **[37]**.

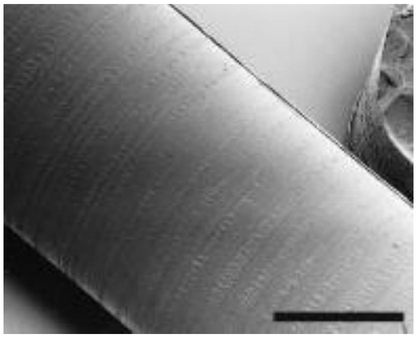

Figure 26: SEM Images of as-produced P(L/D) LA rod sample where the scale bar represents 1.38 mm **[37]**.

The samples were placed in glass vessels that were filled with a phosphate buffer solution and were kept in an incubator at 37°C. Over the course of 52 weeks, SEM images were taken to observe the effects of degradation as seen in figure 27 **[37]**.

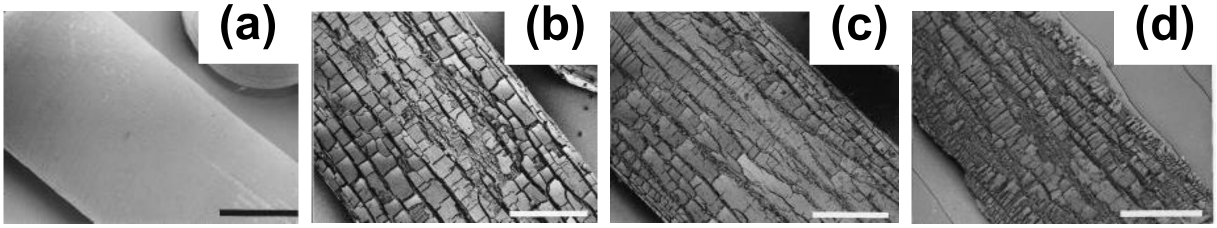

Figure 27: SEM Images of P(L/D) LA rods after aging for **(a)** 1 month, **(b)** 3 months, **(c)** 6 months and **(d)** 12 months **[37]**.

1.8.2.2. Erosion

To observe the effect of geometry on the erosion of polyanhydrides, *Akbari et al* fabricated cylindrical poly[1,3-bis(p-carboxyphenoxy) propane: sebacic acid], p(CPP:SA) matrices with diameters of 5, 9 and 12.5 mm, respectively. Then, they monitored the water absorption profile of the three samples by measuring the weight loss as a function of diameter **[14]**. Results in figure 28 show that the initial rate of decrease was related to the geometry where matrices of lesser thickness and diameter experienced faster rates of decrease **[38]**.

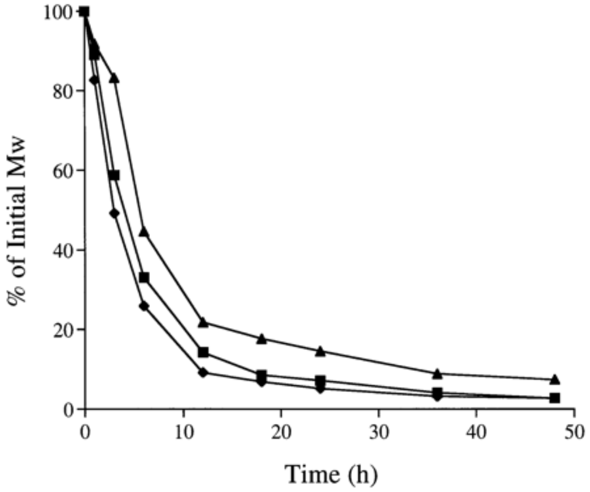

Figure 28: Molecular weight changes of p(CPP:SA) 40:60 polymer in matrices with diameters of (diamond) 5 mm, (square) 9 mm, and (triangle) 12.5 mm **[38]**.

This behavior is due to the gradual penetration of water from the surface into the matrix center, the thinner the matrix the shorter the time required for water to reach the center and hence the more rapid the reduction in molecular weight **[38]**.

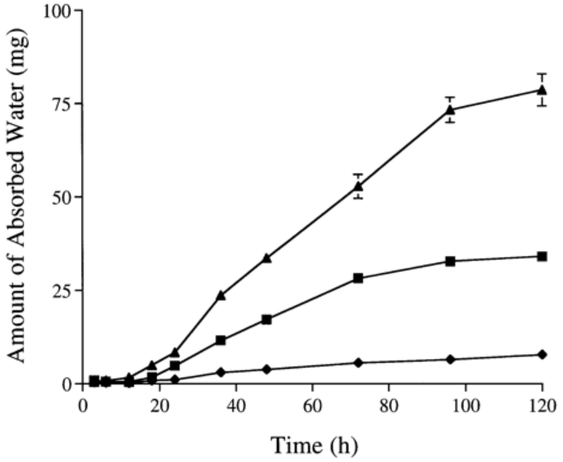

Figure 29: Water absorption profile of p(CPP:SA) 40:60 polymer in matrices with diameters of (diamond) 5 mm, (square) 9 mm, and (triangle) 12.5 mm [38].

Additionally, the device geometry had a significant effect on the water absorption profile (figure 29). Based on the collected data, the rates of water uptake were 0.9, 0.5 and 0.1 mgh^{-1} for diameters of 12.5, 9 and 5 mm, respectively [38].

Furthermore, to experimentally observe the complexity of erosion kinetics as function of mass, *Shieh et al* fabricated poly (Sebacic Acid), p(SA), homo-polymer disks with various thicknesses and volumes but identical diameters and surface areas [39]. The disks were immersed in a phosphate buffer solution with a 7.4 pH to monitor the erosion rate at 37°C.

As seen in figure 30, the collected data were used to generate a plot of rate in mg per hour (mgh^{-1}) vs. time in hours (h) and the following observations were made [39]:

- Initially, disks of all thicknesses show identical erosion rate profiles, with an induction period followed by a peak in erosion rate.
- After that, the erosion rate decreases, and a sharp distinction between the disks of different thicknesses develops, where the thicker disks show prolonged erosion at the peak rate.

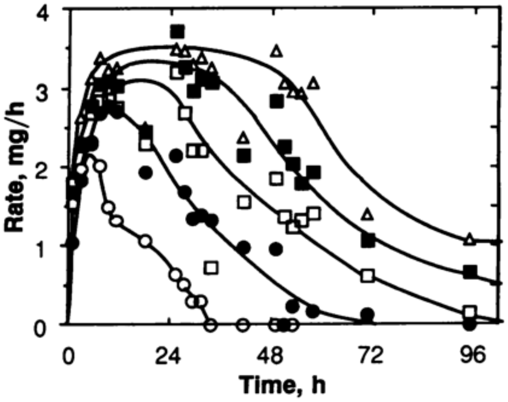

Figure 30: Rate of erosion p(SA) (M_r, 9000) disks. Mass and thickness of disks: (white circle), 47.41 mg and 0.38 mm; (black circle), 97.0 mg and 0.60 mm; (white square), 150.6 mg and 0.94 mm; (black square), 200.0 mg and 1.19 mm; (white triangle), 248.5 mg and 1.47 mm [39].

This means that material is being successively exhausted from the outside to the inside which indicates a steady advancement of the erosion zone (figure 31).

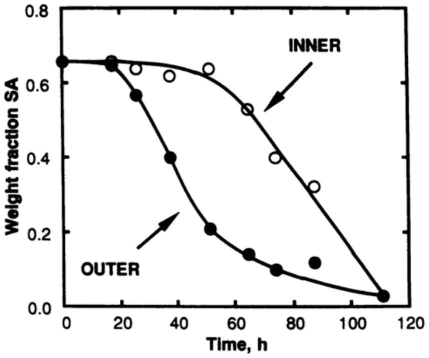

Figure 31: Composition of the outer and inner zones of p(CPP-SA) 20:80 mol% during erosion [34,39].

Initially, erosion takes place from the exterior of the disk; therefore, disks of different thicknesses and volumes with the same external surface area yield the same erosion kinetics. Based on that, *Shieh et al* concluded that it would take an erosion zone twice as long to reach the center of a disk that is twice as thick [34,39].

1.8.3. Mathematical Models

1.8.3.1. Degradation

For many commonly used degradable polymers such as PLA and PGA, there is a strong interplay between crystallization and the hydrolysis reaction. This is mostly due to the extra mobility of polymer chains provided by chain cleavage during hydrolysis where the resulting crystalline phase becomes more resistant to further hydrolysis. Additionally, and as stated in section 1, the interplay between the hydrolysis reaction, diffusion of reaction products and crystallization makes the mechanical properties of degradable devices difficult to predict **[40]**.

Therefore, *Han et al*. developed a model that accounts for the crystallization rate and how it changes throughout the degradation process.

The fundamental equations used were based on Avrami's theory of crystallization. The authors coupled the theory with diffusion-reaction equations to capture the desired behavior using Equations 12 through 14 where the variables are defined table 1 **[40]**.

$$\frac{dr}{dt} = k_1 C_e + k_2 C_e C_m^n \qquad \textbf{(12)}$$

$$\frac{dR}{dt} = (1 - X_c)\frac{dr}{dt} = k_1 C_e + k_2 \frac{C_e C_m^n}{(1-X_c)^n} \qquad \textbf{(13)}$$

$$\frac{dC_e}{dt} = -\frac{dR}{dt} - \frac{C_e}{1-X_c}\frac{dX_c}{dt} \qquad \textbf{(14)}$$

The developed model was able to illustrate that during degradation, the crystallization, hydrolysis reaction and diffusion are highly interconnected (figure 32) **[40]**.

Table 1: Definition of variables used in Equations 12 through 14 [40].

Variable	Definition
r	Mole number of the number of monomers produced by hydrolysis reaction per unit volume of amorphous polymer
k_1 & k_2	Reaction constants for the non-autocatalytic and auto-catalytic hydrolysis reactions
C_e	Mole number of Ester bounds of amorphous polymer per unit volume
C_m	Mole number of monomers remained in the material per unit volume of amorphous polymer
n	Power term that accounts for the dissociation of the acid end groups
R	Moles of monomers produced per unit volume of the semi-crystalline polymer. It also reflects the total number of chain cleavages per unit volume of the semi crystalline polymer
X_c	The volume degree of crystallinity

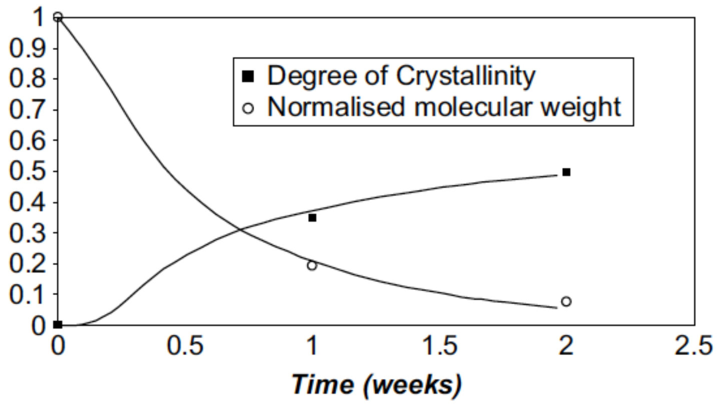

Figure 32: Average molecular weight and volume degree of crystallinity as a function of time of poly(glycolide-co-lactide). The continuous lines represent the model prediction while the discrete symbols are the experimental data [40].

The crystallization reduces the region where the hydrolysis reaction operates while the hydrolysis reaction encourages further crystallization. Thus, the diffusion process hinders the autocatalytic hydrolysis reaction and leads to weight loss [40].

Laycock et al were able to develop a model that can be used to established a relationship between chemical changes and engineering properties through degradation [41].

The changes to polymer strength over time may be related to the progressive increase in the number of polymer chain scissions that can in turn be linked to polymer degradation which is the basic principle used to complete the current model [16]. This was achieved by using Equation 15 that relates general strength (σ) to the Initial number average molecular weight $(\overline{M_{n0}})$ [41]:

$$\sigma = \sigma_{\infty} - \frac{B}{\overline{M_{n0}}\, e^{k' t}} \tag{15}$$

Where B is a material constant and σ_{∞} is the fracture strength at infinite molecular weight. The simulation results shown in figure 33 are based on different initial molecular weights and have been tested using the hydrolysis of PLA, poly (glyconate) and PLGA [41].

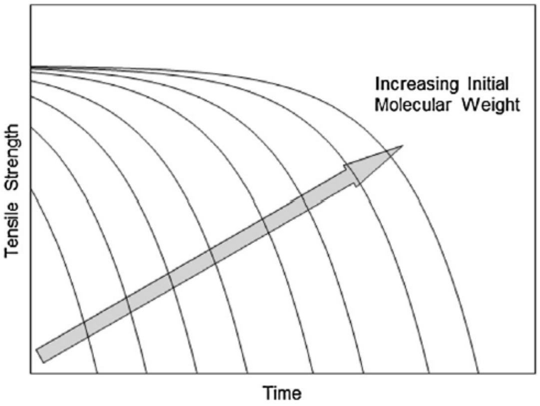

Figure 33: Plots of calculated tensile strength vs time of hydrolysis for different initial molecular weights using Equation 15 [41].

Additionally, the developed model offers the opportunity to visualize the processes that control the change in properties, recognizes the heterogeneity of the degradation process and how it impacts the mechanical properties as a function of time [41].

Vieira et al were able to investigate the evolution of the mechanical properties of PLA-PCL fibers during degradation by assuming that the hydrolytic reaction was the rate limiting step of the overall degradation process [42]. As seen from figure 34, the fibers became brittle, lost plasticity, and progressively decreased in strength after 16 weeks [42].

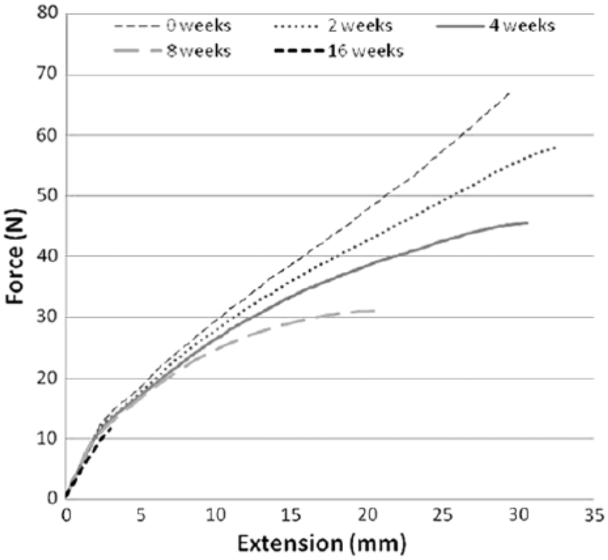

Figure 34: Tensile test results during degradation of PLA–PCL fibers (400 μm) [42].

It's important to note that the constant slope of the linear elastic region indicates that no significant variation in Young's modulus occurred during degradation [42]. By developing the current model, the degradation rate can be used as a failure benchmark when designing materials for biodegradable devices [42].

1.8.3.2. Erosion

As discussed in section 1.8.1, there are two types of erosion and mathematical models are used to explain why some polymers experience surface erosion while others undergo bulk erosion.

For example, it is theoretically known that polyanhydride polymers experience surface erosion. However, there was no clear explanation of why this is true and that is why *Göpferich et al* developed a model to understand the erosion behavior of polyanhydrides. Their work was able to explain why these polymers are surface eroding.

By using diffusion theory and Monte Carlo models, the authors developed a dimensionless erosion number (ε), which is defined based on the following equation **[43]**:

$$\varepsilon = \frac{\langle x\rangle^2 \lambda\pi}{4D_{\text{eff}}\left(ln[\langle x\rangle] - ln\left[\sqrt[3]{\frac{(\overline{M_n})}{N_A(N-1)\rho}}\right]\right)} \tag{16}$$

Where D_{eff} is the effective diffusivity of water inside the polymer, $\langle x\rangle$ is the device dimension, λ is the degradation rate of the polymer, M_n is the number average polymer molecular weight, N is the average degree of polymerization, N_A is Avogadro's number and ρ is the polymer density **[43]**.

When ε = 1, the erosion mechanism is not defined and a critical device dimension $L_{critical}$ can be calculated. If a matrix is larger than $L_{critical}$, it will undergo surface erosion. Otherwise, it will be bulk eroding **[43]**.

Using this criterion, polyanhydrides were estimated to be surface eroding down to a size of approximately 10^{-4} m, while poly (α-hydroxy acids) matrices need to be larger than 10^{-1} m to lose their bulk eroding properties and undergo surface erosion **[43]**. This erosion criteria were successfully illustrated by the authors in figure 35 based on the parameters defined in Equation 16 **[43,44]**.

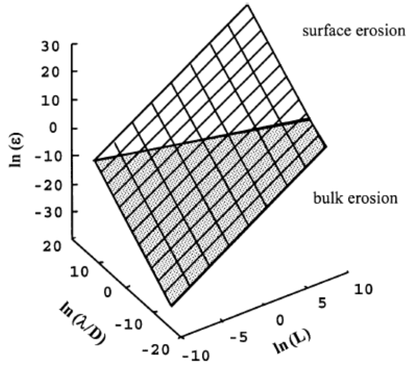

Figure 35: Dependence of the erosion number, ε, on the diffusivity of water inside the polymer, D_{eff}, the dimensions of a polymer matrix, L, and the polymer bond reactivity, λ, calculated from Equation 16. The white plane represents the area of surface erosion while the gray one represents the area of bulk erosion **[44]**.

1.9. Stress Corrosion Cracking

In general, stress corrosion cracking (SCC) is defined as the formation and growth of a crack when a material is placed in a corrosive environment. Normally ductile materials such as metal alloys and polymers can experience SCC which can lead to unexpected and sudden failure (figure 36). It's important to note that the effect of SCC on a material is accelerated in the presence of tensile stresses and elevated temperatures.

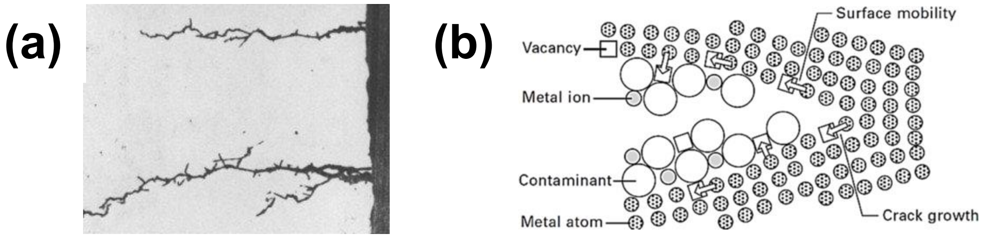

Figure 36: SEM image **(a)** and diagram **(b)** showing initiation and growth mechanism of stress corrosion cracking in stainless steel where contaminates are used to illustrated corrosive trigger [45,46].

However, the initiation of SCC requires specific environmental conditions, and only small concentrations of highly active chemicals/triggers are needed to produce catastrophic cracking that leads to devastating unexpected failure.

With this general definition in mind, the effect of SCC on degradable polymers can be defined at the molecular scale where atomic bonds break in response to a trigger, such as light or water [47]. Under such conditions and in the presences of an applied load, a stress concentrated crack can begin to form.

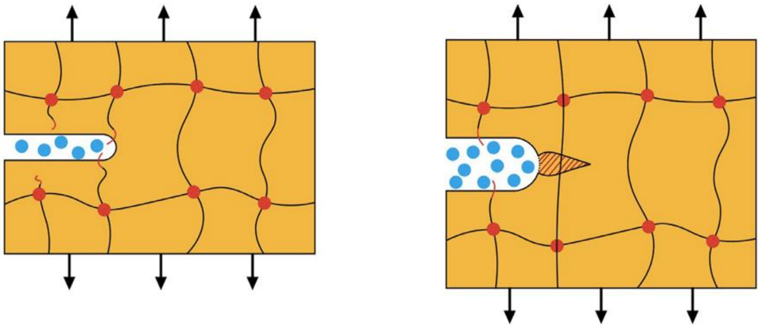

Figure 37: Bond breaking and crack growth in a degradable polymer as a response to water exposure where the blue dots are used to illustrate water molecules and the black arrows indicate the direction of the applied load [47].

Then, stress at the crack tip can lead to crack growth even when the magnitude of the load is small as seen in figure 37 [47]. Although Stress corrosion cracks have been observed in many materials, including silica glass, metals, natural rubber, non-degradable polymers, and conductive polymers, they have not been deeply studied in degradable polymers and some of the major studies are highlighted in this section [47].

Since stress is unavoidable in many applications of degradable polymers, recent work has focused on the evaluation and prediction of their properties under stress in a corrosive environment [48]. The influence of static tensile loading on polymers is commonly evaluated by the modified Arrhenius equation as follows [49,50]:

$$K = K_0 \exp\left[-\frac{(E_A - \alpha\sigma)}{RT}\right] \tag{17}$$

where K_0 is the Arrhenius frequency factor, K is the rate of bond rupture events, E_A is the activation energy, σ is the tensile stress, and α is the coefficient. According to Equation 17, static tensile stress increases the activation energy leading to the accelerated degradation of the degradable polymers [48].

To experimentally observe the effect of stress corrosion cracking in poly (D, L-lactic acid) (PDLLA), *Fan et al* designed a device that would supply different loads during the *in vitro* degradation process shown in figure 38 **[51]**. The results collected under different loads were compared with those without load and were used to understand the influence of load on degradation rates **[51]**.

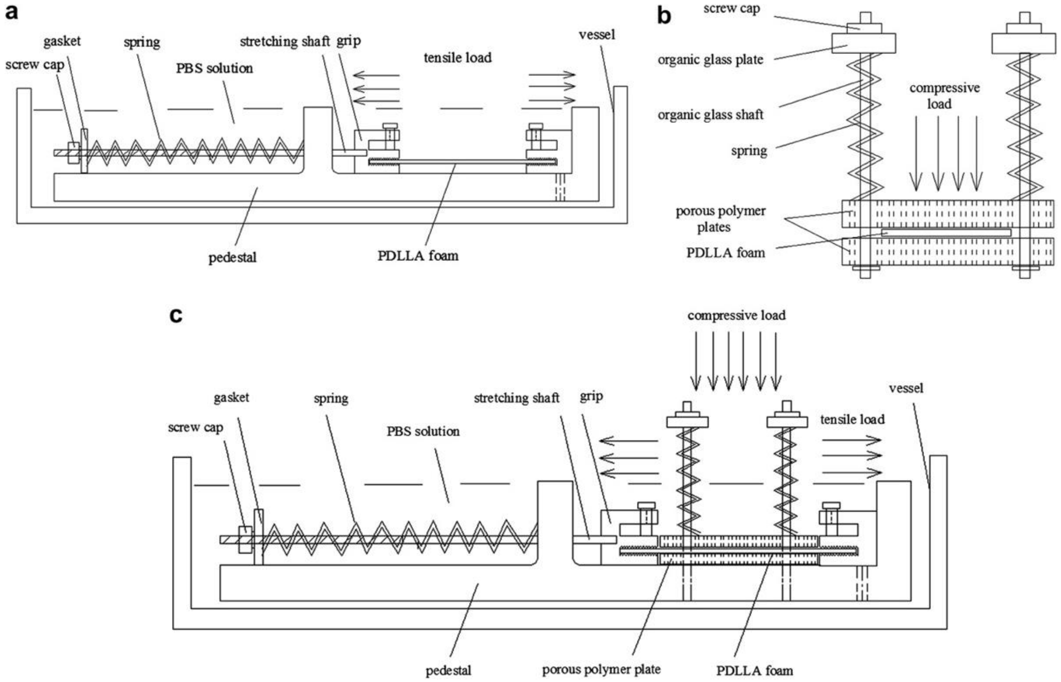

Figure 38: Self-made load-providing devices for **(a)** tensile load; **(b)** compressive load and **(c)** tensile-compressive combined load **[51]**.

PDLLA foam gaskets were fastened on the loading device and placed in a glass vessel containing phosphate buffer saline (PBS) with 7.4 pH and at a constant temperature of 37°C **[51]**. The degradation experiment was carried out in a drying cabinet for the duration of 3 months **[51]**.

Based on these conditions and using the load devices seen in figure 38, *Fan et al* conducted four types of loaded tests that are categorized into two series:

Series A:

- Test # 1 - PDLLA under 15 N tensile load
- Test # 2 - PDLLA under 15 N tensile load combined with 100 N compressive load

Series B:

- Test # 3 - PDLLA under 25 N tensile load
- Test # 4 - PDLLA under 25 N tensile load combined with 100 N compressive load

The unloaded control experiments were conducted using the tensile load-providing device but without tensile load [51]. At weekly intervals, the PBS solution was refreshed to prevent the effect of acidic degradation products [51]. Three samples were taken out from the degradation system for characterization at the end of each month [51]. Over the course of three months, *Fan et al* recorded the changes in molecular weight, elastic modulus, mass loss and tensile strength [51].

The results seen in figure 39 confirm that the degradation rates of PDLLA under continuous loads were obviously quicker than those without load [51]. Moreover, the influence of tensile plus compressive load was larger than that of tensile load alone [51].

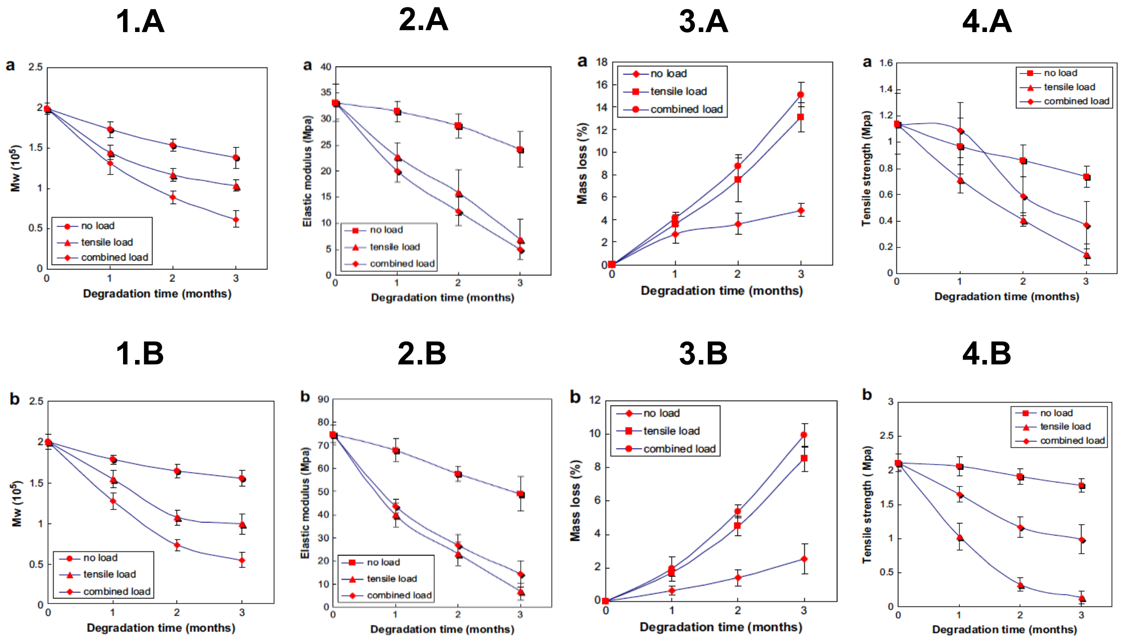

Figure 39: The changes in **(1)** molecular weight, **(2)** elastic modulus, **(3)** mass loss and **(4)** tensile strength as a function of degradation time where the symbols A and B represent the respective test series discussed on page 45 [51].

This indicates that *in vivo* degradation of PDLLA is not only influenced by the local solution, but also by the applied load [51]. Additionally, and since experimental conditions match those of stress corrosion cracking (applied load in combination with a corrosive environment), these results highlight the significance of this phenomena and its accelerated impact on polymer degradation.

Using similar experimental conditions, *Shi et al* were able to establish a relationship between crack growth and surface erosion in the presence of an applied load in poly (glycerol sebacate) (PGS) which is a degradable elastomer that was developed for medical applications [47].

The elastomer is a polyester in which ester bonds hydrolyze in the presence of water molecules. Because of that, *Shi et al* prepared PGS samples with a pre-cut crack, applied various loads, and recorded crack growth using a camera as seen in figure 40 [47].

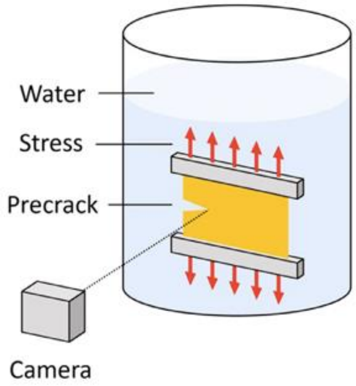

Figure 40: Experimental setup where a pre-cut PGS sample is stretched to a constant strain, submerged in DI water, and observed by a camera [47].

The application of a small load opens the pre-cut crack in PGS and provides a path for water molecules to reach the crack tip [47]. This accelerates hydrolysis at the crack and allows the crack speed to become orders of magnitude higher than the speed of surface erosion [47].

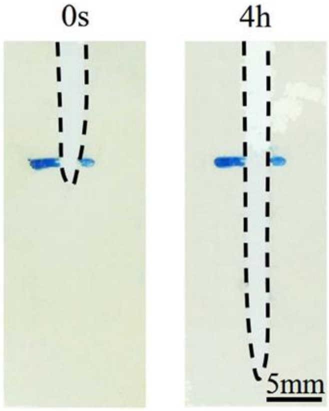

Figure 41: The application of a constant strain that is equivalent to an energy release rate of 19.2 Jm^{-2} allows the crack to advance 3.5 cm in 4 hours [47].

The crack velocity is calculated based on the results shown in figure 41 by dividing the observed crack growth by the time between images [47]. Data analysis confirms that the crack length increases linearly with time, indicating a constant crack velocity [47]. Where the average crack velocity was calculated to be 1.15 x 10^{-6} ms^{-1} [47].

Additionally, and to determine the depends of crack speed on the applied load, this experiment was repeated using several values of energy release rates where the final results are summarized in figure 42.

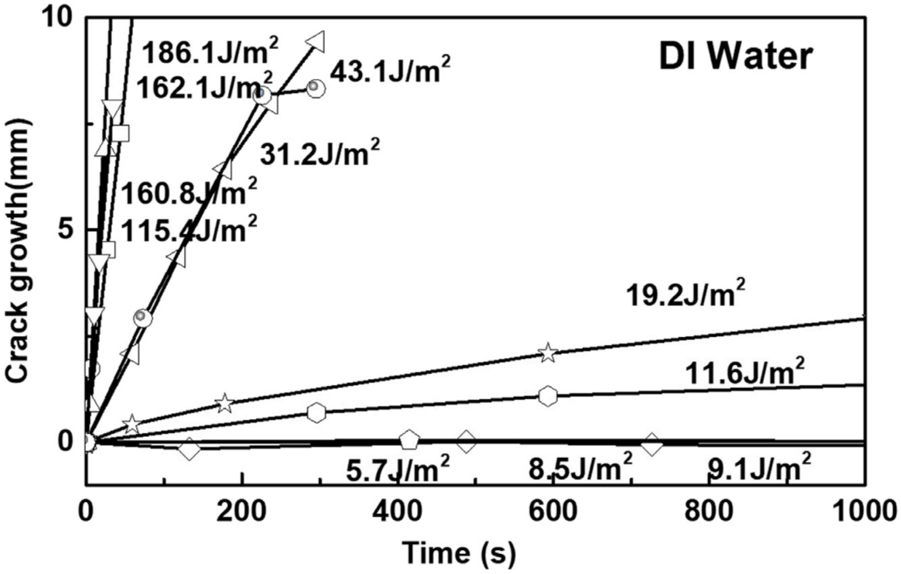

Figure 42: Crack growth as a function of time, where each line represents a crack advancing in a sample subject to a value of energy release rate [47].

When the environmental conditions are fixed, *Shi et al* identify two regimes of crack growth: one that is sensitive to the magnitude of the applied load, and another that is not. At small values of energy release rate, the crack speed increases steeply with energy release rate. The crack speed reaches ~2x10^{-5} ms^{-1} at an energy release rate of 50 Jm^{-2}, which is six orders of magnitude greater than that of erosion (figure 43) [47].

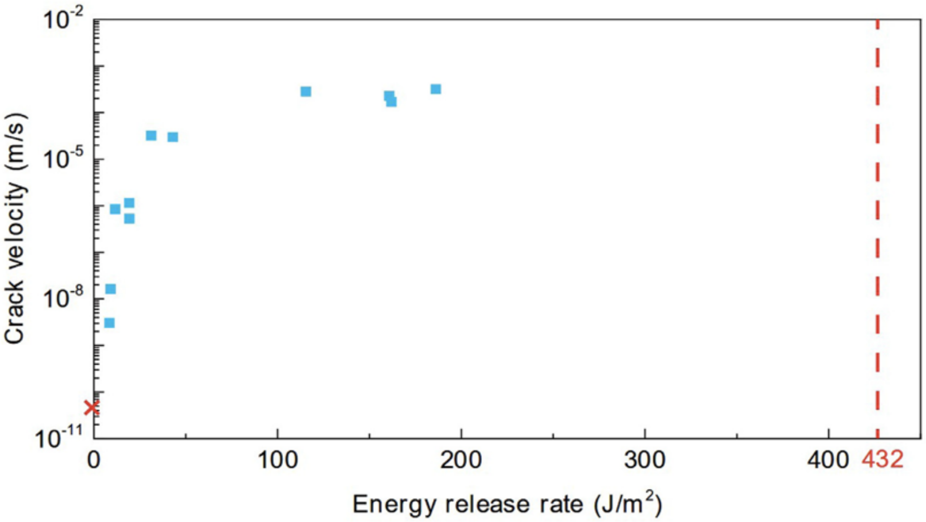

Figure 43: Crack speed of PGS in DI water measured at various values of energy release rate [47].

At an energy release rate of ~70 Jm^{-2}, the crack speed plateaus at ~2x10^{-4} ms^{-1}, and becomes insensitive to the magnitude of the energy release rate (figure 43) [47]. Based on these results, *Shi et al* concluded that hydrolytic cracks can cause degradable polymer to lose their load-carrying capacity prematurely, and fragment the polymer into particles which can lead to serious complications when used in medical applications [47].

1.10. Chapter Conclusions

A review of the time-sensitive properties of degradable polymers was provided firstly by exploring a range of mechanical properties including elasticity, toughness, strength, viscosity, and stress corrosion cracking through experimental efforts and computational models that have been developed to study commonly used degradable polymers. More importantly, we focus our attention on polymer erosion and degradation by presenting a range of mathematical models and recent experimental results that highlight the importance of these two phenomena.

Although many efforts have been dedicated to studying the effects of degradation and erosion, much more research needs to be done before we can gain a deeper understanding of how the mechanical properties change as a function of material degradation. Therefore, the investigations presented in this dissertation have been focused on coupling the effect of mechanical loading with degradation. With the results presented in the coming chapters we aspire to provide the scientific community with a benchmark on how the mechanical properties of polymers change as a function of degradation and in the presences of external factors such as high pH, stress and strain.

Also, most of the studies found in the literature have been focused on PLA, PCL and various ratios of PLLA. Because of that, we focus our efforts on hydrogels and a photocurable degradable elastomer known as PGSA.

We believe that our research findings have not only accelerated our understating of these polymers but will also help expand their application envelope along with providing the scientific community with a wider range of sustainable starting materials.

Chapter 2

Tailorable Non-linear Viscoelasticity of Hydrogels

2.1. Introduction & Background

Hydrogels are a special kind of polymer-based gel composed of a three-dimensional hydrophilic polymer network in which a large amount of water is interposed [52]. Depending on the type of the crosslinkers, hydrogels can be categorized into covalently (or chemically) crosslinked gels and ionically (or physically) crosslinked gels [53]. In a hydrogel, hydrophilic polymers can retain a large amount of water, and this gives hydrogels unique proprieties that make them suitable for many applications in the biomedical field, active devices, soft robots, and environmental engineering [52,54]. Examples of the applications of hydrogels include scaffolds for tissue engineering, vehicles for drug delivery, actuators for optics and fluidics, and model extracellular matrices for biological studies [54].

Inspired by nature, and since most tissues found in animals and plants are composed of hydrogels [55], many synthetic hydrogels have been designed to mimic the behavior of natural tissue. Some of the most common polymers used include alginate, a naturally occurring polysaccharide co-polymer found in brown seaweed that is composed of irregular block arrangements of α-L-guluronate (G-Block) and β-D-mannuronate (M-Block) [56]. Another commonly used polymer is polyacrylamide (PAAm) which is a synthetic linear polymer often composed of acrylamide monomer units or a combination of acrylamide and acrylic acid [57].

As stated previously, hydrogels are composed of long polymer chains that constantly interact within the gel's network [58,59]. This often gives rise to complex viscoelastic behavior, which may result from various microscopic processes including sliding between polymer chains, temporary bond formation and breakage etc. [58-60]. Recent studies have found that viscoelasticity of soft tissues plays an important role in many biological processes including regulating cell behaviors, differentiation, and malignancy [61-64]. Consequently, lots of efforts have been dedicated to developing hydrogels with tunable viscoelasticity that closely match the behavior of biological tissues [65,66]. Moreover, theoretical frameworks have been formulated which highlight the dynamic, time-dependent behavior of self-healing gels transient polymer networks, and dual crosslink gels all of which have significantly advanced the biomedical applications of hydrogels [67-70].

In the current study, we aim to conduct systematic investigations of the viscoelastic behavior of hydrogels. It has been known that due to the low viscosity of water, the resistance to the movement of the polymer chains in a hydrogel is very small. As a result, covalently crosslinked hydrogels typically exhibit hyperelastic behavior with little viscous effects or mechanical dissipation. In contrast, for an ionically crosslinked hydrogel such as Ca^{2+} crosslinked alginate, the ionic bond can be unzipped by external forces, which is a rate-dependent process and can dissipate energy. As a result, an ionically crosslinked hydrogel usually exhibits significant viscoelastic properties. Though the viscoelasticity of an ionically crosslinked hydrogel has been often ascribed to the ionic debonding process, according to our knowledge, quantitative analyses correlating the macroscopically viscoelastic behavior of multi-bonded hydrogels with the microscopic ionic debonding process has yet been done. Moreover, it is reasonable to expect that the dynamic ionic debonding process in a hydrogel is force dependent. Therefore, the time scales associated with viscoelastic behaviors of a hydrogel should also be dependent on its external load. Recent work has also shown that the load-dependent stress relaxation of hydrogels can profoundly affect their fracturing process [71]. However, in most of the previous studies, the time scale (s) associated with the viscoelasticity of ionically crosslinked hydrogels are assumed to be constant.

In this work, we conduct stress relaxation experiments to systematically study the viscoelastic behavior of four different hydrogels: covalently crosslinked PAAm, covalently crosslinked PAAm network immersed in a viscous alginate solution, ionically crosslinked alginate, and crosslinked PAAm-alginate double network. We found that we can tailor the viscoelastic behavior of a covalently crosslinked PAAm hydrogel by increasing the viscosity of the aqueous solution in which the polymer network is immersed. We have also demonstrated that the macroscopically measured force-dependent viscoelastic behavior of ionically crosslinked alginate gel and PAAm-alginate double network gel can be quantitatively interpreted by the microscopic ionic debonding process in the gel.

2.2. Hydrogel Synthesis

The hydrogels were prepared by following the previous work **[54]**. Briefly, the 2wt% alginate gel was prepared by mixing 2.5 g of medium viscosity alginic acid sodium salt from brown algae (Sigma-Aldrich A2033) with 122.5 g of deionized water where 2.5vol% Calcium Sulfate dihydrate ($CaSO_4.2H_2O$, Sigma-Aldrich C3771) was used as a crosslinker. The 8wt% PAAm gel was prepared by mixing 10 g of Acrylamide (Sigma-Aldrich 79-06-1) with 115 g of deionized water where 0.96vol% N,N′-Methylenebisacrylamide (2wt% MBAA, Sigma-Aldrich 146072) was used as a crosslinker, 1.53vol% Ammonium persulfate (0.27 M APS, Sigma-Aldrich A3678) was used as an initiator and 0.055vol% Tetramethylethylenediamine (TEMED, Sigma-Aldrich T9281) was used as a catalyst.

The double network hydrogel was fully crosslinked and prepared by homogenously mixing the 2wt% alginate and 8wt% PAAm solutions while using the same amount of $CaSO_4.2H_2O$, MBAA, APS and TEMED. The immersion of covalently crosslinked PAAm network in a viscous alginate solution was achieved by using the same procedure for the double network. However, the $CaSO_4.2H_2O$ ionic crosslinker was eliminated to keep the alginate chains in linear form.

2.3. Experimental Methods

2.3.1. Sample Preparation

A 30 mL syringe was used as a mold to create cylindrical-shaped samples for compression testing. After 24 hours of crosslinking 10 mL of the desired gel, the cylindrical shaped sample was removed from the mold where the average value of the diameter was equal to 22.5 mm and the diameter to length ratio was kept at 1:1. After that, the sample was fully immersed in a silicon oil bath to prevent water evaporation throughout the test.

2.3.2. Stress Relaxation Test

Using the 10 N load cell on the Instron (Model # 3345), a compressive strain was applied on each hydrogel and was held constant for 3 hours. This setup (figure 44) was used to conduct different compression experiments on each hydrogel starting with 5% compressive strain followed by 10%, 15% and 20% compressive strain.

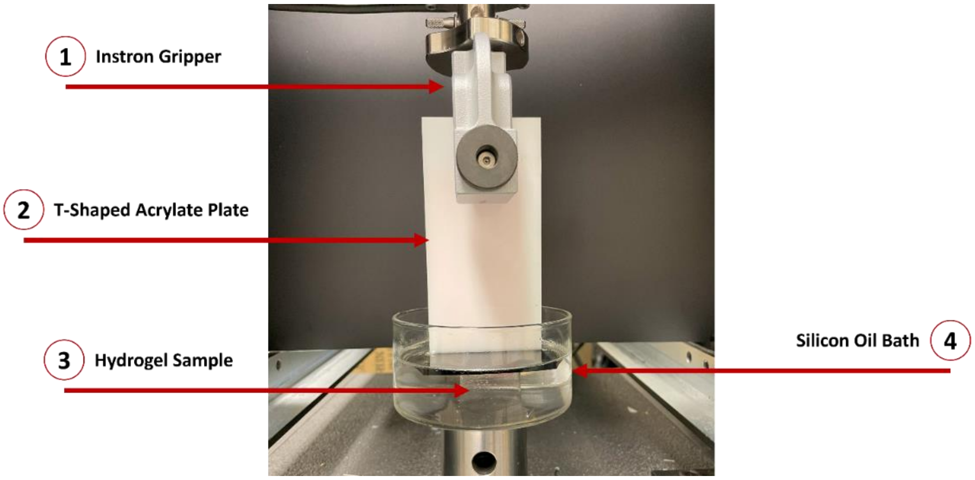

Figure 44: The 10 N Instron load cell was used to apply a compressive strain on the sample which was held constant for 3 hours where the sample was fully immersed in a silicon oil bath to prevent the evaporation of water throughout the experiment.

In each experiment, the time to reach maximum compressive strain was equal to 2 seconds through adjusting the compressive strain rate. For instance, 2.5% s^{-1} rate was used during the 5% compression test while 5% s^{-1}, 7.5% s^{-1} and 10% s^{-1} were used during the 10%, 15% and 20% compression tests respectively. Throughout the experiment, the stress was recorded as a function of time to characterize the stress relaxation behavior of the prepared hydrogels.

2.4. Model of Non-linear Viscoelasticity of Hydrogels

Viscoelastic relaxation of hydrogels can be represented by a rheological model of springs and dashpots. Here, we adopt a simple rheological model of two parallel units: one unit consists of a spring (α), and the other unit consists of a spring (β) and a dashpot, as shown in figure 45. It is easy to see that for this simple rheological model, only one relaxation time is captured, corresponding to the primary relaxation of the hydrogel.

In a principal coordinate, for spring α, the state of deformation can be described by three principle stretches of the hydrogel : $\lambda_1, \lambda_2 \text{ and } \lambda_3$; however, for spring β, the state of deformation is given by $\lambda_1\xi_1^{-1}$,$\lambda_2\xi_2^{-1} \text{ and } \lambda_3\xi_3^{-1}$, where $\xi_1, \xi_2 \text{ and } \xi_3$ are used to describe dashpot deformation.

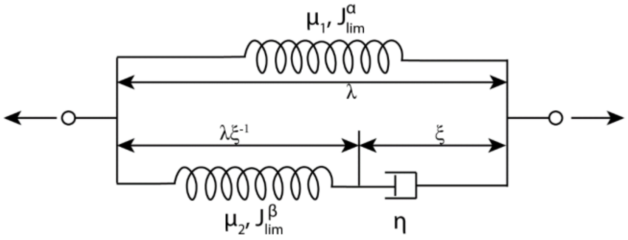

Figure 45: Rheological model used to obtain fitting parameters based on experimentally observed stress relaxation behavior where $\mu_1$and μ_2 are the shear moduli for springs α and β, respectively. The viscosity of the dashpot is described by η , λ is the applied stretch, ξ is used to describe dashpot deformation under uniaxial compression while the J^{α}_{lim} and J^{β}_{lim} values represent chain extensibility of springs α and β, respectively.

In a principal coordinate, the free energy density of the hydrogel is:

$$W = -\frac{\mu_1 J^{\alpha}_{limit}}{2}\ln\left(1-\frac{\lambda_1^2+\lambda_2^2+\lambda_3^2-3}{J^{\alpha}_{limit}}\right)-\frac{\mu_2 J^{\beta}_{limit}}{2}\ln\left(1-\frac{\lambda_1^2\xi_1^{-2}+\lambda_2^2\xi_2^{-2}+\lambda_3^2\xi_3^{-2}-3}{J^{\beta}_{limit}}\right), \qquad \textbf{(18)}$$

where μ_1 and μ_2 are shear moduli of springs α and β, respectively, and J_{limit}^{α} and J_{limit}^{β} are constants related to the limiting stretches of the two springs.

For a uniaxial compression test along direction 1, we have:

$$\lambda_1 = \lambda \, , \tag{19}$$

$$\lambda_2 = \lambda_3 = \lambda^{-\frac{1}{2}} \quad , \tag{20}$$

and

$$\xi_1 = \xi \quad , \tag{21}$$

$$\xi_2 = \xi_3 = \xi^{-\frac{1}{2}} \; . \tag{22}$$

So, the free energy density of the gel under uniaxial compression can be simplified as

$$W = -\frac{\mu_1 J_{limit}^{\alpha}}{2} \ln\left(1 - \frac{\lambda^2 + 2\lambda^{-1} - 3}{J_{limit}^{\alpha}}\right) - \frac{\mu_2 J_{limit}^{\beta}}{2} \ln\left(1 - \frac{\lambda^2 \xi^{-2} + 2\lambda^{-1}\xi - 3}{J_{limit}^{\beta}}\right). \tag{23}$$

we assume that for alginate gel and double network, $J_{limit}^{\alpha} = J_{limit}^{\beta} = J_{limit}$; while, for PAAm gel dissolved in water and immersed in alginate solution, $J_{limit}^{\alpha} = J_{limit}^{\beta} = \infty$ which reduces the Gent model to the Neo-Hookean model. According to Equation 23, the Cauchy (true) stress can be written as:

$$\sigma = \lambda \frac{\partial W}{\partial \lambda} = \sigma_1 + \sigma_2 = \frac{\mu_1(\lambda^2 - \lambda^{-1})}{1 - \frac{\lambda^2 + 2\lambda^{-1} - 3}{J_{limit}^{\alpha}}} + \frac{\mu_2(\lambda^2 \xi^{-2} - \lambda^{-1}\xi)}{1 - \frac{\lambda^2 \xi^{-2} + 2\lambda^{-1}\xi - 3}{J_{limit}^{\beta}}} \; , \tag{24}$$

where σ_1 is the stress on the spring α, and σ_2 is the stress on the spring β and the dashpot. The viscous behavior of the dashpot in figure 45 can be described by a Newtonian fluid as:

$$\frac{d\xi}{\xi dt} = \frac{\sigma_2}{3\eta} \; , \tag{25}$$

where η is the shear viscosity of the dashpot. Using the viscosity of dashpot η and the shear modulus of the spring μ_2, we can describe the primary relaxation time as:

$$\tau = \frac{\eta}{\mu_2}. \qquad \textbf{(26)}$$

For our stress relaxation test, the stretch λ is fixed. With knowing the material parameters: μ_1, μ_2 and τ, a combination of Equations 24, 25, and 26 allows us to predict the stress relaxation with time, namely, $\sigma(t)$. Likewise, we can obtain those material parameters by fitting the theoretical predictions with the experiment results.

2.5. Results & Discussion

2.5.1. Viscoelasticity of Covalently Crosslinked PAAm Gel

When AAm monomers are dissolved in water, they form an elastic covalently crosslinked PAAm hydrogel network (figure.46.a). However, upon the immersion of PAAm chains in a viscous alginate solution, the formed hydrogel network (figure.46.b) is expected to behave differently under compressive strains.

Upon the application of constant compressive strain, the covalently crosslinked PAAm gel experiences hyperplastic behavior with minimum relaxation over a long period of time as seen in the stress vs. time curves in figure.46. We expect this type of elastic behavior because the permanently crosslinked polymer network is immersed in water which has very low viscosity.

But under the same compressive strain, and as more alginate solution is added into the network, obvious viscoelastic behavior is observed. At 5% compression (figure.46.c), the PAAm gel (0wt% Alg) has a maximum stress (σ_{max}) value of 0.178 kPa and an equilibrium stress (σ_0) value of 0.136 kPa confirming minimal relaxation behavior. However, and when exposed to the same compressive strain of 5%, the PAAm network immersed in 3wt% alginate solution starts with a σ_{max} value of 0.42 kPa and reaches a σ_0 of 0.32 kPa at the end of the test.

In this case, the relaxed stress $\Delta\sigma$ of 0.1 kPa is generated by the viscous alginate solution while the PAAm gel dissolved in water had $\Delta\sigma$ of 0.037 kPa confirming how the two gels behave differently under the same constant compressive strain. As higher compressive strains are applied on the gels, the effect of alginate viscosity on the viscoelastic behavior of the gels becomes more apparent. For example, when the applied compressive strain is equal to 10% (figure.46.d), the PAAm gel still behaves elastically with a σ_{max} that is equal to 0.53 kPa and σ_0 of 0.49 kPa ($\Delta\sigma = 0.04$ kPa). We compare this to the behavior of the PAAm gel immersed in 2wt% alginate under the same compression and find that the $\Delta\sigma$ is equal to 0.102 kPa. This is also true when a 20% compressive strain is applied (figure.46.e) and the viscoelastic behavior is observed even with the PAAm gel immersed in as little as 0.5wt% alginate where the $\Delta\sigma$ is equal to 0.09 kPa, while the pure PAAm gel still exhibits elastic behavior and has a $\Delta\sigma$ of 0.04 kPa.

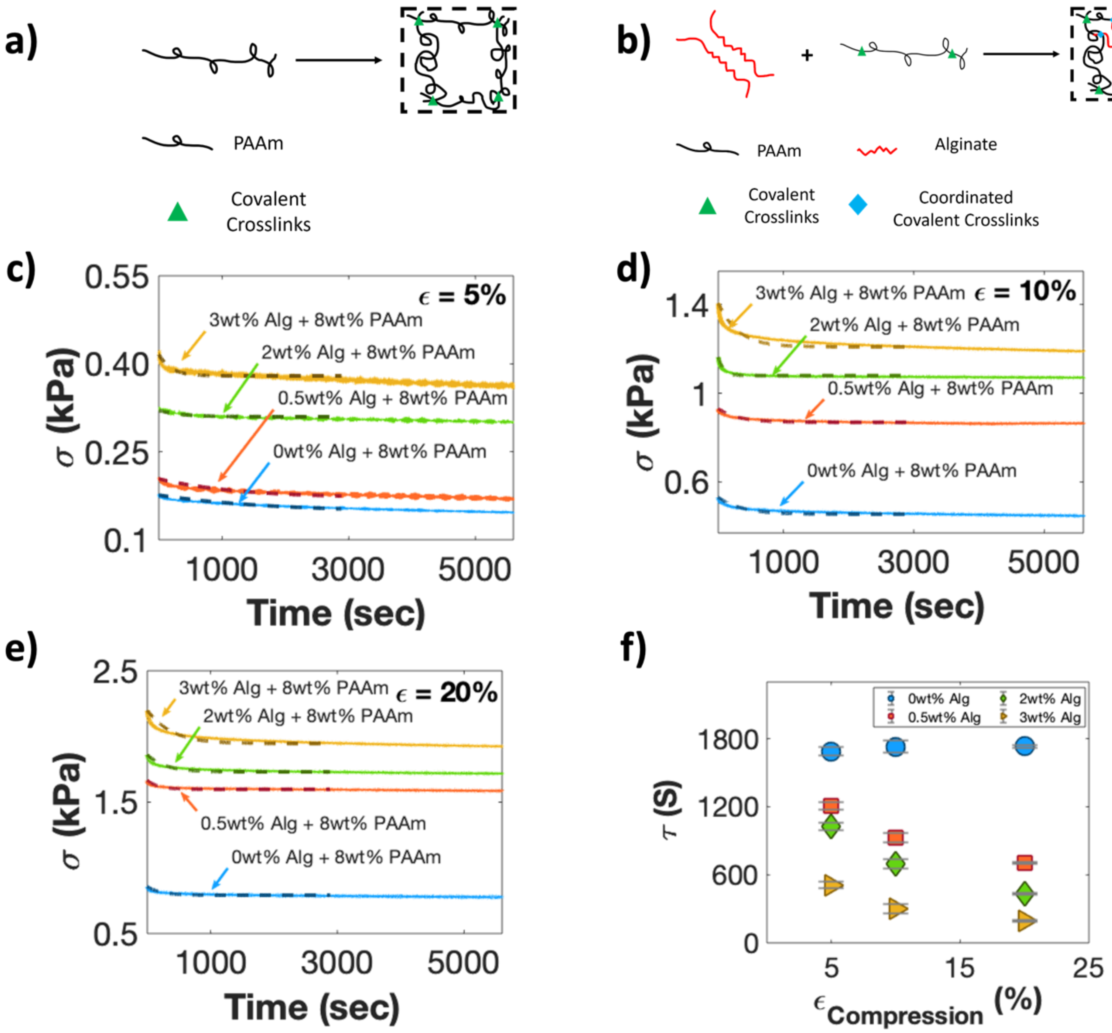

Figure 46: A hydrogel with the molecular structure seen in **(a)** is developed when AAm monomers are crosslinked to form an elastic network composed of PAAm chains. When these chains are immersed in a viscous solution of uncrosslinked alginate chains **(b)** both covalent (green triangles) and coordinated covalent bonds (blue diamonds) form within this network. To determine how the alginate viscosity will affect the viscoelastic behavior of the gel, we designed networks with varying concentration of alginate and observed the relaxation behavior under constant compressive strain. By increasing the viscosity of the alginate, and when compared to the single network PAAm gel (0wt% Alg), viscoelastic behavior is observed at ε = 5% **(c)**, ε = 10% **(d)** and ε = 20% **(e)**. Additionally, an increase in stiffness is observed due to interaction between the two polymer chains. Using the Gent model fitting results (dashed lines in c, d, and e), we plot relaxation time (τ) as a function of compressive strain which shows faster relaxation time as a function of increased alginate viscosity **(f)**.

To quantitatively study the dependence of the relaxation time on the applied strain and to illustrate the effect of solution viscosity on the gel's viscoelastic behavior, we fit the experimental data with the theoretical predictions. Using Equations 24, 25, and 26 along with the assumptions discussed in section 2.4, we can plot the stress as a function of time as predicted by the viscoelastic Gent model where the theoretical curves are shown as dashed lines in figure 46.c, d, and e. We use the fitting results and plot relaxation time (τ) as a function of applied compressive strain in figure 46.f and list the raw data in table 1. Our calculations reveal that when PAAm is dissolved in water with 0wt% alginate, its relaxation time remains constant as higher compressive strains are applied (table 2). That is no longer the case when the PAAm is dissolved in viscous alginate solution where faster relaxation times are observed at higher compression (table 2). It's interesting to note that the relaxation time is directly correlated to the alginate solution's viscosity where faster relaxation time is achieved as the concentration of the alginate is increased (figure 46.f, table 2).

Table 2: The primary relaxation time of all the tested gels obtained from theoretical fitting of the rheological model using experimentally collected data along with the standard deviation values based on 3 tested samples for each gel. As seen in **figure 46.f**, and when compared to the relaxation time of the single network PAAm gel, the addition of uncrosslinked alginate into the PAAm network results in decreasing the relaxation time under the same compressive strain. Furthermore, as the concentration of the alginate chains is increased within the PAAm network, it results in a significant reduction in the relaxation time which can be directly correlated with the increased number of coordinate covalent bonds within a specific network.

Relaxation Time (τ, sec)			
Hydrogel	**5% $\varepsilon_{Compression}$**	**10% $\varepsilon_{Compression}$**	**20% $\varepsilon_{Compression}$**
0wt% Alg + 8wt% PAAm	1688.21± 35.6	1731 ± 51.1	1734 ± 13.6
0.5wt% Alg + 8wt% PAAm	1206.61± 31.35	924 ± 40.35	705 ± 10.38
2wt% Alg + 8wt% PAAm	1029 ± 32.28	699 ± 41.24	435 ± 9.49
3wt% Alg + 8wt% PAAm	510.50 ± 33.42	303.64 ± 43.82	192 ± 8.92
2wt% Alg	435.78 ± 186.2	355.16 ± 130.3	207 ± 125.41
PAAm-Alg Double Network	475 ± 180.2	232.14 ± 179	192 ± 129.8

Because the relaxation time for the uncrosslinked alginate solution is very short (<1s) and the PAAm gel shows negligible relaxation (Fig.46.f), the observed decrease in relaxation with applied strain for crosslinked PAAm network immersed in viscous alginate solution is associated with the additional interactions between PAAm and alginate polymer.

Additionally, it is noted that the equilibrium modulus of the gel μ_1 also increases with the increased concentration of alginate polymer in the solution as shown in table 3 and the stress vs. time curves in figure 46. Apparently, the increase of the equilibrium modulus of the gel cannot be caused by the increase of the viscosity of the solution in the gel. However, such modulus increase can be attributed to the interaction between the amine groups on the PAAm and carboxyl groups on the alginate which results in the formation of dynamic coordinated covalent bonds (illustrated by blue diamonds in figure 46.b) **[54,56,72]**. By increasing the amount of alginate solution in the gel, we statistically increase the interaction between the alginate and crosslinked PAAm which results in the formation of more coordinated covalent bonds within the gel and consequently and consequently increases its equilibrium modulus and crosslink density along with the number of chains per unit volume.

The effect of the coordinated covalent bonds can be quantitatively evaluated through the equilibrium moduli reported in table 3 where the equilibrium shear modulus of the hydrogel can be estimated using Equation 27 as follows:

$$\mu_1 = N k_B T \tag{27}$$

where N is the number of chains per unit volume of the gel, k_B is the Boltzmann constant, and T is the absolute temperature. For a purely elastic hydrogel (0wt% Alg + 8wt% PAAm), μ_1 = 1.26 kPa. When 0.5wt% alginate is added, the modulus is equal to 2.22 kPa which increased the equilibrium modulus ($\Delta\mu_1$) by 0.96 kPa. The addition of 2wt% and 3wt% alginate results in a $\Delta\mu_1$ = 1.57 kPa and 1.98 kPa, respectively. The results are plotted in figure 47 and based on these calculations; we can estimate that a 1% increase in alginate concentration results in increasing the equilibrium modulus by 0.7215 kPa which can be attributed to an increase in coordinated covalent bond density within the hydrogel network.

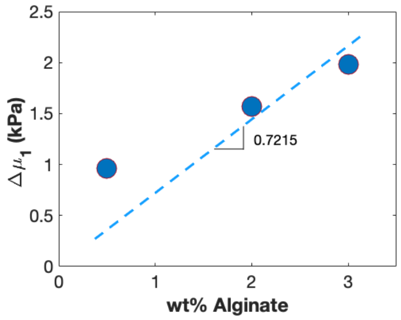

Figure 47: The Change in equilibrium modulus ($\Delta\mu_1$) as a function of weight percentage alginate

Using Equation 27 and given that $k_BT = 4.1 \times 10^{-21}$ J , we can estimate that on average, a 1% increase of alginate results in increasing the number of polymer chains by 1.75×10^{23} m^{-3}.

Table 3: The shear moduli (μ_1) and (μ_2) along with the instantaneous modulus ($\mu_1 + \mu_2$) for all the tested gels were obtained based on theoretical fitting of the rheological model using experimentally collected data. When the AAm monomers are immersed in viscous alginate solution, an increase in the values of the equilibrium modulus $\mu_1$is observed as a function of the alginate concentration which can be attributed to the formation of coordinated covalent bonds. Finally, and when compared to single network gels, the double network gel has significantly larger moduli due to the formation of ionic, covalent, and coordinated covalent bonds within its network.

Hydrogel	**μ_1 (kPa)**	**μ_2 (kPa)**	**$\mu_1 + \mu_2$ (kPa)**
0wt% Alg + 8wt% PAAm	1.26	0.13	1.39
0.5wt% Alg + 8wt% PAAm	2.22	0.18	2.40
2wt% Alg + 8wt% PAAm	2.83	0.37	3.2
3wt% Alg + 8wt% PAAm	3.24	0.55	3.79
2wt% Alg	2.94	2.40	5.34
PAAm-Alg Double Network	4.94	4.51	9.45

2.5.2. Ionically Crosslinked Alginate Gel

When the alginate is mixed with water in the presence of divalent metal ions such as Ca^{2+}, it results in the formation of egg-box structured crosslinkers **[56]**. Upon the application of constant compressive strain, the ionic bonds experience unzipping under compression for a long period of time (figure 48.a). To determine the force-dependent relaxation behavior of the gel, we measure the stress relaxation of the gel under four different compressive strains (figure 48.b). To better reveal the force-dependent relaxation dynamics observed in the experiments, we normalize the relaxation stress as:

$$\sigma_{Normalized} = \frac{\sigma(t) - \sigma_0}{\sigma_{max} - \sigma_0} \tag{28}$$

where $\sigma(t)$ is the relaxation stress at time t, σ_0 is the equilibrium stress which is obtained at t = 10,800 seconds and σ_{max} is the initial stress when relaxation starts (t = 2 seconds) which is the value of the maximum compressive stress as defined in the previous section. The normalized stress as a function of time is plotted in figure 48.c and clearly illustrates accelerated relaxation behavior at higher strain.

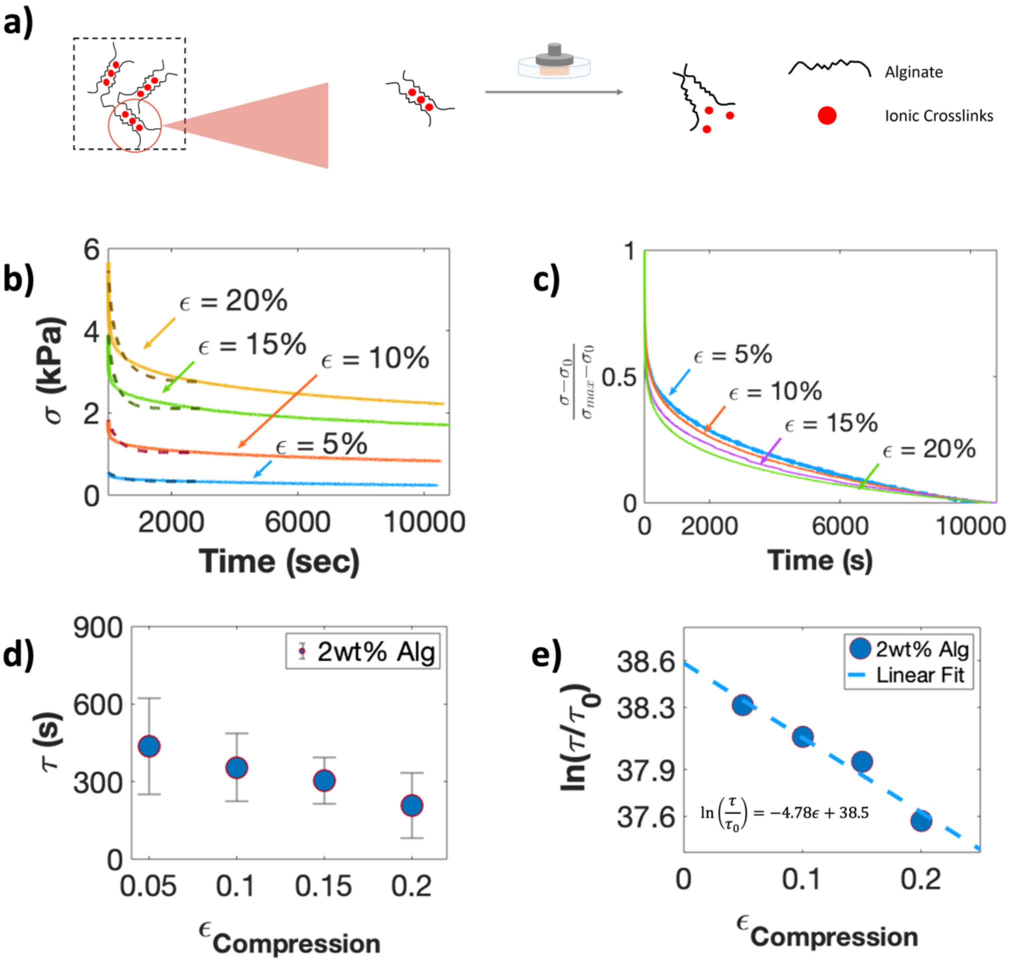

Figure 48: The stress relaxation mechanism of ionically crosslinked alginate hydrogel due to the unzipping of its ionic bonds in the presence of constant compressive strain is illustrated in **(a)**. The stress relaxation behavior was observed under 5%,10%, 15% and 20% compressive strain based on stress vs. time **(b)** where the solid line shows experimental data while the dashed line represents Gent model fitting. Normalized stress is plotted as a function of time **(c)** where strong force-dependent viscoelastic behavior is observed. The Gent model fitting results were used to plot relaxation time (τ) and ln(τ/τ_0) as a function of applied compressive strain in **(d)** and **(e)** respectively where τ_0 is the inverse of average atomic frequency and is equal to 10^{-14} seconds.

As stated in section 2.5.1, we can plot the stress as a function of time as predicted by the Gent model where the theoretical curves are shown as dashed lines in figure 48.b. We also obtained the relaxation time (τ) (table 2) along with the values of μ_1 and μ_2 (table 3) and according to fitting results of the rheological model, the relaxation time decreases with increased compressive strain (figure 48.d, table 2). At the lowest compressive strain of 5%, the gel's relaxation time was 435 seconds whereas at the highest compressive strain of 20%, the gel undergoes relaxation within 207 seconds which is 52.4% faster.

We next correlate the measured stress relaxation kinetics to the ionic debonding process. Without the application of an external force, the time needed for the ionic debonding can be given by:

$$\tau = \frac{1}{\nu} \exp(\frac{E_a}{k_B T}) , \tag{29}$$

where ν is the average atomic frequency, the typical value of which is 10^{14} Hz, E_a is the dissociation energy, k_B is Boltzmann's constant (1.38×10^{-23} $\mathrm{JK^{-1}}$) and T (300 K) is the absolute temperature.

We assume that the stress relaxation measured in the alginate hydrogel stems from the ionic debonding. When a polymer chain is subject to force f, the ionic debonding time can be modified as:

$$\tau = \frac{1}{\nu} \exp\left(\frac{E_a}{k_B T}\right) \exp\left(\frac{f\,\Delta_a}{k_B T}\right) , \tag{30}$$

where Δ_a is the activation length. By re-arranging Equation 30, we obtain the following linear equation:

$$\ln\left(\frac{\tau}{\tau_0}\right) = \frac{E_a}{k_B T} - \Psi\varepsilon \tag{31}$$

where $\tau_0 = 1/\nu = 10^{-14}$ sec and $\Psi = \frac{K\,\Delta_a}{k_B T}$, with the assumption $f = K\varepsilon$.

In figure 48.e, we plot $\ln\left(\frac{\tau}{\tau_0}\right)$ as a function of the applied compressive strain where linear fitting is used to determine the values of $\frac{E_a}{k_B T} = 38.5$ and $\Psi = 4.78$ based on the y-intercept and slope. We can calculate the dissociation energy E_a to be 95.9 $\mathrm{kJmol^{-1}}$, which is consistent with previous studies **[56,73,74]**.

We can link the force *f* that one chain experiences, the Young's modulus and the applied strain based on eight-chain model as **[75]**:

$$f = El_0^2 \frac{\sqrt{3}}{4} \varepsilon \quad \textbf{(32)}$$

where $E = 0.013\ MPa$ and is the Young's modulus, ε is the applied compressive strain and l_0 is the mesh size of the polymer network **[76]**. Based on the definition of $\Psi,$ we have:

$$\Psi = \frac{\sqrt{3}El_0^2\Delta_a}{4k_BT} \quad \textbf{(33)}$$

Built on the previous studies, we put the mesh size of the alginate gel to be 50 nm, and by using Equation 33, we find that the activation length Δ_a= 1 nm, and this is comparable to the size of a G-Block which forms an ionic bond with the Ca^{2+} in the alginate gel **[56]**.

2.5.3. Crosslinked PAAm-alginate Double Network Hydrogels

Double network gels have been recently intensively explored to achieve superior mechanical properties. A representative double network gel is formed by combing these two polymers (figure.49.a) with covalent (green triangles) and ionic (red circles) bonds in addition to the formation of coordinated covalent bonds (blue diamonds) because of chain interaction as discussed in section 2.5.1. Under three different compressive strains (figure 49.b), the double network hydrogel behaves similarly to the single network alginate gel with noticeable change in relaxation behavior at higher strain as shown figure 49.c where normalized stress is plotted as function of time. The results indicate that the stress relaxation in a double network gel is also associated with the unzipping of ionic bonds within the gel's network.

Like what we did previously, fitting data of the rheological model (dashed lines in figure 49.b) were used to determine the relaxation time as a function of the applied strain (figure 49.d, table 2) and the results confirm the presence of strong force-dependent behavior due to the alginate ionic bonds that exists within the hydrogel's double network.

Using Equation 31 and the concept of microscopic force sensitivity explained in section 2.5.2, the value of Ψ for the double network hydrogel was found to be equal to 5.44 (figure 49.e) which is 1.13 times larger than the value for single network alginate. Such difference is mainly because of the different environment and chain topology in ionically crosslinked alginate gel and the double network gel. Although the value of Ψ is different for the two gels, the dissociation energy E_a value remains unchanged and is also equal to 95.9 $kJmol^{-1}$ for the double network gel. This is expected since the source of energy comes from the ionic debonding of the alginate chains which are present in equal amounts in both hydrogels.

Furthermore, and based on the results obtained from the Gent model, we find that the double network equilibrium modulus (μ_1) was equal to 4.94 kPa which is 17.6% higher than the addition of the single network moduli (table 3) and this again can be explained by the formation of the coordinated covalent bonds between the alginate and PAAm polymer chain as described previously.

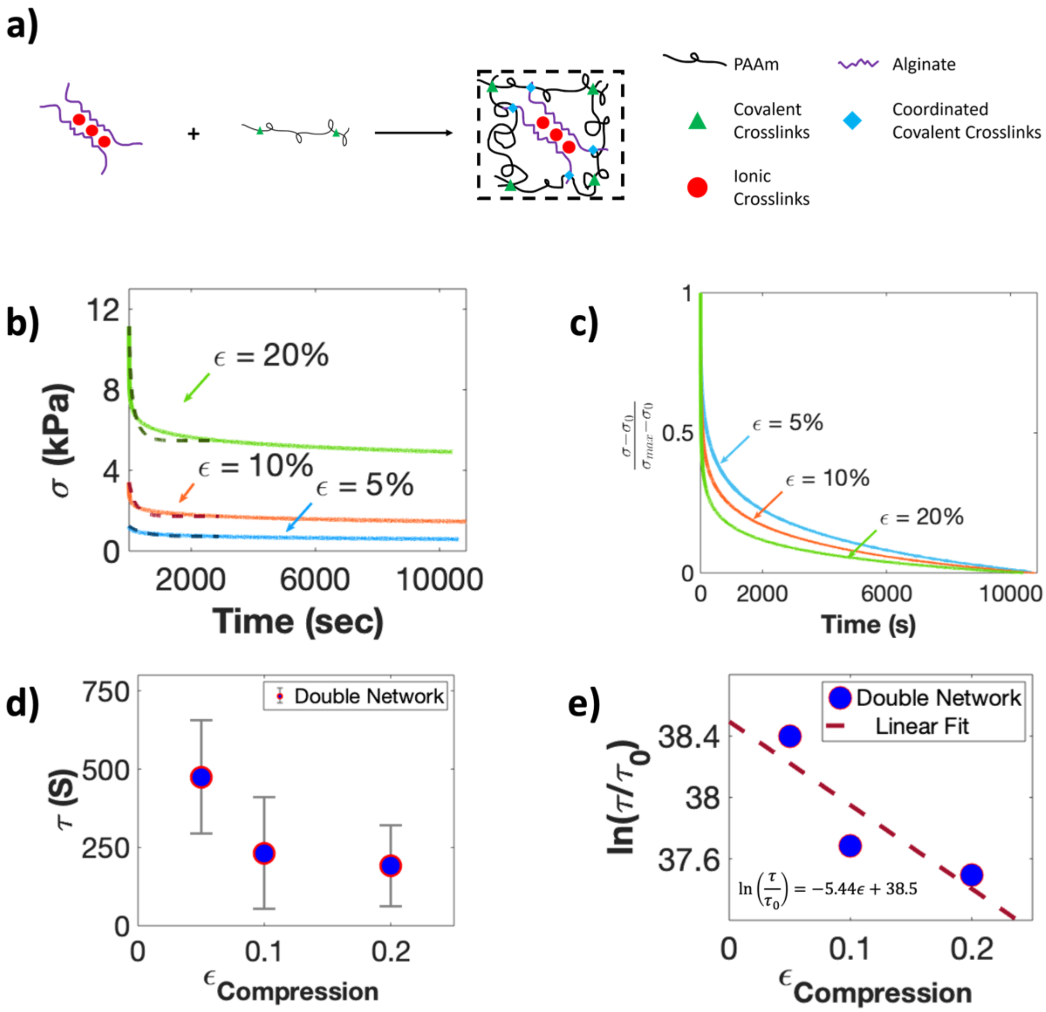

Figure 49: The two single networks were combined to create a double network hydrogel that has ionic bonds along with the two types of covalent bonds previously discussed within its network **(a)**. The stress relaxation behavior of the double network hydrogel was observed under 5%,10% and 20% compressive strain based on stress vs. time **(b)** where a significant increase in the stiffness was observed due to the formation multiple bonds within the gel. At higher compressive strains, we observe strong force-dependent viscoelastic behavior when normalized stress is plotted as function of time **(c)**. The Gent model fitting results were used to plot relaxation time (τ) and ln(τ/τ_0) as a function of applied compressive strain in **(d)** and **(e)** respectively where τ_0 is the inverse of average atomic frequency and is equal to 10^{-14} seconds.

2.6. Chapter Conclusions

Hydrogels have been used in many applications within the biomedical field, active devices, and soft robots, however, many of their potential applications can be unlocked by learning how to tune their properties to meet specific requirements for unique applications.

With this aspiration in mind, we have conducted a systematic investigation on how to tailor the viscoelastic behavior of covalently crosslinked PAAm networks by increasing the viscosity of the aqueous solution in which the polymer network is immersed in. Our results have shown that when AAm monomers are dissolved in water, the PAAm hydrogel behaves elastically under compressive strain and experiences minimal stress relaxation. However, when the same amount of AAm monomers were dissolved in viscous alginate solution, the resulting hydrogels experienced increased viscoelastic behavior with increased alginate concentration. Through theoretical fitting of the rheological model, we reported the relaxation time and how it changes as a function of alginate concentration and applied compressive strain.

Although previous studies have assumed that the time scale associated with viscoelasticity is constant, our detailed study of the stress relaxation behavior of ionically crosslinked alginate networks and double network hydrogels have proven otherwise. Through our experimental data and Gent model fitting, we were able to quantitatively correlate the macroscopically viscoelastic behavior of the hydrogel by confirming faster relaxation time at higher compressive strains with the microscopic ionic debonding process while using reasonable activation length Δ_a and dissociation energy E_a.

Finally, and by reporting the moduli of the six different types of hydrogels investigated in this study, we provide quantitative evidence of a widely accepted theoretical concept within the community and confirm the existence of coordinated covalent bonds that form whenever amine groups on the PAAm chains interact with the carboxyl groups on the alginate chains.

Chapter 2, in full, is coauthored and has been submitted for publication of the material as it may appear in Mechanics of Time-dependent Materials, 2023. Qari, Nada; Song, Zhaoqiang; Hosseini-toudeshki, Hamed; Li, Chenghai; Cai, Shengqiang. The dissertation author was the primary investigator of this paper.

Chapter 3

Stress-assisted Erosion of Poly (Glycerol-co-Sebacate) Acrylate Elastomer

3.1. Introduction & Background

Today, global consumption of plastics is greater than 200 million tons with an expected annual growth of 5% [77]. Yet, commonly used oil-based plastics such polystyrene (PS) and high-density polyethylene (HDPE) do not undergo natural degradation which has significantly harmful effects on the environment. In fact, out of the 35.4 million tons of plastic that are generated each year in the United States, 26.8 million tons end up in landfills [78]. While the overall number of recycled plastics remains relatively small with an 8.4% current recycling rate which is equivalent to 3 million tons per year [78]. Due to these facts, and in recent decades, the scientific community has rushed to the development of degradable polymers, which can undergo degradation in response to a trigger such as humidity, elevated temperatures, and light [79,80]. Since their development, degradable polymers have been used in surgery, drug delivery, tissue engineering and the development of environmentally sustainable products [81-85]. With the accelerated ongoing research efforts, degradable polymers are expected to rapidly replace nondegradable ones. In recent years, the sales of degradable polymers exceeded $7 billion, accounting for almost 88% of the total biomaterial market [86]. Future outlooks predict that the biocompatible materials market will reach $11.9 billion suggesting a huge market for degradable polymers in the coming decades [85,86].

Although polymer degradation is predominantly a chemical process, it is also accompanied with erosion where diffusion, dissolving and other physical processes are involved. Degradation usually refers to the breakdown of certain bonds in the polymer's backbone. Erosion designates the loss of material from the bulk of the polymer in the form of oligomers and monomers [87]. When it comes to degradation mechanics, hydrolysis is the most common path taken by degradable polymers. After the initial attack by water, there are a series of events, including a decrease in the molecular weight and a gradual loss of mechanical properties [88]. After that, erosion, which is a predominantly physical process takes place and is typically characterized by the mass loss of a polymer matrix [89]. Polymer erosion can be divided into two types: bulk and surface erosion. When a polymer experiences bulk erosion, material is lost from the entire polymer volume. In this case, the erosion rate depends on the total amount of material and decreases as the material is depleted [90]. On the other hand, when a polymer exhibits surface erosion, the material is lost from the polymer exterior surface. In this case, the erosion rate is directly proportional to the external surface area and the rate remains mostly constant until the polymer is completely eroded [90]. The kinetics of how a polymer degrades and erodes can significantly influence its performance along with the type of applications that it can be used for.

In addition to their degradation, the interaction between polymer chains with water can also lead to premature failure and crack growth. And due to the type of applications that degradable polymers are used in, they are often subject to various forces during degradation. However, and according to our knowledge, many of the previous studies have ignored the effect of stress on the degradation process where most studied have been conducted using free standing samples. Therefore, in this study, we aim to understand the influence of stress on polymer degradation from two perspectives. First, the effect of external stress and strain on the degradation process of a polymer without obvious defects. Second, the effect of stress and strain on the degradation of a polymer sample with a pre-crack. In fact, recent studies have shown that as polymers start to degrade, cracks and voids will begin to form [81,87]. We believe that in the presence of an external load, the applied stress will be concentrated at the tip of the crack and since the polymer is undergoing degradation due to its interaction with water, the concentrated stress will lead to crack growth and eventual failure of the material [81]. This type of phenomenon has been observed in many materials including metals, natural rubber, and non-degradable polymers and is known as stress corrosion cracking (SCC) [81,91-94].

In the case of degradable polymers such as poly (glycerol sebacate) (PGS), water from the environment reacts with the ester bond on the polymer backbone resulting in the formation of carboxyl and hydroxyl groups [80]. These reactions break the chain and degrade the polymer. As the polymer degrades, its mechanical properties or size may change and so will its performance within a specific application, especially in the presence of an external load. In fact, recent studies have shown that the speed of the hydrolytic crack depends on relative humidity, pH, and applied load [80,81,95]. In recent years, the acrylated derivative of PGS known as poly (glycerol sebacate) acrylate (PGSA) has sparked a lot of interest within the research community. When compared to PGS, PGSA is a strong, stretchable, and photocurable elastomer that can be easily crosslinked in the presence of ultraviolet radiation [81,96]. This makes it possible to process solid PGSA structures using bioprinting along with various types of light-based lithography. Because of its practical processing techniques, PGSA has been used to develop degradable stents and porous capsules for drug delivery [96,97].

In this work, we conduct a detailed investigation on PGSA with the aspiration of understanding its hydrolytic degradation kinetics and how the degradation rate of a sample without obvious defects changes with the applied strain. Furthermore, to study the coupled effect of degradation and external mechanical loading, we systematically studied the SCC phenomena using PGSA samples with pre-cut and two different crosslink densities.

By studying the degradation of PGSA at high pH and in the absence of external stress, we confirmed that the polymer undergoes surface erosion with an observable erosion front. By investigating the degradation kinetics of PGSA at neutral pH and under varying stresses and strains, we observed that the degradation rate is accelerated when stresses and strains are applied on the degrading sample. Finally, we studied the coupled effects of degradation and mechanical loading on PGSA through our study of the SCC phenomena. In doing so, our results have revealed that crack growth outruns PGSA's surface erosion rate which is consistent with recent studies that have reported similar behavior in other types of degradable polymers [81].

3.2. Materials Synthesis

The synthesis of the PGS and PGSA polymers were prepared by following pervious articles [96-98]. Briefly, the pre-polymer PGS was prepared through the polycondensation reaction of an equimolar ratio of glycerol (Sigma-Aldrich G5516) and sebacic acid (Sigma-Aldrich 283258) at the temperature of 120°C, and pressure of 15 mbar for 48 hours (figure 50.a). Next, PGS (30 g) was reacted with acryloyl chloride (2.75 mL, Sigma-Aldrich A24109) (figure 50.b) to convert 12.5% of OH groups to acrylate groups (figure 50.c). After 24 hours, the acrylation reaction is complete and the HCl is filtered out of the product in the form of white salt. Upon filtration, the final PGSA polymer is collected in liquid form and stored in brown vials at -4°C for future usage.

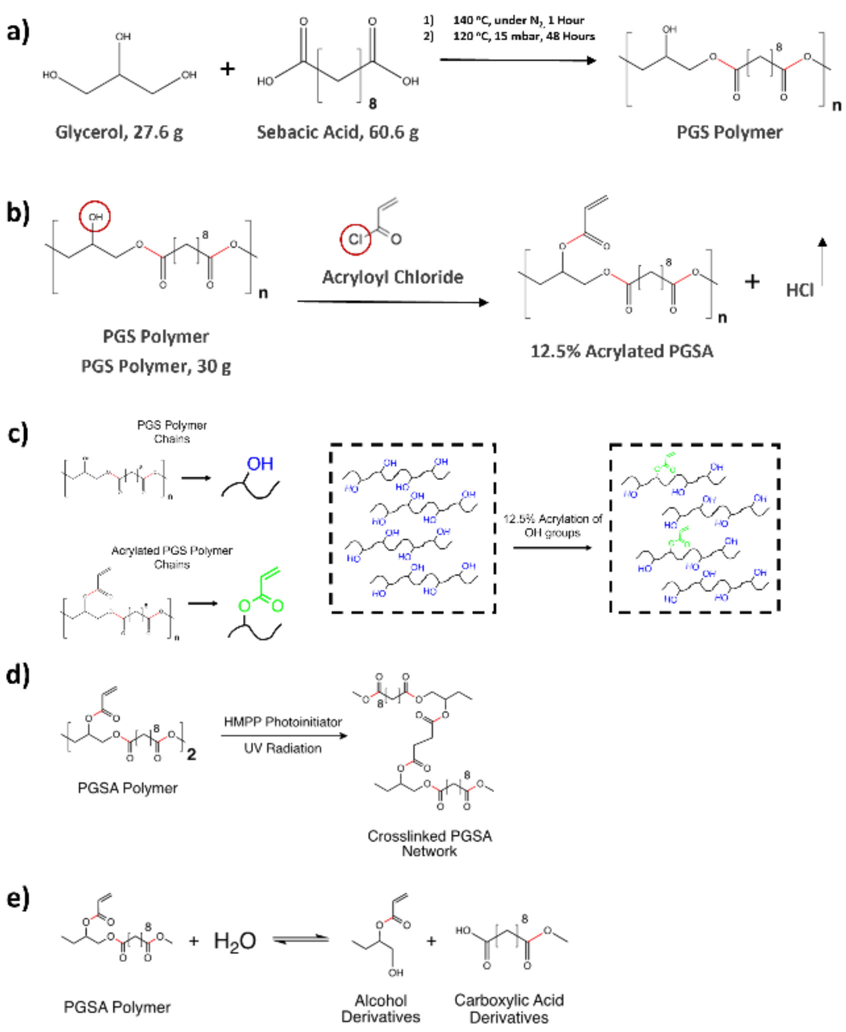

Figure 50: The first step of synthesizing the PGSA polymer involves the condensation **(a)** of glycerol and sebacic acid at 120°C and 15 mbar for 48 hours which results in the formation of the PGS pre-polymer. The PGS is reacted with acryloyl chloride **(b)** in an acid-base reaction to generate the PGSA polymer where 12.5% of the OH groups are converted to acrylate groups **(c)** and the HCl is filtered out of the reaction product in the form of white salt. The PGSA polymer is crosslinked through the acrylate bond via free radical polymerization in the presence of UV radiation **(d)**. In an aqueous solution, **(e)** The PGSA polymer undergoes hydrolytic degradation through its ester bond (highlighted in red) and breaks down to its alcohol and carboxylic acid derivatives. Note that the ester bonds undergo hydrolytic degradation and are highlighted in red in figures a through e.

To prepare solid samples, PGSA (5.15 g) is mixed with 2-Hydroxy-2-methylpropiophenone (HMPP, 0.105 g, Sigma-Aldrich 405655), a photo-initiator, and are crosslinked under ultraviolet radiation (UV) via free radical polymerization through the acrylate groups (figure 50.d).

3.3. Results & Discussion

3.3.1. The Degradation of PGSA

3.3.1.1. Demonstration of surface erosoin of PGSA in a high pH aqueoue enviorment

Like PGS, the ester bonds present in PGSA undergo hydrolytic degradation in the presence of water which results in breaking down the polymer chain into its alcohol and carboxylic acid derivatives (figure 50.e). To determine the degradation mechanism of PGSA and whether it undergoes surface or bulk erosion, we investigate the *in-situ* degradation of PGSA in a stress-free high pH environment. This was achieved by preparing a cylindrical shaped sample with the dimensions shown in figure 51.a where each side of the sample was exposed to 10 minutes of UV light to complete the crosslinking reaction. Additionally, the sample was dyed red using Rhodamine B (0.0035 g, Acros-Organics 25GRR) to allow clear observation of the erosion process.

To accelerate the degradation process so that it is observable within a few hours, the crosslinked sample was fully immersed in a 0.5 (M) NaOH solution where the pH was equal to 13.69. This setup was placed under an optical microscope and the degradation reaction was observed from a top-down view (figure 51.a). Throughout the experiment, and using the microscope's camera, we capture an image every 10 minutes until the degradation reaction was complete with no sample left in the reaction flask.

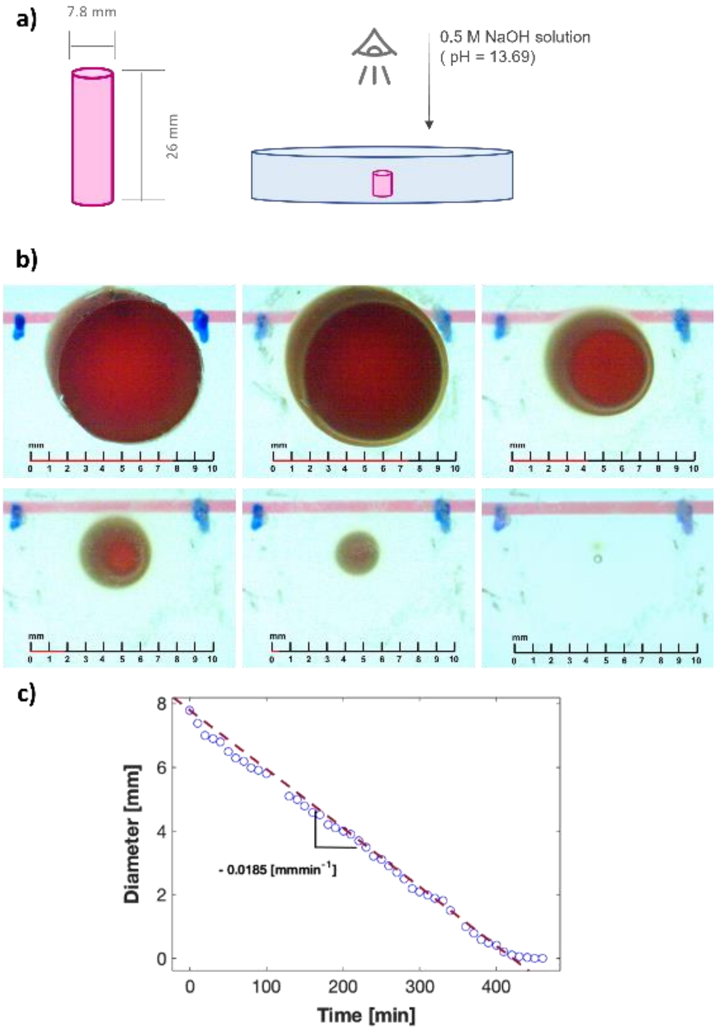

Figure 51: A cylindrical PGSA sample with the dimensions shown in **(a)** was dyed using Rhodamine B and fully immersed in a 0.5 M NaOH solution (pH = 13.69) where the surface erosion was observed in real time using an optical microscope with a top-down view. Images were captured every 10 minutes for 7.6 hours where the main stages of degradation are highlighted in **(b)**. The experimental images were used to measure the cylinder's diameter and how it changed as a function of time **(c)** where linear fitting illustrated by the dashed line was used to determine the degradation rate of PGSA at pH 13.69 which was equal to 0.0185 $mmmin^{-1}$.

As seen from the images in figure 51.b, at time = 0 minutes, the diameter is equal to 7.8 mm. Within the first 10 minutes, the diameter reduces to 7.4 mm in addition to the appearance of a yellow ring around the sample's diameter which is associated with the diffusion of the dyes from the sample to the external solution. The reduction of the sample is illustrated by the images captured at time = 190, 320 and 400 minutes. Finally, after 7.6 hours, the sample was fully degraded, and no more mass was left in the reaction flask.

The data collected throughout the experiment was used to plot the diameter as a function of time (figure 51.c) and by measuring the slope through linear fitting, we found that the degradation speed of PGSA in such conditions was equal to 0.0185 $\mathrm{mmmin^{-1}}$. Furthermore, our results confirm that surface erosion is the dominant degradation mechanism for the PGSA polymer.

3.3.1.2. Demonstartion of the effec of mehancial stress on the hydrolytic rate of PGSA

To directly observe the effect of stress on the hydrolysis of PGSA, we designed a T-shaped PGSA sample with the dimensions illustrated in figure 52.a. This sample was placed on a linear actuator which was used to apply a 5% elongation on the entire sample where the applied elongation was held constant for the total duration of the experiment (7 days) (figure 52.b). This geometry was selected so that the stretched sample can experience two different stresses under the same force due to the difference of cross-sectional area. The wide region (20 mm x 0.93 mm) would experience lower stress since it has a larger cross-sectional area whereas the narrow region (10 mm x 0.93 mm) would experience higher stress.

To study the stress assisted hydrolysis, the stretched sample was fully immersed in a water tank (pH = 7) and the thickness of both the wide and narrow regions were measured daily. As a control test, a PGSA sample was placed in a water medium with no applied stress for 10 days where the thickness was measured every 2 days. The thickness data collected throughout the experiment were plotted as a function of time where we can clearly observe the effect of stress on the degradation rate (figure 52.c).

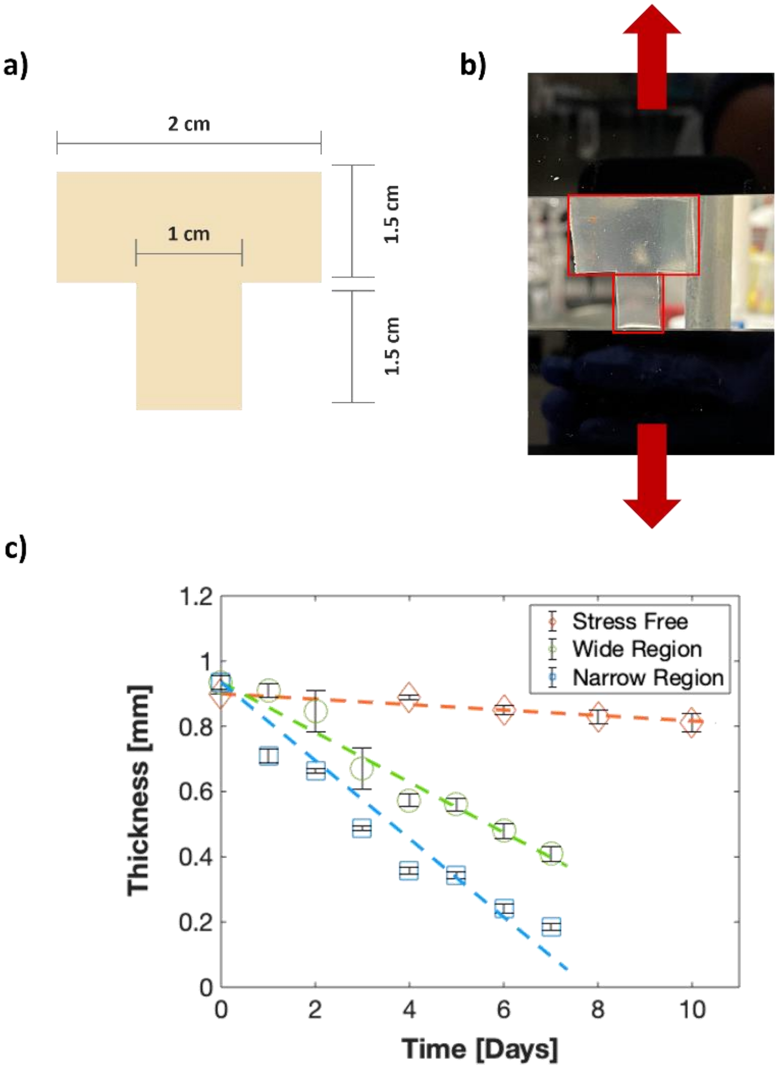

Figure 52: To determine the effect of stress on the surface erosion of PGSA, we designed a T-shaped PGSA sample with the dimensions shown in **(a)** and used a linear actuator to stretch the sample by 5% where the stretch was held constant **(b)**. The stretched sample was placed in a water tank (pH = 7) while monitoring the thickness every day for 1 week for both the wide and narrow regions of the T-shaped structure. Upon completion, the collected thickness values were plotted as a function of time **(c)**. Our experimental results along with liner fitting shown as dashed lines confirm that the narrow region degrades faster than the wide region. Furthermore, and when compared to an unstretched sample that is exposed to the same pH conditions, the stretched PGSA degrades at a faster rate.

At neutral pH and with no applied stress, the PGSA degradation rate is approximately 0.0083 mmday^{-1}. However, when the sample is stretched under the same pH conditions, the wide region experiences a 0.076 mmday^{-1} degradation rate (89% faster than the control test). Whereas the narrow region degrades at a rate of 0.119 mmday^{-1} which is 93% faster than the control test. Based on the results reported in figure 52, we were able to show that there is a direct relationship between the degradation rate of PGSA and the applied stress where our results confirm that with higher stress, the PGSA polymer degrades faster.

3.3.1.3. Quantitative effect of applied strain on the surface erosion rate of PGSA

To study the effect of applied strain systematically and more quantitatively on the hydrolysis-induced surface erosion of PGSA, we conducted further experiments using a homogeneous sample with the dimensions shown in figure 53.a. A linear actuator was used to stretch the sample where the applied strain was held constant for 7 days (figure 53.b). Likewise, the stretched sample was fully immersed in a water tank with pH = 7 and the thickness was measured daily.

This setup was used to investigate the effect of 6 differently applied strains starting with 5% followed by 10%, 15%, 20%, 25% and 30% respectively. As a reference state, a PGSA sample was placed in a water medium with no applied strain for 10 days where the thickness was measured every two days. The data collected throughout the experiment were plotted as a function of time where a clear dependence between the applied strain and degradation rate can be observed (figure 53.c).

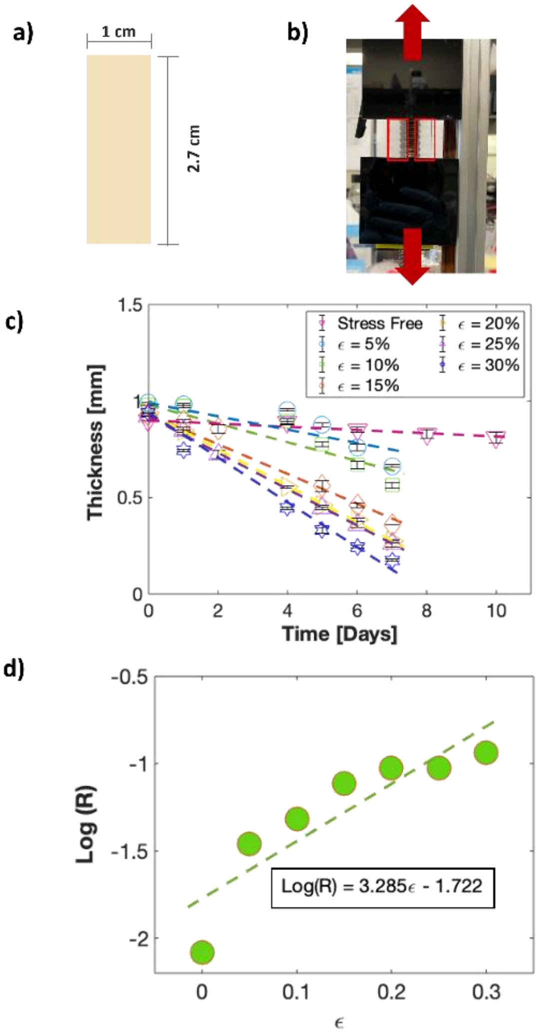

Figure 53: To determine the effect of strain on surface erosion, we designed a tensile shaped PGSA sample with the dimensions shown in **(a)** and used a linear actuator to apply 6 different strains starting from 5% followed by 10%, 15% 20%, 25% and 30% respectively using the same type of sample for each test **(b)**. The stretched samples were placed in a water tank (pH = 7) where the thickness was monitored every day for 1 week. Upon completion, the thicknesses were plotted as a function of time where we observe an increase in degradation rate at higher strain. Linear fitting illustrated by dashed lines was used to determine the different degradation rate (*R*) values in mmdays^{-1} **(c)**. The logarithmic values of (*R*) were determined and plotted as a function of the applied strain in **(d)** where liner fitting indicated by the dashed line was used to calculate the slop and y-intercept highlighted by the boxed equation.

At neutral pH and with no applied strain, the PGSA sample degrades at a slow rate of 0.0083 mmday^{-1}. At 5% strain, the degradation rate is increased to 0.034 mmday^{-1}.

The application of 10% strain on the sample further increases the degradation rate to 0.048 mmday^{-1}. When a 15% strain is applied on the sample, the degradation rate goes up to 0.076 mmday^{-1}. At 20% and 25% strain, the degradation rates are approximately 0.0946 and 0.0941 mmday^{-1} respectively. However, when a 30% strain is applied on the sample, the degradation rate increases to 0.116 mmday^{-1}. Based on that, our results confirm the relationship between applied strain and degradation rate (*R*) where the rate is dramatically increased at higher strain. To further illustrate this effect, figure 53.d plots the logarithmic values of the degradation rate (*R*) as a function of the applied strain.

3.3.2. Stress Corrosion Cracking

Previous studies have shown that if pre-cracks exist in degradable polymers, the stress corrosion cracking may outrun the degradation process because the stress can be highly concentrated near the crack tip. So, next, we study the stress corrosion cracking process of PGSA.

3.3.2.1. Effect of crosslink density on the mechanical behavior of PGSA

As mentioned previously and when compared to the PGS elastomer, one advantage of using acrylated PGS is its photocurable properties. The crosslinking mechanism mentioned in section 3.2 (figure 50.d) allows us to control the crosslink density simply by adjusting the polymer's exposure time to UV radiation. And by changing the crosslink density, we can alter the mechanical properties of the PGSA polymer.

Through uniaxial tensile testing at 0.25% s^{-1} strain rate, and by using a simple rectangular geometry (10 mm x 60mm x 1 mm), our results have shown that when the PGSA polymer is exposed to 15 seconds of UV radiation, this results in the formation of a solid film with low crosslink density where the soft sample can be stretched to 144.3% strain before fracture and has an ultimate strength of 63.3 kPa. However, when the PGSA polymer is exposed to 5 minutes of UV radiation, a solid film with high crosslink density is formed where the stiff sample is only stretched to 40.34% strain before failure, yet its ultimate strength is increased to 105.5 kPa (figure 54.a).

To determine the fracture toughness of PGSA and how it changes as function of crosslink density, we conducted tensile testing at 0.25% s^{-1} strain rate using pure shear geometry (50 mm x 10 mm x 1 mm). When the samples are un-notched (figure 54.b), calculating the area under the stress-strain curve allows us to determine the work of rupture *W* in Jm^{-3}. By doing so, we find that high crosslink density PGSA has a $W = 6.67 \times 10^3$ Jm^{-3} while low crosslink density PGSA has a *W* that is equal to 2.93×10^3 Jm^{-3}.

By conducting the same type of tensile testing using notched samples with pure shear geometry, we can determine the critical strain $\varepsilon_{critical}$ and how it changes as a function of crosslink density. As seen from figure 54.c, high crosslink density PGSA fractures at $\varepsilon_{critical} =$ 15.34% while low crosslink density PGSA fractures at $\varepsilon_{critical} = 22.23\%$. By determining the values of both the work of rupture and the critical strain, we can determine the fracture toughness Γ in Jm^{-2} for each type of PGSA using Equation 34:

$$\Gamma = HW(\varepsilon_{critical}) \tag{34}$$

where *H* is the height of the sample, and the value of *W* was calculated by taking the area under the stress-strain curve of the un-notched sample from zero strain to the critical strain where the pre-cut sample ruptures. By completing these calculations, we find that the fracture toughness values are equal to 19.56 Jm^{-2} and 14.78 Jm^{-2} for the high and low crosslink density PGSA, respectively.

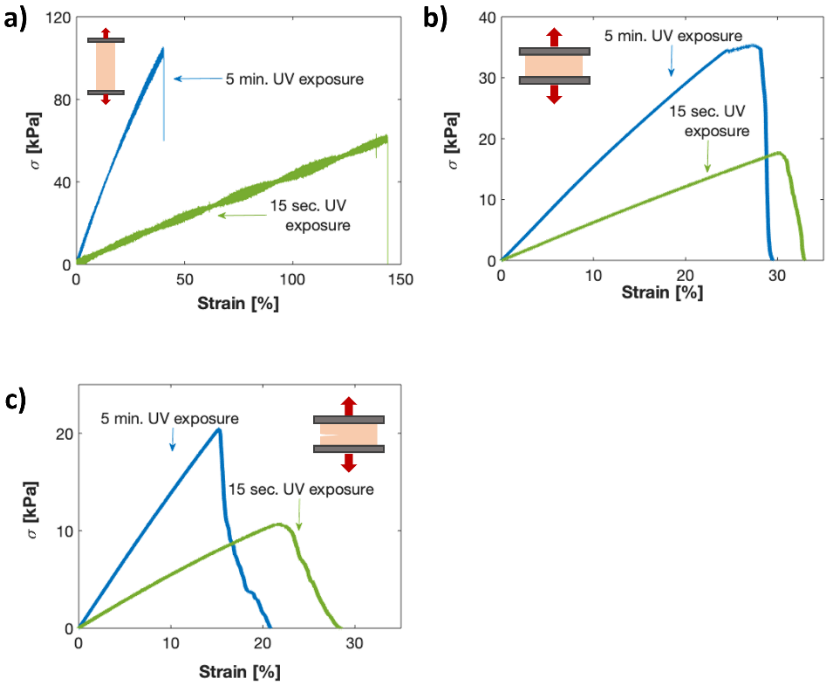

Figure 54: Tensile testing was completed on PGSA samples with low and high crosslink density using the Instron's 10 N load cell at a strain rate of 0.25% s^{-1}. **(a)** By exposing a rectangular-shaped sample to 5 minutes of UV, we create a stiff sample with 40.34% failure strain. However, when another sample is exposed to 15 seconds of UV, it becomes soft and fails at 144.3% strain. **(b)** To calculate the work of rupture, we test both types of PGSA samples with un-notched pure shear geometry and use the plot to determine the area under the curve. **(c)** To determine the value of the critical strain along with the range of energy release rate values that can be used in the stress corrosion cracking experiment, we test both types of PGSA samples with notched pure shear geometry.

By calculating the work of rupture and fracture toughness of both types of PGSA samples along with the results shown in figure 54, we confirm that by simply changing the UV exposure time, we can tune the crosslink density of the polymer along with its mechanical properties. Using this methodology, we can create PGSA samples using the same polymer chains that have quite different mechanical properties. And because of that, we believe that the two samples should respond differently when exposed to similar experimental conditions. Therefore, and to confirm our hypothesis, we investigate the phenomena of SCC on both samples and compare the results in the remaining sections.

3.3.2.2. Experimental setup for the stress corrosion cracking experiment

To study the SCC phenomenon in PGSA, and following the pervious article [81], we design a notched sample with the dimensions shown in figure 55.a where 1 cm from both ends is attached to an acrylate plate so that only 1 cm of the sample's width is exposed to testing conditions.

The bottom acrylate plate is attached to an in-house designed water tank and the top plate is attached to the Instron's 10 N load cell (figure 55.b). Once in place, the tank is filled with DI water (pH = 7) fully immersing the sample in solution. After that, 10 different strain values that range from 14% to 3% for the high crosslink density PGSA are applied at 0.25% s^{-1} ($\varepsilon_{applied} < \varepsilon_{critical}$) and held constant for 3 hours or until crack propagation is complete (figure 55.c). The same type of testing was done using low crosslink density PGSA where the 10 different strain values ranged from 21.5% to 16%.

To accurately measure the crack growth throughout the experiment, we use a high-resolution camera where images were captured periodically from time equals zero until the end of the experiment. The captured images were used to calculate the crack growth as a function of time which is then used to determine how the crack growth rate changes as a function of the applied strain.

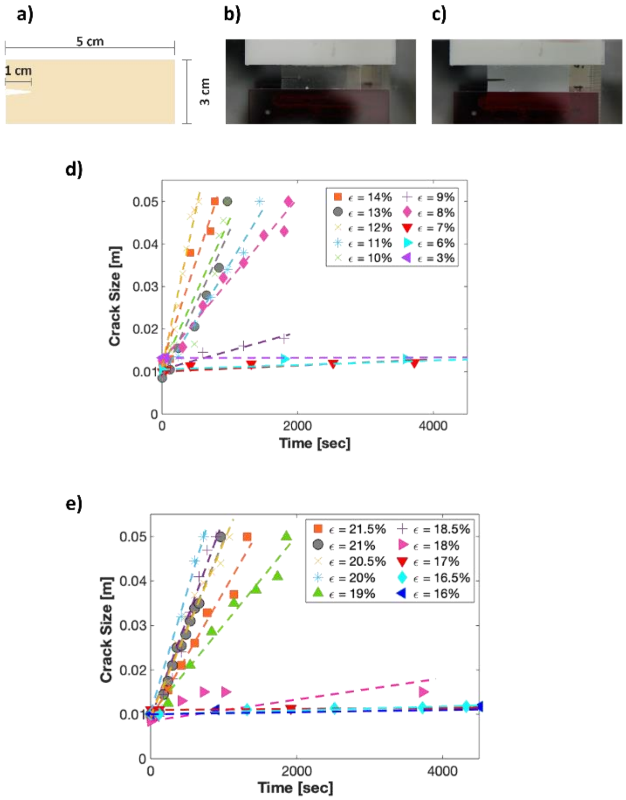

Figure 55: To study the phenomena of stress corrosion cracking in PGSA, we designed a notched pure shear testing sample based on the dimensions shown in **(a)**. The sample was attached to the Instron machine using an in-house designed water tank setup **(b)**. The 10 N load cell was used to apply a specified strain which was held constant until fracture while the sample was fully immersed in DI water with pH = 7 **(c)**. Throughout each experiment, a camera setup was used to consistently capture images to determine the crack size growth rate as a function of time. The PGSA samples with high crosslink density (5 min. UV exposure) were tested under 10 different strains starting with 14% to 3% and the measured crack size was plotted as a function of time **(d)**. The same type of testing was conducted using PGSA samples with low crosslink density (15 sec. UV exposure) where the applied strains were adjusted based on the pre-determined critical strain starting with 21.5% to 16% and the measured crack size was plotted as a function of time **(e)**. Note that liner fitting illustrated by the dashed lines was used to determine the crack growth rate for each of the applied strains in both cases discussed in **d** and **e**.

3.3.2.3. Time-dependent crack growth in the sample with constant strain

In figure 55.d we plot crack size as a function of time based on the data collected from all 10 experiments using high crosslink density PGSA. We observe two regions of crack growth rates: high and low rates that are dependent on the applied strain. When the $\varepsilon_{applied}$ values ranged from 14% to 8%, we observe rapid crack growth and full crack propagation within 2000 seconds or less. However, when the strain range is between 7% and 3%, we observe minimal crack growth with negligible propagation even after 3 hours of constant strain application.

In the high crack growth rate region (figure 55.d), the crack velocity ranged from $4.91\text{x}10^{-5}$ ms^{-1} to $1.92\text{x}10^{-5}$ ms^{-1} for the 14% and 8% applied strain respectively (table 4). On the other hand, in the low crack growth rate region, the velocity was as low as $4.67\text{x}10^{-7}$ ms^{-1} and $3.33\text{x}10^{-8}$ ms^{-1} for the 7% and 3% applied strains respectively (table 4).

Table 4: Applied stain values, energy release rate and crack velocity of high crosslink density PGSA exposed to 5 minutes of UV radiation along with the standard deviation values.

High Crosslink Density PGSA – 5 Minutes UV Exposure			
Applied Strain [%]	**Energy Release Rate [G, Jm^{-2}]**	**Crack Velocity [V, ms^{-1}]**	**STD [ms^{-1}]**
14%	16.55	$4.91\text{x}10^{-5}$	0.113
13%	14.38	$3.87\text{x}10^{-5}$	0.098
12%	12.31	$8.33\text{x}10^{-5}$	0.014
11%	10.39	$2.75\text{x}10^{-5}$	0.007
10%	8.64	$3.80\text{x}10^{-5}$	0.098
9%	7.02	$4.13\text{x}10^{-6}$	0.049
8%	5.56	$1.92\text{x}10^{-5}$	0.056
7%	4.32	$4.67\text{x}10^{-7}$	0.002
6%	3.18	$3.67\text{x}10^{-7}$	0.004
3%	0.81	$3.33\text{x}10^{-8}$	0.003

Similarly, in figure 55.e, we plot crack size as a function of time based on the data collected from all 10 experiments using low crosslink density PGSA. As is the case for the stiff PGSA samples, we also observe both low and high crack growth rate regions. When the applied strain ranges from 21.5% to 18.5%, the crack grows rapidly, and full propagation is observed within 2000 seconds or less. However, when the strain values ranged from 18% to 16%, slow to minimal crack growth was observed with negligible propagation within 3 hours of the applied strain.

In the high crack growth rate region (figure 55.e), the crack velocity ranged from 5.91×10^{-5} ms^{-1} to 2.03×10^{-5} ms^{-1} for 20% and 19% strain respectively (table 5). In contrast, in the low crack growth rate region, the velocity ranged from 1.25×10^{-6} ms^{-1} to 1×10^{-7} ms^{-1} for 18% and 17% applied strains respectively (table 5).

Table 5: Applied stain values, energy release rate and crack velocity of low crosslink density PGSA exposed to 15 seconds of UV radiation along with the standard deviation values.

Low Crosslink Density PGSA – 15 Seconds UV Exposure			
Applied Strain [%]	**Energy Release Rate [G, Jm^{-2}]**	**Crack Velocity [V, ms^{-1}]**	**STD [ms^{-1}]**
21.5%	14.47	2.93×10^{-5}	0.035
21%	13.82	4.33×10^{-5}	0.028
20.5%	13.25	3.88×10^{-5}	0.014
20%	12.64	5.91×10^{-5}	0.084
19%	11.47	2.03×10^{-5}	0.063
18.5%	10.88	5.10×10^{-5}	0.084
18%	10.28	1.25×10^{-6}	0.024
17%	9.23	1.00×10^{-7}	0.031
16.5%	8.74	4.00×10^{-7}	0.00042
16%	8.23	1.67×10^{-7}	0.034

Collectively, our results confirm that crack growth rate increases as a function of the applied strain for both types of PGSA samples. We also confirm that the application of strain values that are close to the fracture strain accelerate crack growth and allow full propagation through the sample. Conversely, we strongly believe that when low strain values are applied on the sample, polymer hydrolysis on the surface of the crack becomes the prevailing factor that drives crack growth and is therefore significantly slower when compared to strain driven crack growth with no observed propagation.

3.3.2.4. Crack growth rate vs. energy release rate

With the results that we have collected and discussed in the previous section, we can find a direct correlation between the crack growth rate, the applied strain, and their significant influence on the hydrolytic degradation of PGSA. By applying 10 different strains on both types of PGSA, we apply a range of energy release rate (*G* in Jm^{-2}) values that are all less than the measured fracture toughness.

For example, in the case of high crosslink density PGSA with $\Gamma = 19.56\ Jm^{-2}$, we apply a maximum *G* of 16.55 Jm^{-2} which was determined using Equation 34 and by calculating the area under the stress-strain curve of the un-notched sample using $\varepsilon_{critical}$ that is equal to 14% strain. Similarly, and by using Equation 34, the energy release rate values applied on the high crosslink density PGSA ranged from 0.81 to 16.55 Jm^{-2} (table 4). In the case of low crosslink density PGSA, the values of *G* ranged from 8.23 to 14.47 Jm^{-2} (table 5).

To visualize how the crack growth rate is correlated with the applied energy release rate *(G)*, we plot the logarithmic values of crack growth velocity (*V*) in ms^{-1} as a function of calculated energy release rate for both low and high crosslink density PGSA (figure 56.a). When both types of PGSA are exposed to high *G* values, the crack grows rapidly and prevails over the effect of hydrolytic degradation. However, when the applied *G* values are low, the two types of PGSA begin to exhibit different behavior. We see that at low strains, the crack grows significantly faster in stiff PGSA (blue circles in figure 56.a) when compared to soft PGSA (green squares in figure 56.a).

We next aim to develop quantitative understandings of the relationship between the crack growth rate and the applied energy release rate. Following **[80]**, we have:

$$log\,V = \ log\,V_0 - G\left(\frac{A^*}{K_B T}\right), \qquad \textbf{(35)}$$

where V is the crack velocity, V_0 is the crack velocity when the energy release is zero, A^* is the activation area, K_B is Boltzmann's constant ($1.38\text{x}10^{-23}$ JK^{-1}) and T is the absolute temperature (300 K). In the case of high crosslink density PGSA and using linear fitting (dashed line in figure 56.a), we find that the slope is equal to 0.181 m^2J^{-1} while the y-intercept is equal to -6.692. By using Equation 35 along with the values obtained from liner fitting, we find that $V_0 = 2.03\text{x}10^{-7}$ ms^{-1} while $A^* = 7.50\text{x}10^{-22}$ m^2 for high crosslink density PGSA.

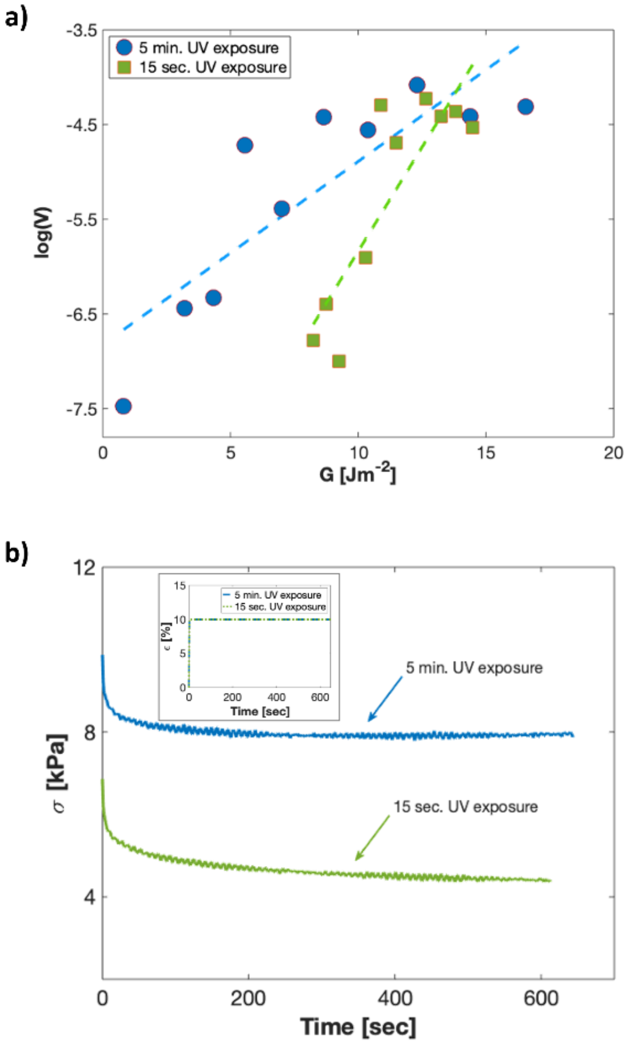

Figure 56: The logarithmic values of crack growth velocity in ms^{-1} (V) were plotted as a function of the energy release rate in Jm^{-2} (G) for both the low and high crosslink density PGSA samples **(a)**. Through linear fitting illustrated by the dashed lines, we observed that the velocity changes with crosslink density. Therefore, we conducted a stress relaxation test under the same experimental conditions where the 10 N load cell was used to apply a 10% strain at 5% s^{-1} and the stress was plotted as function of time **(b)**. Our results confirm that under the same constant strain, the low crosslink density sample experiences more significant stress relaxation when compared to the high crosslink density sample. Note that strain vs. time is added as an inset for the reader's reference.

Now, we can calculate the dissociation energy E_a as follows:

$$V_0 = av * exp\left(\frac{E_a}{K_B T}\right). \tag{36}$$

where v is the average atomic frequency that is equal to 10^{14} Hz and a is the distance of the advancement of the crack tip with the breakage of an ester bond, which can be estimated by the mesh size that is approximately equal to 1 nm for PGSA based on the value of its elastic modulus from figure 54.b. Based on these values, we find that under the influence of hydrolytic degradation, the dissociation energy E_a of the ester bonds in PGSA is equal to 29.14 kJmol^{-1} which is comparable to the values of ester bond dissociation energies reported in literature that range from 27.19 kJmol^{-1} to 30.12 kJmol^{-1} **[99,100]**.

By applying the same type of linear fitting on the low crosslink density PGSA, we find that the value of V_0 is equal to 8.7x10^{-11} ms^{-1} which is 4 orders of magnitude slower. This difference of the crack growth velocities can be explained by investigating the stress relaxation behavior of both types of PGSA where the same experimental setup discussed in section 3.3.2.2 was used to apply a constant 10% strain on both samples at a rate of 5% s^{-1}. Within the first 10 minutes of the experiment (figure 56.b), we see that the stress relaxation in the PGSA with lower crosslink density is more significant (i.e., larger percentage of stress relaxation). Therefore, during the SCC experiment, with a fixed strain, the true energy release rate applied to the elastomer actually decreases with time during crack growth, and the reduction of the energy release rate is greater for the PGSA with lower crosslink density. We believe the slow crack growth observed in PGSA with lower crosslink density is mainly because of its more significant stress relaxation.

3.4. Chapter Conclusions

With the rising concerns regarding global plastic pollution, degradable polymers offer a sustainable solution. However, during the degradation, breakdown of the polymer chains causes them to lose their mechanical strength and structural integrity which needs to be carefully studied for their practical applications. In the current work, we have investigated the hydrolytic erosion of PGSA, a photocurable and biocompatible elastomer, under various experimental conditions.

By observing the *in-situ* degradation of PGSA in an aqueous environment, we confirm that the elastomer undergoes surface erosion. Moreover, the application of varying stress and strain values dramatically alters the degradation rate of the polymer.

Our detailed investigations of the stress corrosion cracking phenomena in PGSA have allowed us to understand the coupled effects of mechanical loading and hydrolytic degradation of PGSA with a pre-crack through correlating crack growth velocity to the energy release rate applied onto PGSA samples. Our experimental results have demonstrated that hydrolytic cracking often outruns the surface erosion of PGSA, and stress relaxation in the sample can decrease the crack growth speed during hydrolytic cracking.

Chapter 3, in full, is coauthored and has been submitted for publication of the material as it may appear in Macromolecular Chemistry & Physics, 2023. Qari, Nada and Cai, Shengqiang. The dissertation author was the primary investigator of this paper.

Summary & Conclusions

In the first chapter, we provide a review on the time-sensitive properties of degradable polymer by exploring a range of mechanical properties including elasticity, toughness, strength, viscosity, and stress corrosion cracking through experimental efforts and computational models that have been developed to study commonly used degradable polymers over the years. Towards the end of the chapter, we focused our attention on polymer erosion and degradation by presenting a wide range of currently used mathematical models and recent experimental results that have been able to highlight important finding regarding these two phenomena.

Based on our thorough review of the literature, we believe that although many efforts have been dedicated to studying the effects of degradation and erosion, much more research is needed before we can gain a deeper understanding on how the mechanical properties change as a function of material degradation. And because of that, the investigations presented in this dissertation have been focused on coupling the effect of mechanical loading with degradation. With the results presented in the remaining chapters we hope to have provided the scientific community with a benchmark on how the mechanical properties of polymers change as a function of degradation and in the presences of external factors such as stress, strain, and extreme pH.

Also, most of the studies discussed in chapter 1 were focused on PLA, PCL, and various ratios of PLLA. Because of that, we focused our research efforts on hydrogels and the photocurable degradable elastomer PGSA.

We believe that our research findings have not only accelerated our understating of these polymers but will also help expand their application envelope along with providing the scientific community with a wider range of practical sustainable materials.

In the second chapter, we investigate the possibilities of tuning the viscoelastic behavior of Hydrogels. This is important because although hydrogels have been used in many applications within the biomedical field, active devices, and soft robots, many of their potential applications can be unlocked by learning how to tune their properties to meet specific requirements for unique applications. With this aspiration in mind, we experimentally studied the viscoelastic behavior of 4 different types of hydrogels: covalently crosslinked polyacrylamide (PAAm), covalently crosslinked PAAm network immersed in a viscous alginate solution, ionically crosslinked alginate along with crosslinked PAAm-alginate double network.

We conducted a systematic investigation on how to tailor the viscoelastic behavior of covalently crosslinked PAAm networks by increasing the viscosity of the aqueous solution in which the polymer network is immersed in. Our results have shown that when AAm monomers are dissolved in water, the PAAm hydrogel behaves elastically under compressive strain and experiences minimal stress relaxation. However, when the same amount of AAm monomers were dissolved in viscous alginate solution, the resulting hydrogels experienced increased viscoelastic behavior with increased alginate concentration. Through theoretical fitting of the rheological model, we reported the relaxation time and how it changes as a function of alginate concentration and applied compressive strain. Moreover, based on the stress relaxation test of ionically crosslinked alginate gel and the double network gel, we have revealed the quantitative correlation between the ionic bond dissociation and force-dependent viscoelastic behavior of gels containing ionic crosslinks.

Although previous studies have assumed that the time scale associated with viscoelasticity is constant, our detailed study of the stress relaxation behavior of ionically crosslinked alginate networks and double network hydrogels have proven otherwise. Through our experimental data and Gent model fitting, we were able to quantitatively correlate the macroscopically viscoelastic behavior of the hydrogel by confirming faster relaxation time at higher compressive strains with the microscopic ionic debonding process while using reasonable activation length Δ_a and dissociation energy E_a.

More importantly, and by reporting the moduli of the different hydrogels investigated in this study, we provide quantitative evidence of a widely accepted theoretical concept within the community and confirm the existence of coordinated covalent bonds that form whenever amine groups on the PAAm chains interact with the carboxyl groups on the alginate chains.

With these reported discoveries, we hope to provide the scientific community with a methodology to develop hydrogels with tunable viscoelastic properties while highlighting the importance of force-dependent stress relaxation and how it is correlated with chain debonding mechanisms within the hydrogel network.

In the third and final chapter, we conducted a systematic investigation on stress-assisted erosion of the photocurable and degradable elastomer poly (glycerol sebacate) acrylate (PGSA). Through our results, and with the rising concerns regarding global plastic pollution, we highlight the potential of PGSA as a promising sustainable polymer.

Although degradable polymers have been widely investigated, during the degradation process, breakdown of the polymer chains causes them to lose their mechanical strength and structural integrity which needs to be carefully studied for their practical applications.

Because of that, we focused on understating the hydrolytic erosion of PGSA under various experimental conditions. By observing the *in-situ* degradation of PGSA in an aqueous environment, we confirm that the elastomer undergoes surface erosion. Moreover, the application of varying stress and strain values dramatically alters the degradation rate of the polymer.

Our detailed investigations of the stress corrosion cracking phenomena in PGSA have allowed us to understand the coupled effects of mechanical loading and hydrolytic degradation with a pre-crack through correlating crack growth velocity to the energy release rate applied onto samples. Our experimental results have demonstrated that hydrolytic cracking often outruns the surface erosion of PGSA, and stress relaxation in the sample can decrease the crack growth speed during hydrolytic cracking. We have further shown that with decreasing the crosslink density of the elastomer, the crack growth speed during SCC can be slowed down due to the increased viscoelasticity of the material.

References

[1] Feldman D. Polymer history. Designed monomers and polymers. 2008 Jan 1;11(1):1-5.

[2] Siracusa V, Rocculi P, Romani S, Dalla Rosa M. Biodegradable polymers for food packaging: a review. Trends in food science & technology. 2008 Dec 1;19(12):634-43.

[3] Plastics: Material-Specific Data, United States Environmental Protection Agency, 2017.

[4] Vroman I, Tighzert L. Biodegradable polymers. Materials. 2009 Apr 1;2(2):307-44.

[5] Nair LS, Laurencin CT. Biodegradable polymers as biomaterials. Progress in polymer science. 2007 Aug 1;32(8-9):762-98.

[6] Vert M. Aliphatic polyesters: great degradable polymers that cannot do everything. Biomacromolecules. 2005 Mar 14;6(2):538-46.

[7] Ispir M, Ates AO, Ilki A. Low strength concrete: Stress-strain curve, modulus of elasticity and tensile strength. In Structures 2022 Apr 1 (Vol. 38, pp. 1615-1632). Elsevier.

[8] Wang Y, Han X, Pan J, Sinka C. An entropy spring model for the Young's modulus change of biodegradable polymers during biodegradation. Journal of the mechanical behavior of biomedical materials. 2010 Jan 1;3(1):14-21.

[9] Ding L, Davidchack RL, Pan J. A molecular dynamics study of Young's modulus changes of semi-crystalline polymers during degradation by chain scissions. Journal of the mechanical behavior of biomedical materials. 2012 Jan 1;5(1):224-30.

[10] "Mechanical Properties of a Material." Smlease Design*,* July 2021.

[11] Safranski DL, Crabtree JC, Huq YR, Gall K. Thermo-mechanical properties of semi-degradable poly (β-amino ester)-co-methyl methacrylate networks under simulated physiological conditions. Polymer. 2011 Sep 29;52(21):4920-7.

[12] Smith KE, Temenoff JS, Gall K. Journal of Applied Polymer Science, vol. 114, no. 27, 2009, 11-22.

[13] Smith KE, Trusty P, Wan B, Gall K. Long-term toughness of photopolymerizable (meth) acrylate networks in aqueous environments. Acta biomaterialia. 2011 Feb 1;7(2):558-67.

[14] Lim H, Hoag SW. Plasticizer effects on physical–mechanical properties of solvent cast Soluplus® films. Aaps Pharmscitech. 2013 Sep; 14:903-10.

[15] "Yield Strength vs. Tensile Strength - What's the Difference?" Matmatch, 2021.

[16] Flory PJ. Tensile strength in relation to molecular weight of high polymers. Journal of the American Chemical Society. 1945 Nov;67(11):2048-50.

[17] Sookne AM, Harris M. Journal of Research of National Bureau of Standards. vol. 30, no. 1, 1943.

[18] "Stress, Strain, and Elastic Modulus." Openstax, University Physics Volume 1, 2021.

[19] Guo M, Chu Z, Yao J, Feng W, Wang Y, Wang L, Fan Y. The effects of tensile stress on degradation of biodegradable PLGA membranes: A quantitative study. Polymer Degradation and Stability. 2016 Feb 1; 124:95-100.

[20] Deng M, Zhou J, Chen G, Burkley D, Xu Y, Jamiolkowski D, Barbolt T. Effect of load and temperature on in vitro degradation of poly (glycolide-co-L-lactide) multifilament braids. Biomaterials. 2005 Jul 1;26(20):4327-36.

[21] Kang Y, Yao Y, Yin G, Huang Z, Liao X, Xu X, Zhao G. A study on the in vitro degradation properties of poly (l-lactic acid)/β-tricalcuim phosphate (PLLA/β-TCP) scaffold under dynamic loading. Medical engineering & physics. 2009 Jun 1;31(5):589-94.

[22] Hollinger JO, Battistone GC. Biodegradable bone repair materials: synthetic polymers and ceramics.

[23] Kikuchi M, Koyama Y, Takakuda K, Miyairi H, Shirahama N, Tanaka J. In vitro change in mechanical strength of β-tricalcium phosphate/copolymerized poly-l-lactide composites and their application for guided bone regeneration. Journal of Biomedical Materials Research: An Official Journal of The Society for Biomaterials, The Japanese Society for Biomaterials, and The Australian Society for Biomaterials and the Korean Society for Biomaterials. 2002 Nov;62(2):265-72.

[24] Cleries L, Fernandez-Pradas JM, Morenza JL. Behavior in simulated body fluid of calcium phosphate coatings obtained by laser ablation. Biomaterials. 2000 Sep 1;21(18):1861-5.

[25] Kashani Rahimi S, Otaigbe JU. Polyamide 6 nanocomposites incorporating cellulose nanocrystals prepared by In situ ring-opening polymerization: Viscoelasticity, creep behavior, and melt rheological properties. Polymer Engineering & Science. 2016 Sep;56(9):1045-60.

[26] Muliana AH, Rajagopal KR. Changes in the response of viscoelastic solids to changes in their internal structure. Acta mechanica. 2011 Mar; 217:297-316.

[27] Atkin RJ, Craine R. Continuum theories of mixtures: basic theory and historical development. The Quarterly Journal of Mechanics and Applied Mathematics. 1976 May 1;29(2):209-44.

[28] Ferry JD. Viscoelastic properties of polymers. John Wiley & Sons; 1980 Sep 16.

[29] Breche Q, Chagnon G, Machado G, Nottelet B, Garric X, Girard E, Favier D. A non-linear viscoelastic model to describe the mechanical behavior's evolution of biodegradable polymers during hydrolytic degradation. Polymer degradation and stability. 2016 Sep 1; 131:145-56.

[30] Khan KA, El-Sayed T. A phenomenological constitutive model for the nonlinear viscoelastic responses of biodegradable polymers. Acta Mechanica. 2013 Feb;224(2):287-305.

[31] Göpferich A. Mechanisms of polymer degradation and erosion. The biomaterials: silver jubilee compendium. 1996 Jan 1:117-28.

[32] Lyu S, Sparer R, Untereker D. Analytical solutions to mathematical models of the surface and bulk erosion of solid polymers. Journal of Polymer Science Part B: Polymer Physics. 2005 Feb 15;43(4):383-97.

[33] Göpferich A. Polymer bulk erosion. Macromolecules. 1997 May 5;30(9):2598-604.

[34] Tamada JA, Langer R. Erosion kinetics of hydrolytically degradable polymers. Proceedings of the National Academy of Sciences. 1993 Jan 15;90(2):552-6.

[35] Brannigan RP, Dove AP. Synthesis, properties and biomedical applications of hydrolytically degradable materials based on aliphatic polyesters and polycarbonates. Biomaterials science. 2017;5(1):9-21.

[36] Ali SA, Zhong SP, Doherty PJ, Williams DF. Mechanisms of polymer degradation in implantable devices: I. Poly (caprolactone). Biomaterials. 1993 Jul 1;14(9):648-56.

[37] Mainil-Varlet P, Curtis R, Gogolewski S. Effect of in vivo and in vitro degradation on molecular and mechanical properties of various low-molecular-weight polylactides. Journal of Biomedical Materials Research: An Official Journal of The Society for Biomaterials and The Japanese Society for Biomaterials. 1997 Sep 5;36(3):360-80.

[38] Akbari H, D'emanuele A, Attwood D. Effect of geometry on the erosion characteristics of polyanhydride matrices. International journal of pharmaceutics. 1998 Jan 12;160(1):83-9.

[39] Shieh L, Tamada J, Tabata Y, Domb A, Langer R. Drug release from a new family of biodegradable polyanhydrides. Journal of controlled release. 1994 Feb 1; 29(1-2):73-82.

[40] Han X, Pan J. A model for simultaneous crystallisation and biodegradation of biodegradable polymers. Biomaterials. 2009 Jan 1;30(3):423-30.

[41] Laycock B, Nikolić M, Colwell JM, Gauthier E, Halley P, Bottle S, George G. Lifetime prediction of biodegradable polymers. Progress in Polymer Science. 2017 Aug 1; 71:144-89.

[42] Vieira AC, Vieira JC, Ferra JM, Magalhães FD, Guedes RM, Marques AT. Mechanical study of PLA–PCL fibers during in vitro degradation. Journal of the mechanical behavior of biomedical materials. 2011 Apr 1;4(3):451-60.

[43] Göpferich A, Teßmar J. Polyanhydride degradation and erosion. Advanced drug delivery reviews. 2002 Oct 16;54(7):911-31.

[44] Von Burkersroda F, Schedl L, Göpferich A. Why degradable polymers undergo surface erosion or bulk erosion. Biomaterials. 2002 Nov 1;23(21):4221-31.

[45] “Stress Corrosion Cracking.” Industrial Metallurgists, 2021.

[46] Pereira HB, Panossian Z, Baptista IP, Azevedo CR. Investigation of stress corrosion cracking of austenitic, duplex and super duplex stainless steels under drop evaporation test using synthetic seawater. Materials Research. 2019 Jan 31;22.

[47] Shi M, Steck J, Yang X, Zhang G, Yin J, Suo Z. Cracks outrun erosion in degradable polymers. Extreme Mechanics Letters. 2020 Oct 1; 40:100978.

[48] Li X, Chu C, Chu PK. Effects of external stress on biodegradable orthopedic materials: a review. Bioactive materials. 2016 Sep 1;1(1):77-84.

[49] Davis DA, Hamilton A, Yang J, Cremar LD, Van Gough D, Potisek SL, Ong MT, Braun PV, Martínez TJ, White SR, Moore JS. Force-induced activation of covalent bonds in mechanoresponsive polymeric materials. Nature. 2009 May 7;459(7243):68-72.

[50] Beyer MK, Clausen-Schaumann H. Mechanochemistry: the mechanical activation of covalent bonds. Chemical Reviews. 2005 Aug 10;105(8):2921-48.

[51] Fan YB, Li P, Zeng L, Huang XJ. Effects of mechanical load on the degradation of poly (d, l-lactic acid) foam. Polymer degradation and stability. 2008 Mar 1;93(3):677-83.

[52] Nakayama A, Kakugo A, Gong JP, Osada Y, Takai M, Erata T, Kawano S. High mechanical strength double-network hydrogel with bacterial cellulose. Advanced functional materials. 2004 Nov;14(11):1124-8.

[53] Tang Z, Huang J, Guo B, Zhang L, Liu F. Bioinspired engineering of sacrificial metal–ligand bonds into elastomers with supramechanical performance and adaptive recovery. Macromolecules. 2016 Mar 8;49(5):1781-9.

[54] Sun JY, Zhao X, Illeperuma WR, Chaudhuri O, Oh KH, Mooney DJ, Vlassak JJ, Suo Z. Highly stretchable and tough hydrogels. Nature. 2012 Sep 6;489(7414):133-6.

[55] Bai R, Chen B, Yang J, Suo Z. Tearing a hydrogel of complex rheology. Journal of the Mechanics and Physics of Solids. 2019 Apr 1;125:749-61.

[56] Agulhon P, Markova V, Robitzer M, Quignard F, Mineva T. Structure of alginate gels: interaction of diuronate units with divalent cations from density functional calculations. Biomacromolecules. 2012 Jun 11;13(6):1899-907.

[57] Bai R, Yang J, Suo Z. Fatigue of hydrogels. European Journal of Mechanics-A/Solids. 2019 Mar 1;74:337-70.

[58] Dordrecht, Viscoelastic Behavior of Polymers. In: Physicochemical Behavior and Supramolecular Organization of Polymers. Springer (2009).

[59] Drozdov AD, Kalamkarov AL. A constitutive model for nonlinear viscoelastic behavior of polymers. Polymer Engineering & Science. 1996 Jul;36(14):1907-19.

[60] Green MS, Tobolsky AV. A new approach to the theory of relaxing polymeric media. The Journal of chemical physics. 1946 Feb 1;14(2):80-92.

[61] Nam S, Hu KH, Butte MJ, Chaudhuri O. Strain-enhanced stress relaxation impacts nonlinear elasticity in collagen gels. Proceedings of the National Academy of Sciences. 2016 May 17;113(20):5492-7.

[62] Chaudhuri O, Gu L, Klumpers D, Darnell M, Bencherif SA, Weaver JC, Huebsch N, Lee HP, Lippens E, Duda GN, Mooney DJ. Hydrogels with tunable stress relaxation regulate stem cell fate and activity. Nature materials. 2016 Mar;15(3):326-34.

[63] Guimarães CF, Gasperini L, Marques AP, Reis RL. The stiffness of living tissues and its implications for tissue engineering. Nature Reviews Materials. 2020 May;5(5):351-70.

[64] Storm C, Pastore JJ, MacKintosh FC, Lubensky TC, Janmey PA. Nonlinear elasticity in biological gels. Nature. 2005 May 12;435(7039):191-4.

[65] Chaudhuri O. Viscoelastic hydrogels for 3D cell culture. Biomaterials science. 2017;5(8):1480-90.

[66] Agarwal P, Lee HP, Smeriglio P, Grandi F, Goodman S, Chaudhuri O, Bhutani N. A dysfunctional TRPV4–GSK3β pathway prevents osteoarthritic chondrocytes from sensing changes in extracellular matrix viscoelasticity. Nature biomedical engineering. 2021 Dec;5(12):1472-84.

[67] Long R, Mayumi K, Creton C, Narita T, Hui CY. Time dependent behavior of a dual cross-link self-healing gel: Theory and experiments. Macromolecules. 2014 Oct 28;47(20):7243-50.

[68] Shen T, Song Z, Cai S, Vernerey FJ. Nonsteady fracture of transient networks: The case of vitrimer. Proceedings of the National Academy of Sciences. 2021 Jul 20;118(29):e2105974118.

[69] Meng F, Pritchard RH, Terentjev EM. Stress relaxation, dynamics, and plasticity of transient polymer networks. Macromolecules. 2016 Apr 12;49(7):2843-52.

[70] Mayumi K, Marcellan A, Ducouret G, Creton C, Narita T. Stress–strain relationship of highly stretchable dual cross-link gels: Separability of strain and time effect. ACS Macro Letters. 2013 Dec 17;2(12):1065-8.

[71] Wang J, Cui K, Zhu B, Gong JP, Hui CY, Zehnder AT. Load transfer between permanent and dynamic networks due to stress gradients in nonlinear viscoelastic hydrogels. Extreme Mechanics Letters. 2023 Jan 1;58:101928.

[72] Fiorillo AA, Galbraith JM. A valence bond description of coordinate covalent bonding. The Journal of Physical Chemistry A. 2004 Jun 10;108(23):5126-30.

[73] Hashemnejad SM, Kundu S. Rheological properties and failure of alginate hydrogels with ionic and covalent crosslinks. Soft Matter. 2019;15(39):7852-62.

[74] Fang Y, Al-Assaf S, Phillips GO, Nishinari K, Funami T, Williams PA, Li L. Multiple steps and critical behaviors of the binding of calcium to alginate. The Journal of Physical Chemistry B. 2007 Mar 15;111(10):2456-62.

[75] Cioroianu AR, Spiesz EM, Storm C. Disorder, pre-stress, and non-affinity in polymer 8-chain models. Journal of the Mechanics and Physics of Solids. 2016 Apr 1;89:110-25.

[76] Campbell KT, Wysoczynski K, Hadley DJ, Silva EA. Computational-based design of hydrogels with predictable mesh properties. ACS biomaterials science & engineering. 2019 Dec 10;6(1):308-19.

[77] Siracusa V, Rocculi P, Romani S, Dalla Rosa M. Biodegradable polymers for food packaging: a review. Trends in food science & technology. 2008 Dec 1;19(12):634-43.

[78] Plastics: Material-Specific Data, United States Environmental Protection Agency, 2017.

[79] Vroman I, Tighzert L. Biodegradable polymers. Materials. 2009 Apr 1;2(2):307-44.

[80] Jiao Q, Shi M, Yin T, Suo Z, Vlassak JJ. Composites retard hydrolytic crack growth. Extreme Mechanics Letters. 2021 Oct 1;48:101433.

[81] Shi M, Steck J, Yang X, Zhang G, Yin J, Suo Z. Cracks outrun erosion in degradable polymers. Extreme Mechanics Letters. 2020 Oct 1;40:100978.

[82] Gross RA, Kalra B. Biodegradable polymers for the environment. Science. 2002 Aug 2;297(5582):803-7.

[83] Walker S, Rueben J, Volkenburg TV, Hemleben S, Grimm C, Simonsen J, Mengüç Y. Using an environmentally benign and degradable elastomer in soft robotics. International Journal of Intelligent Robotics and Applications. 2017 Jun;1:124-42.

[84] Muller J, González-Martínez C, Chiralt A. Combination of poly (lactic) acid and starch for biodegradable food packaging. Materials. 2017 Aug 15;10(8):952.

[85] Weinig, Hans-Georg. Science to Enable Sustainable Plastics. 2020; 82-83.

[86] Lakshmi N, Laurencin C. Progress in polymer science. 2007; 32.8-9: 762-798.

[87] Göpferich A. Mechanisms of polymer degradation and erosion. The biomaterials: silver jubilee compendium. 1996 Jan 1:117-28.

[88] Suping L, Sparer R, Untereker D. Journal of Polymer Science Part B: Polymer Physics. 2005; 43.4: 383-397.

[89] Göpferich A. Polymer bulk erosion. Macromolecules. 1997 May 5;30(9):2598-604.

[90] Tamada JA, Langer R. Erosion kinetics of hydrolytically degradable polymers. Proceedings of the National Academy of Sciences. 1993 Jan 15;90(2):552-6.

[91] Speidel MO, Hyatt MV. Stress-corrosion cracking of high-strength aluminum alloys. In Advances in corrosion science and technology 1972 (pp. 115-335). Boston, MA: Springer US.

[92] Sieradzki K, Newman RC. Brittle behavior of ductile metals during stress-corrosion cracking. Philosophical magazine A. 1985 Jan 1;51(1):95-132.

[93] Braden M, Gent A. Journal of Applied Polymer Science. 1960; 3.7: 90-99.

[94] Yang X, Yang J, Chen L, Suo Z. Hydrolytic crack in a rubbery network. Extreme Mechanics Letters. 2019 Sep 1;31:100531.

[95] Shi M, Jiao Q, Yin T, Vlassak JJ, Suo Z. Hydrolysis embrittles poly (lactic acid). MRS Bulletin. 2023 Jan;48(1):45-55.

[96] Wang Y, Ameer GA, Sheppard BJ, Langer R. A tough biodegradable elastomer. Nature biotechnology. 2002 Jun;20(6):602-6.

[97] Gerecht S, Townsend S, Pressler H, Zhu H, Nijst C, Bruggeman J, Nichol J, Langer R. Biomaterials. 2007; 28.32: 4826-4835.

[98] Yadong W, Kim Y, Langer R. Journal of Biomedical Materials Research Part A: An Official Journal of The Society for Biomaterials, The Japanese Society for Biomaterials, and The Australian Society for Biomaterials and the Korean Society for Biomaterials. 2003; 66.1: 192-197.

[99] Zhan C-G, Landry D, Ornstein R. Journal of the American Chemical Society. 2000; 122.11: 2621-2627.

[100] Li H, Li H, Dai Q, Li H, Brédas JL. Hydrolytic Stability of Boronate Ester-Linked Covalent Organic Frameworks. Advanced Theory and Simulations. 2018 Feb;1(2):1700015.